GULF GENERAL ATOMIC

Gulf-GA-A12530

GAS-COOLED FAST BREEDER REACTOR

QUARTERLY PROGRESS REPORT

FOR THE PERIOD NOVEMBER 1, 1972 THROUGH JANUARY 31, 1973

by

Project Staff

Prepared for the
U.S. Atomic Energy Commission
San Francisco Operations Office
Under
Contract AT(04-3)-167
Project Agreement No. 23

Gulf General Atomic Project 393

March 8, 1973

GULF GENERAL ATOMIC COMPANY
P.O. BOX 81608, SAN DIEGO, CALIFORNIA 92138

PROGRESS REPORT SERIES

GA-5537	November 1, 1963 to July 31, 1964
GA-6667	August 1, 1964 to July 31, 1965
GA-7645	August 1, 1965 to July 31, 1966
GA-8107	August 1, 1966 to July 31, 1967
GA-8787	August 1, 1967 to July 31, 1968
GA-8895	August 1, 1968 through October 31, 1968
GA-9229	November 1, 1968 through January 31, 1969
GA-9359	February 1, 1969 through April 30, 1969
GA-9639	May 1, 1969 through July 31, 1969
GA-9811	August 1, 1969 through October 31, 1969
GA-9838	November 1, 1969 through January 31, 1970
GA-10517	February 1, 1970 through January 31, 1971
GA-10645	February 1, 1971 through April 30, 1971
GA-A10803	May 1, 1971 through July 31, 1971
GA-A10906	August 1, 1971 through October 31, 1971
GA-A12003	November 1, 1971 through January 31, 1972
GA-A12165	February 1, 1972 through April 30, 1972
GA-A12252	May 1, 1972 through July 31, 1972
GA-A12421	August 1, 1972 through October 31, 1972

ABSTRACT

The tasks of the Gas-Cooled Fast Breeder Reactor (GCFR) program that are supported by the U.S. Atomic Energy Commission are program planning, core development, development of a pressure equalization system for fuel rods, fuels and materials development, and nuclear analysis and reactor physics. Core development work included analytical studies of the effects of fuel-rod spacer grid misalignment, the design and start of construction of a fuel-rod–spacer wear and fretting test, the thermal-hydraulic performance of the GCFR fuel element, and a fuel-rod calculation model. A development program plan for the pressure equalization system was prepared. The status of the thermal- and fast-flux irradiation programs is given. The results to date of the fission-gas release data from the vented fuel rod GB-10 being irradiated in the ORR are given. Reactor physics work was concerned with critical assembly analysis of small-sample worths, comparing the results of GGA and ANL calculations of a 300-MW(e) GCFR core, and defining physics design problems of the GCFR.

CONTENTS

Figures

Tables

1. INTRODUCTION

The Gas-Cooled Fast Breeder Reactor (GCFR) program sponsored by the U.S. Atomic Energy Commission consists of five tasks: Task 1000—Program Planning, Task 4100—Core Development, Task 4160—Pressure Equalization System for Fuel, Task 4200/4400—Fuels and Materials Development, and Task 4700—Nuclear Analysis and Reactor Physics. The broad objectives of each of these tasks and a summary of the work done on each task during the period covered by this report are given in this section. The work performed under each task during the period is presented in Sections 2 through 6.

The GCFR Utility Program, which is supported by a large number of electric utility companies, rural electric cooperatives, and Gulf General Atomic, is primarily directed toward the development of a 300-MW(e) GCFR demonstration plant. This utility-sponsored work and the AEC-sponsored work are complementary.

1.1. TASK 1000—PROGRAM PLANNING

Work on this task is directed toward implementing the technical development of the GCFR concept. In addition, this task provides for liaison with Argonne National Laboratory (ANL) and Oak Ridge National Laboratory (ORNL) on tasks they are performing under AEC funding; the corresponding work at Gulf General Atomic is being privately funded.

1.2. TASK 4100—CORE DEVELOPMENT

The objective of this task is the engineering development of the reactor core and associated components. The various investigations carried out under this task during this reporting period are given in Section 3.

Analytical studies of the fuel-element assembly are directed toward developing the design criteria for selecting a fuel-rod spacer reference design. Structural analyses made during this reporting period included (1) the effects of element rotation on rod distortion and additional studies of the effect of initial distortion on rod bowing, (2) the distortion of the fuel-element box using an improved correlation for metal swelling and allowing for creep, and (3) the interactions of the spacer-grid dimple and the fuel rod. The thermal-hydraulic performance of the GCFR fuel element, when modified by the fuel-rod distortions predicted, was investigated. This study included the effects of varying the clearances between the fuel rods and the element box wall, the effects of rod displacement and the sensitivity of temperatures to the rod-bundle size. The experimental program to evaluate the mechanical interaction between the spacer-grid dimple and the fuel-rod cladding surface is also discussed.

Fuel-rod and blanket-rod modeling studies are being made to develop a technique for predicting GCFR rod behavior. The results of the fast and thermal irradiations of GCFR rods are being used to test the calculated predictions of rod diameter expansion.

In the studies of the lower shield assembly, the removal of heat by natural convection from the top surface of debris in the lower shield assembly was investigated.

1.3. TASK 4160—PRESSURE EQUALIZATION SYSTEM FOR FUEL

The objective of this task is to develop a system for equalizing the pressure between the inside and the outside of the GCFR fuel rod.

During this quarterly period, the development planning document for the GCFR pressure equalization system (PES) was prepared and a draft was submitted to the Division of Reactor Development and Technology for review.

1.4. TASK 4200/4400—FUELS AND MATERIALS DEVELOPMENT

The fuels and materials development and testing program extends and applies Liquid-metal Fast Breeder Reactor (LMFBR) fuel technology to GCFR

requirements. This includes surveillance of the LMFBR fuels and materials program to utilize existing and developing technology applicable to the GCFR. The status of the thermal-flux and fast-flux irradiation test programs is presented in Section 5.

No further postirradiation examination of the GB-9 fuel rod was carried out at ANL during this quarterly period. The metallograpic examination of a section of the GB-9 rod subjected to burst-testing is discussed.

The vented-fuel-rod, sweep-gas capsule irradiation experiment GB-10, which is operating at 12 kW/ft, had reached a burnup of ~12,000 MWd/Te at the end of this reporting period. Fission-gas release data analyzed during the period were received from Oak Ridge National Laboratory (ORNL) for several sweep-gas flow modes. These results are discussed and also the analysis of the pressure drop across the GB-10 capsule during initial startup.

The F-1 (X094A) subassembly being irradiated in EBR-II had reached a peak burnup exposure of 52,500 MWd/Te in the lead fuel rod (capsule G-1).

The data package for the five replacement capsules to be inserted in the F-1 (X094A) subassembly during the next interim examination at ~50,000 MWd/Te average exposure and detailed as-built capsule drawings were prepared.

Postirradiation examination of the fuel-rod capsule G-3, which was removed from the F-1 experiment at 27,000 MWd/Te burnup, is continuing.

The diameters of the three irradiated concentric stainless steel tubes that comprise the G-3 capsule of the F-1 experiment were obtained from the maximum of the relative Mn^{54} activity in the steel.

Planning for the F-3 fast-flux irradiation experiment continued. Some changes in the details of the loadings of the capsules were made and also in the dosimetry. Fabrication of the fuel and hardware for the experiment is under way.

1.5. TASK 4700—NUCLEAR ANALYSIS AND REACTOR PHYSICS

This task involves the surveillance of LMFBR physics work and critical

experiments to properly coordinate and develop a complementary GCFR nuclear analysis and physics program. The work performed under this task during this reporting period is discussed in Section 6.

Work on this task was primarily focused on comparisons of GGA and ANL physics calculations of a 300-MW(e) GCFR, which showed excellent agreement between the two calculations. Work is continuing on the definition of physics problems affecting the design of the GCFR.

2. TASK 1000—PROGRAM PLANNING

Work under this task includes liaison with Argonne National Laboratory on safety analysis and with Oak Ridge National Laboratory on steam generator dynamic modeling, which are being performed under AEC funding; the corresponding work at Gulf General Atomic is privately funded.

The dynamic modeling of the GCFR steam generator being done at ORNL involves modifications to the hybrid computer simulation of the MSBR steam generator. A three-phase development program has been agreed on, which involves comparative analyses at various stages. Descriptions of the boundary conditions for two transient test cases, which will be used for comparing the ORNL and GGA steam-generator models, were sent to ORNL.

Other work under this task has included the preparation of a quality assurance program for the GCFR project.

3. TASK 4100—CORE DEVELOPMENT

3.1. FUEL-ELEMENT ASSEMBLY

The development of the information necessary to provide design criteria for fuel- and blanket-rod spacers and element assemblies continued. The factors affecting the design criteria for the element assembly and the interactions between those factors were described in the previous quarterly report.[1] In addition, a structural analysis to evaluate the mechanical, thermal, and neutron swelling forces acting on the fuel-rod spacers and the resulting distortions of the fuel rods was reported. During this quarterly period, the thermal-hydraulic performance of the element assemblies when modified by the fuel-rod distortions predicted from the structural analysis was investigated. Structural analyses were also initiated on the element assembly parts, such as the spacer-grid dimple and the hexagonal box enclosing the assembly. The experimental phase of this program, which is to study the problem of fretting and wear due to interacting forces between the fuel rod and the spacer as a function of helium purity, operating conditions, and spacer–rod geometry and distortion, was continued. The design of the test setup is nearly complete.

3.1.1. Structural Analyses

3.1.1.1. Fuel-rod Distortions.

1. Rotation Effects. Additional analyses involving periodic rotation of an element assembly were conducted using the modified CRASIB code[2] with the subroutine ROTATE. As stability problems occurred with this subroutine after the first rotation at 5,000 hr, it was concluded that ROTATE needs further development. However, qualitatively, the fact that periodic rotation appreciably reduces both rod and element distortions was previously established.[1][3] The rod-bowing analysis[1] showed that even without rotation the total distortion after 10,000 full power hours (FPH) was no greater than 6 mils. Therefore, an element rotation scheme that includes periodic

rotation at intervals of 5,000 FPH should result in a maximum rod distortion of less than 6 mils. Because of this positive conclusion and the need to spend available efforts on other necessary analysis planned for the element assembly, the development of the rotation code has been deferred.

2. Initial Distortion. Further analysis of the effect of initial rod distortion has resulted in additional conclusions to those given in Ref. 3. The initial rod distortion was determined analytically with the CRASIB code by locating several support points such that they are initially displaced some distance from the nominal fuel-rod centerline. This simulates the condition where spacers are misaligned with each other during assembly. Two cases of misalignment are used for the analysis, namely, a 0.007-in. displacement and a 0.012-in. displacement. These were designated cases 3 and 4 in Ref. 1. The spacers displaced were numbers 1, 4, 5, and 8, which are located at axial positions 9.10 in., 36.40 in., 45.50 in., and 72.80 in., respectively, along the total rod length of 81.84 in. The results for case 3 are plotted in Fig. 3.1 and those for case 4 in Fig. 3.2, along with the results of case 1 (the base case) for all spacer grids aligned along the fuel-rod axis. It is noted that the maximum distortion for case 1 (aligned spacers) is located at an axial position of about 59 in. However, when the spacers are misaligned, the maximum distortion shifts to the area of the misaligned spacers, specifically between spacers 4 and 5. At the end of the 20,000 FPH, the net bowing distortion is 9.2 mils and 15.5 mils for cases 3 and 4, respectively, at the location of the initial maximum distortion caused by the misaligned spacers. Thus, the distortion increase for the element lifetime is concluded to be small. It should be noted, however, that the distortion at the axial location of 59 in. has increased from 5 mils for case 1 to 7.6 mils and 9.5 mils for cases 3 and 4, respectively. Since this represents an increase of about 50% and 100% for these two cases, the additional conclusion should be that misalignment of spacers can result in a significant increase in distortion at specific locations but that the position of maximum distortion may shift to the location of the misaligned spacers. Further analysis of these misalignment effects may be necessary to provide a basis for design criteria and tolerance specifications for the GCFR fuel elements.

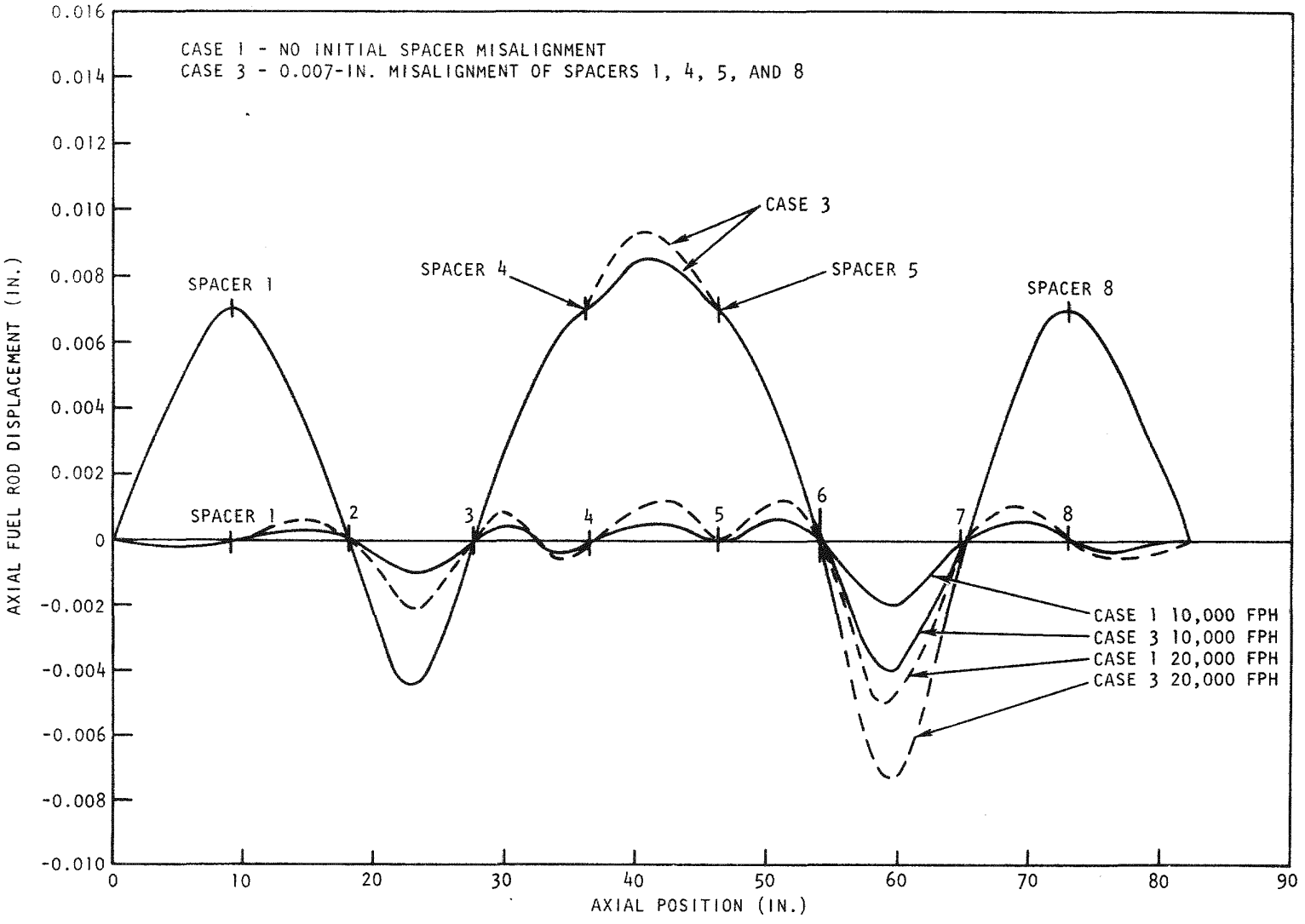

Fig. 3.1 Comparison of fuel-rod bowing with no initial spacer misalignment and with initial misalignment of spacers 0.007 in. from fuel-rod centerline

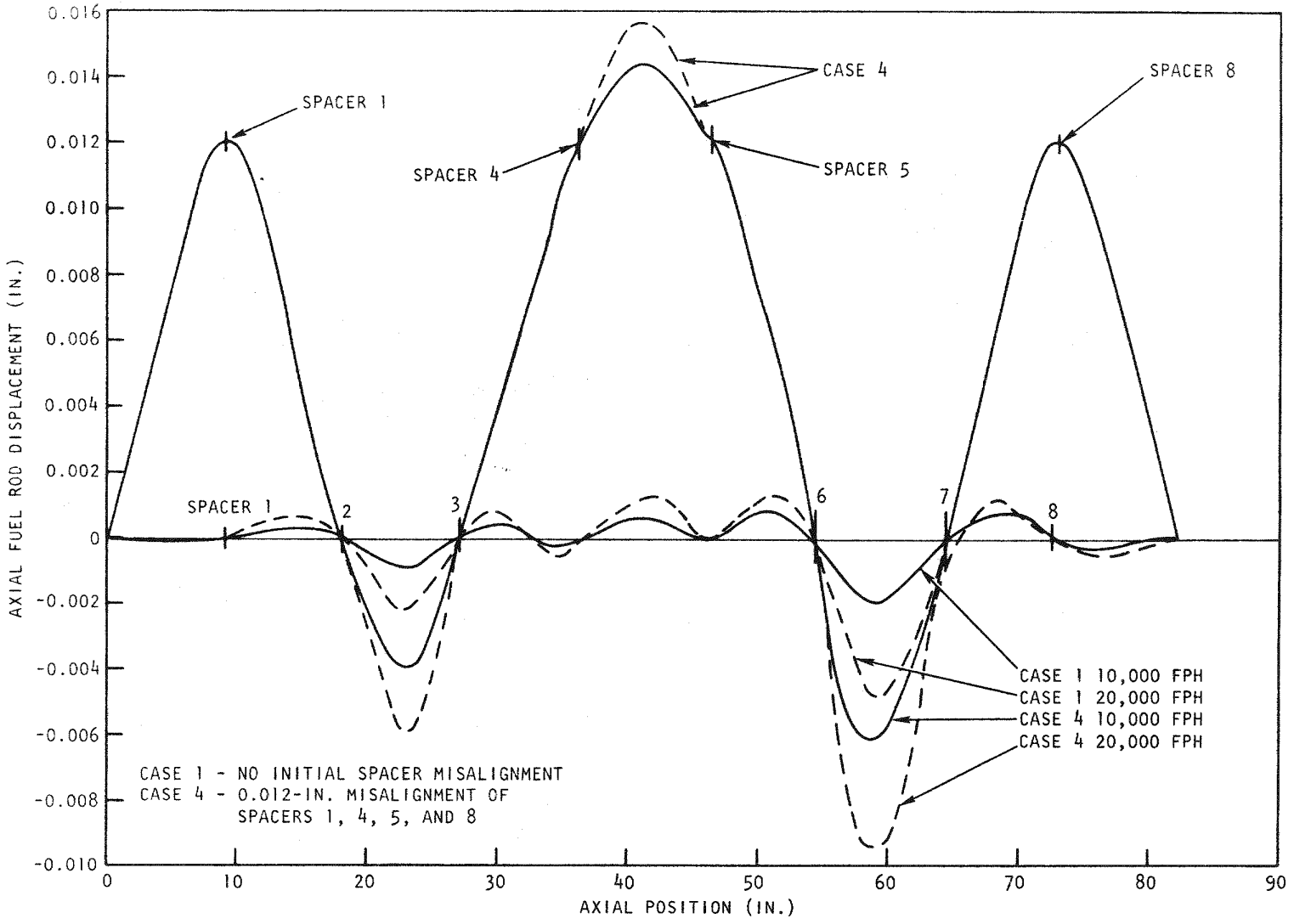

Fig. 3.2 Comparison of fuel-rod bowing with no initial spacer misalignment and with initial misalignment of spacers 0.012 in. from fuel-rod centerline

3.1.1.2. Fuel-element Distortion.

1. Hexagonal Box. The modified CRASIB code was utilized to analyze the distortion of the fuel-element hexagonal box. This analysis used corrected input data that more realistically represents the GCFR fuel-element design. These corrected data are:

1. The bowing direction was taken perpendicular to the flat wall of the element rather than through the corner.

2. Corrected temperature and flux distributions across the element were used. The distributions in Ref. 3 were about 25% higher because the full radial gradient was applied to the mean values for the element rather than the minimum value.

The results are shown in Fig. 3.3. The maximum deflection of the lower end of the box wall was 1.90 in. after 15,000 FPH. The maximum stress is less than 2,000 psi and the maximum total creep strain is 0.75 mil. Rotation of the element every 5,000 FPH will reduce this maximum deflection. Although the stresses and strains in the box wall are not high, they must be combined with the stresses and strains resulting from other loads, such as pressure and seismic loads, before their acceptability can be determined. The distortion predicted by CRASIB is only two-thirds of that calculated in Ref. 3 for the same set of conditions using a GGA code that did not include creep. This difference is due to an improved correlation in CRASIB for metal swelling and allowing for creep.

2. Spacer-Box-wall Interaction. Analysis of the interaction of the fuel-rod spacer with the element box wall is being initiated. The first step is to analyze the wall distortion due to the mechanical, thermal, and irradiation environment. The analysis will be done with a finite-element model code that calculates the elastic-plastic-creep response of structures to thermal, swelling, and mechanical loads.

3.1.1.3. Rod–Spacer-grid-dimple Interaction. The initial clearance between the spacer-grid dimple and the fuel rod is designed to prevent excessive interaction between the rods and spacer dimples due to differential thermal and swelling expansion during the fuel-element lifetime. However, relative misalignment of the spacer grids at assembly and bowing of the fuel

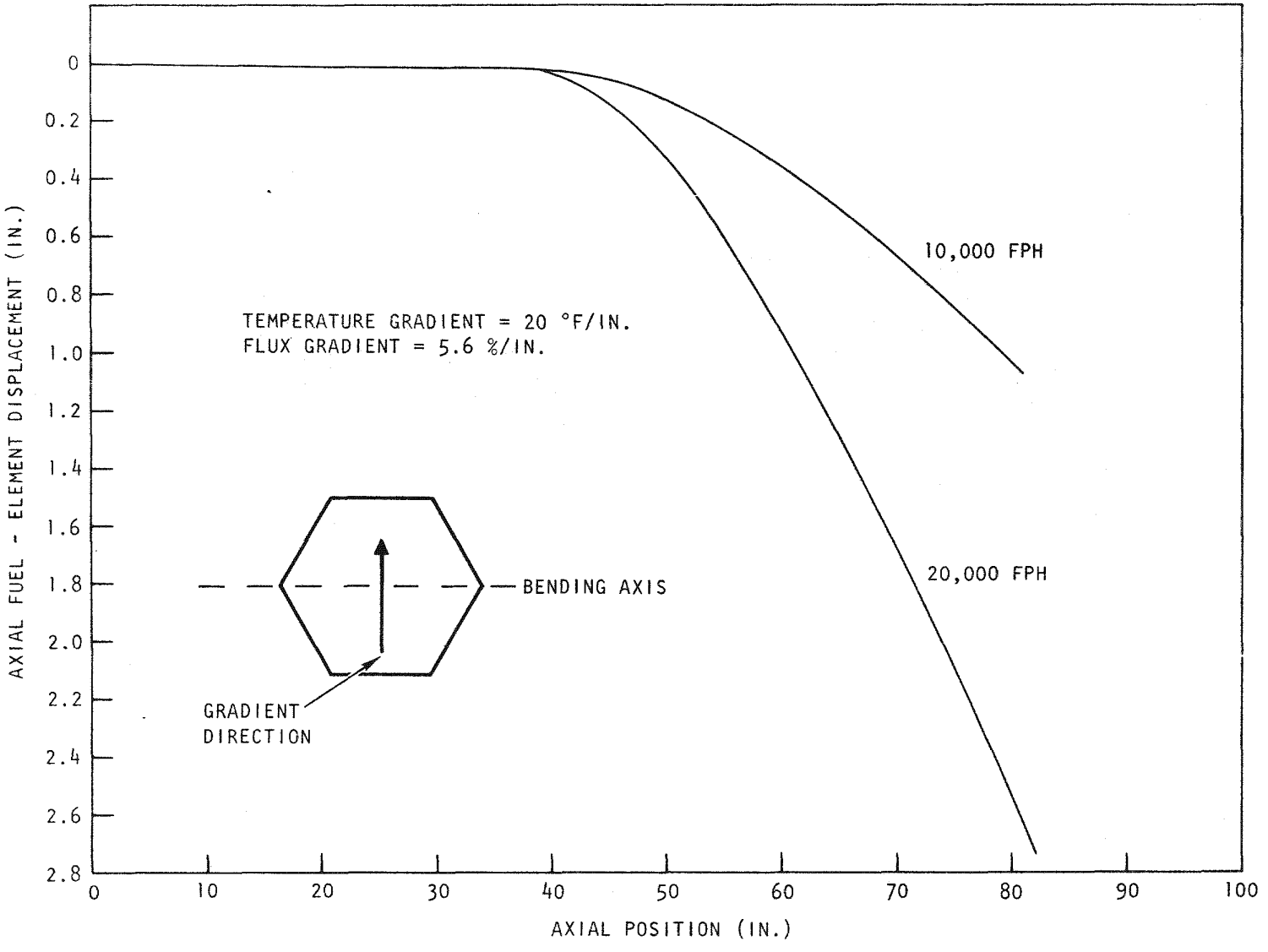

Fig. 3.3 Distortion of fuel element without rotation

rods during operation will cause bending of the rods and interaction forces on the rods due to a stiff clamped support have been calculated with the CRASIB code.[1][4] The fuel-rod forces will produce elastic deflections and plastic distortions of the spacer grid that will reduce the magnitude of the effective reaction force between the spacer grid and the rod. The degree of reduction depends on the relative stiffnesses of the spacer-grid and fuel-rod system.

An elastic load-deflection test of a spacer-grid dimple by GGA was reported in Ref. 4. A similar test on a spacer-grid-dimple design being developed for the LMFBR fuel-element assembly and for a backup to the FFTF fuel-element assembly was reported in Ref. 5. The data for the GGA dimple load deflection test and those for the LMFBR dimple load deflection test are plotted in Fig. 3.4. The thicker 12-mil wall of the referenced LMFBR dimple, compared to the 10-mil-thick GGA dimple, accounts for its higher stiffness, i.e., 17 lb/mil for the LMFBR design compared to 10 lb/mil for the GGA design. It should be noted that the plotted data are for a concentrated loading on the dimple, as shown in Fig. 3.5,[6] and that the dimple is much stiffer than the support-grid wall itself. In fact, the referenced LMFBR grid wall has axial slots (see Fig. 3.6) and is very flexible, with typical stiffness values of 1 lb/mil or less. The above comparison is to verify the mechanical test and analytical data and not to show advantages of one design over another. The 10-mil wall thickness of the GGA spacer was arbitrarily selected for a heat-transfer test and thus is not necessarily an optimized design detail of the GCFR spacer grid.

The effect of the dimple stiffness on the net rod-dimple interaction force due to rod bending, such as occurs with grid misalignment, can be evaluated qualitatively using the simple loading diagrams shown in Fig. 3.7.[5] The rod displacement for no flexibility, i.e., the grid misalignment, is δ_m and the rod-dimple stiffness, the net rod displacement, and rod-dimple interaction force are reduced to δ_g^m and P, respectively. For equilibrium or balance of the forces between the two systems, the following relation[6] between the initial force, F, and the reduced force, P, must be true:

$$P = \left(\frac{Kg}{Kg + 2Kr} \right) F,$$

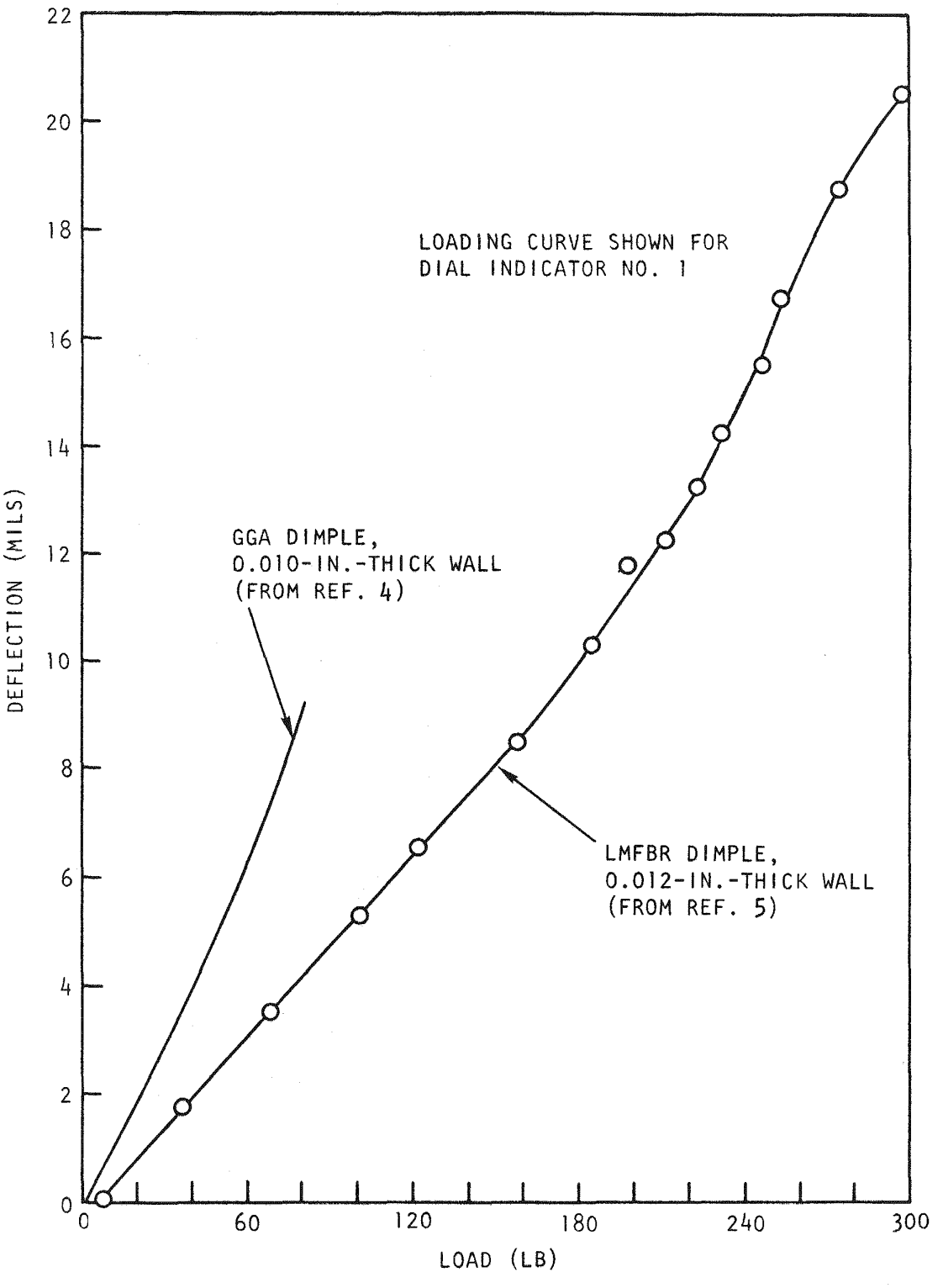

Fig. 3.4 Load vs. deflection for tests of GGA and LMFBR spacer-grid dimple designs

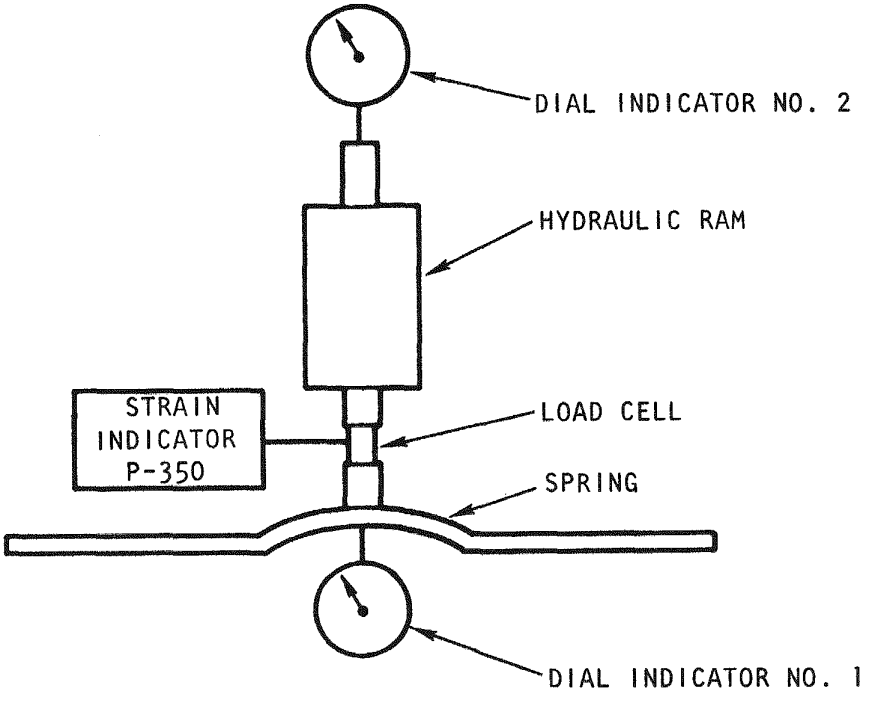

Fig. 3.5 Grid model dimple bending test setup
(taken from Ref. 6)

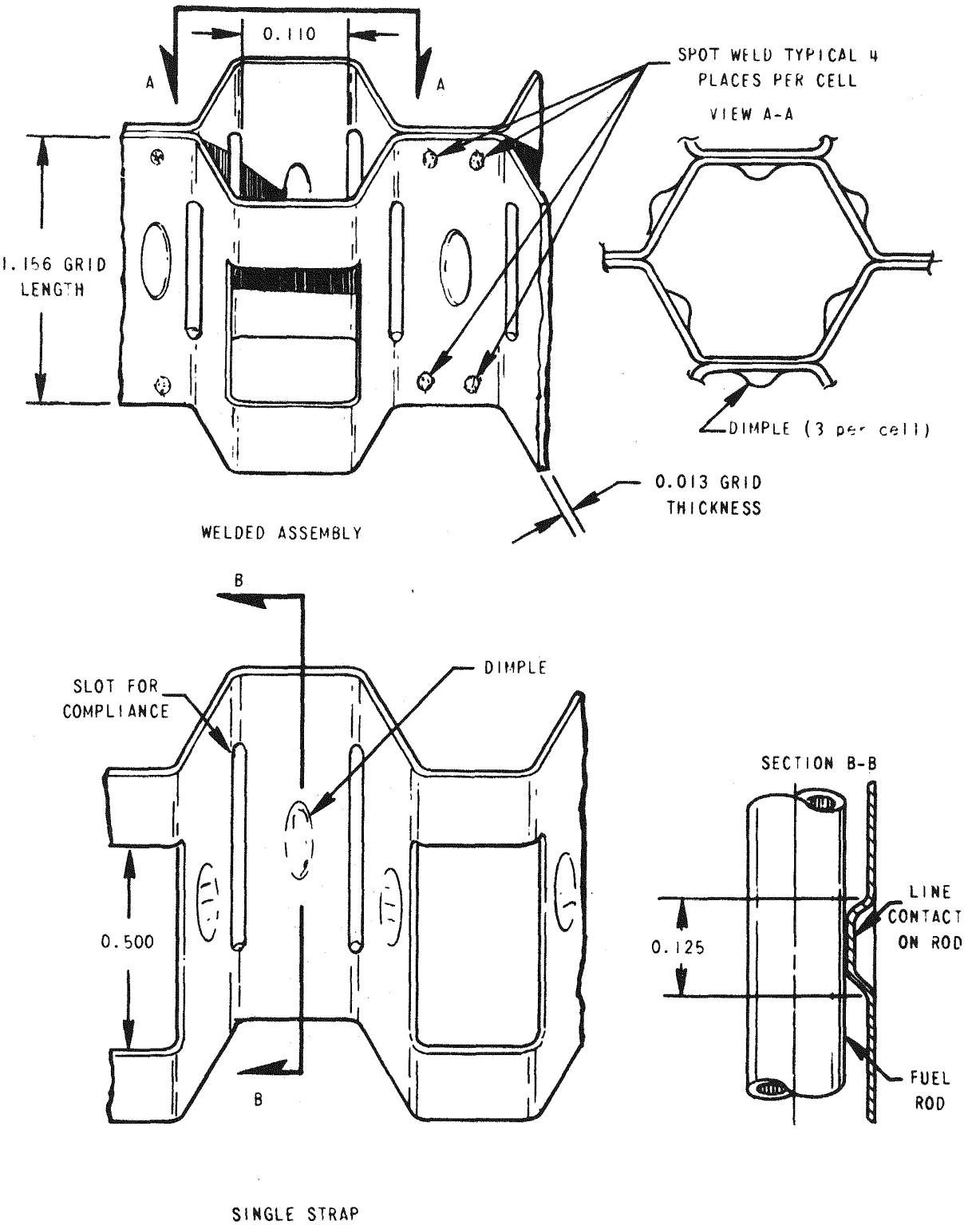

Fig. 3.6 Honeycomb grid-dimple design for LMFBR application (dimensions in inches) (taken from Ref. 7)

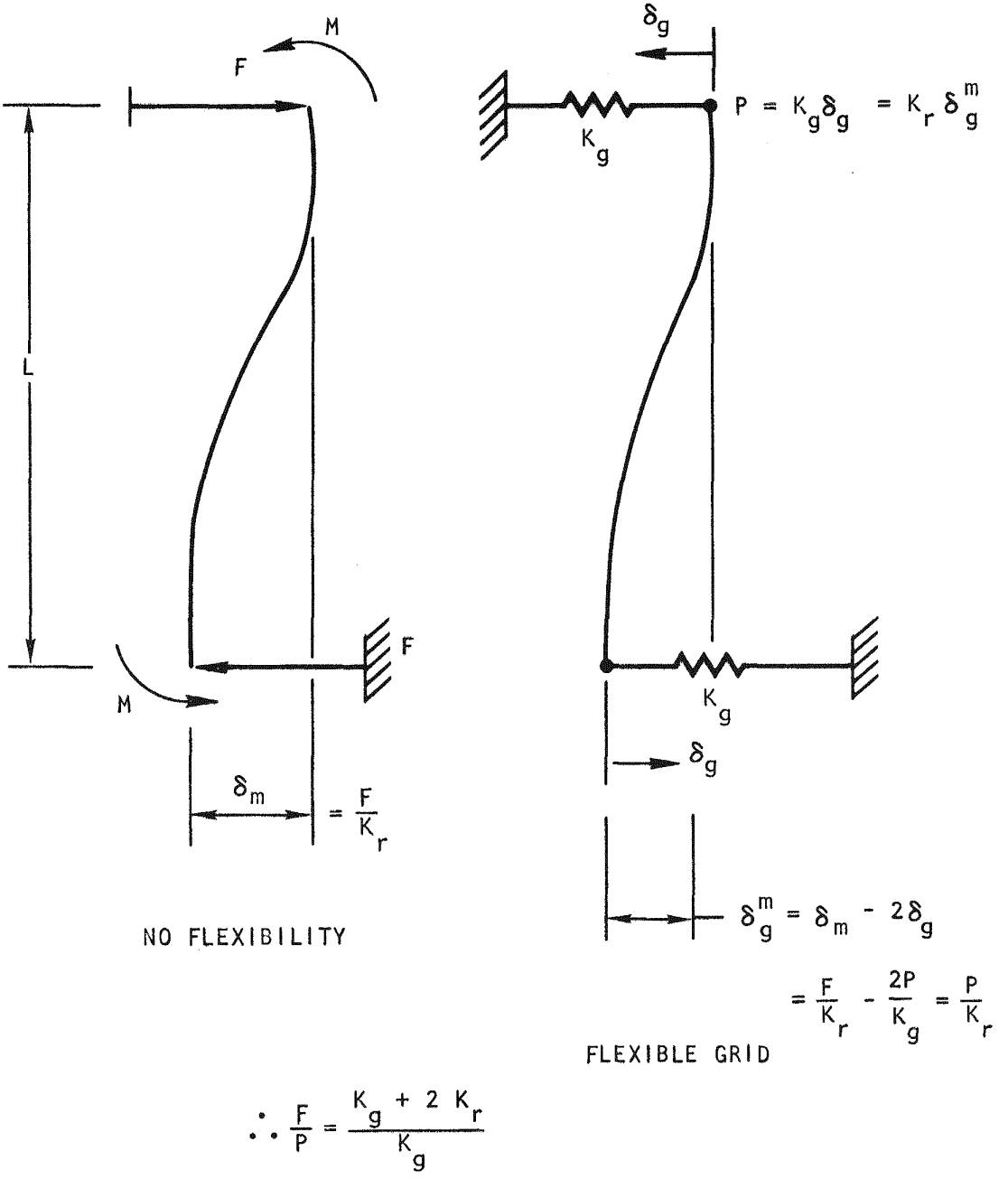

Fig. 3.7 Spacer-grid–fuel-rod misalignment models (taken from Ref. 5)

where K_g = grid-dimple stiffness, lb/in.,

K_r = rod stiffness, lb/in.

For the GGA reference design, the values for elastic stiffness are

K_r = 100 lb/in. (from Fig. 3.3 of Ref. 8 for 9 in. pitch),

K_g = 5,000 to 10,000 lb/in. (estimated from test values in Ref. 4 and reduced for design temperature).

Then, for K_g = 5,000 lb/in.,

$$P = \frac{5{,}000}{5{,}000 + 2(100)} = 0.96\ F$$

and for K_g = 10,000 lb/in.,

$$P = \frac{10{,}000}{10{,}000 + 2(100)} = 0.98\ F.$$

That is, the dimple deflection has only a 4% or less effect on the net elastic rod-dimple interaction force. The effect of the grid wall flexibility is more signficant than dimple compliance in reducing the interaction force. Again, for the elastic analysis, the following values are estimated

K_r = 100 lb/in.,

K_{gw} = stiffness of grid wall $\approx$ 2,000 lb/in., (from case 11 of Table III in Ref. 9),

$$P = \left(\frac{K_{gw}}{K_{gw} + 2K_r}\right) F = \frac{2{,}000}{2000 + 200} = 0.91\ F.$$

Thus, the net elastic interaction force between the rod and spacer-dimple wall can be estimated to be within 10% of the calculated force on the rod due to bending by misaligned spacers. For comparison, an analysis in Ref. 6 resulted in the conclusion that the reduced interaction force is 70% to 90% of the initial rod bending force. It is expected that the LMFBR slotted grid wall would result in a greater reduction of rod force.

An analogous situation to the forces due to grid misalignment is the forces due to thermal- and swelling-induced bowing of the fuel rod being resisted by the grid spacers. The additional effect of creep and plasticity of the spacer has to be analyzed. Although the CRASIB analysis of fuel-rod distortion included creep effects, the predicted forces from the CRASIB

analysis are probably not changed appreciably by creep of the spacer-dimple structure.

3.1.2. Thermal-Hydraulic Analysis

The thermal-hydraulic analysis is coupled with the structural analysis of the GCFR fuel element to provide design performance information on spacer—fuel-rod interaction. Early in the quarter, the thermal-hydraulic code HETHRA was made operational. HETHRA, which is a modification of the COBRA-II program,[10] is capable of performing the detailed thermal-hydraulic analysis of the GCFR fuel element on a subchannel-by-subchannel basis for studying a range of geomtric parameters, such as fuel-rod-to-box-wall clearance, fuel-rod thermal and radiation distortion (change of coolant passage geometry), variation in element size, and spacer effects. Early results indicate that uniform fuel-rod distortion (displacement) causes a rate of cladding temperature increase of 2 ±1°F per mil of displacement. This value applies both to displacement toward another fuel rod and toward the box wall. Based on a temperature increase of 2°F/mil, the spacer tolerances can be related to cladding temperatures. It is tentatively concluded that for practical spacer manufacturing tolerance, the cladding temperature variation will be within acceptable limits. From a study of the effects of sinusoidal rod bowing in which a cladding temperature increase of ~1/2°F/mil displacement was calculated for the maximum displacement studied (10 mils), it is further concluded that the < 10-mil calculated displacement due to bowing will result in only very small cladding temperature increase.

3.1.2.1. Code Development. The HETHRA code is designed specifically to analyze the thermal-hydraulic performance of the helium-cooled GCFR fuel element at or near design conditions with local flow-passage distortion. The flow area within an element is divided into subchannels and the thermal-hydraulic conditions in each subchannel are calculated for an axial increment. Uniform temperatures and flow conditions are assumed to exist within a subchannel and the heat-transfer coefficient is the same for all heater surfaces associated with a particular subchannel. This approach ignores the fine structure of the variation of the heat-transfer coefficient circumferentially around a rod and the circumferential conduction within a rod. Between subchannels, cross flow and turbulent mixing are calculated and the

results are used to modify the flow and temperatures for each subchannel so that the axial pressure drop is approximately the same for all subchannels. Before the modification of COBRA-II was started, possible alternative codes were reviewed. The HECTIC-II code[11] and the Swiss Federal Institute for Reactor Research code SCEPTIC[12] were examined and were found to be superior in certain areas, such as allowing for radiant heat transfer and having an excellent matrix solution method; however, such items as allowing for flow passage variation, flow redistribution, and turbulent mixing were not easily accounted for in HECTIC-II. At some future time, HETHRA and SCEPTIC might be merged, taking the best algorithms from each. Another possible code is CLUHET, which is a detailed thermal-hydraulic code under development by the Swiss Federal Institute for Reactor Research (EIR). CLUHET includes the circumferential variation of the heat-transfer coefficient and circumferential conduction and will thus produce a more accurate determination of the temperature distribution around a fuel rod. Recent information indicates that this code is not yet operational. For the near term, modifying COBRA-II was chosen as the better approach.

The existing COBRA-II provides for 25 fuel rods, 36 subchannels, and 60 subchannel connections; these numbers are set by the computer storage limits and the way the storage is used. A GCFR fuel element contains 271 rods, approximately 600 subchannels, and 870 subchannel connections. Initially, HETHRA was set up with the helium property data replacing the property data for other coolants, which resulted in a considerable saving in data storage and the elimination of unused subroutines. A one-twelfth sector of a GCFR fuel element was run satisfactorily and checked out with HETHRA. The input data were programmed so that identical data for different subchannels did not have to be duplicated. The code was segmented so that the data from each subsequent axial increment are stored in peripheral storage and thus more core storage was available for increasing the code subchannel capacity. To further expand the capacity, some data arrays were compacted by restating the data so that only non-zero data were stored. The current capacity of HETHRA was tested by running a calculation for a 37-rod bundle consisting of 96 subchannels and 132 subchannel interconnections. This problem used 57,400 core storage locations out of the 65,500 available. Further compaction of the data arrays and expansion of the

subchannel capacity are possible by rewriting the flow matrix algorithms.

3.1.2.2. Rod-to-Box-wall Clearance Effects. The effect of varying the clearance between the fuel rods and the element box wall was studied for a 7-rod bundle. Other parameters that were varied were the turbulent eddy mixing factor and the use of smooth and roughened rods. In the case of the roughened rods, the ratio of Stanton number to friction factor, h/f, was taken to be 2/3. The remaining design values were specified to provide a simple system simulating the GCFR in which the effect of varying the clearance could be easily identified. To reduce the number of geometric parameters, the scalloping of the GCFR box wall was not included. These design values are listed in Table 3.1. As the clearance between the rod and box wall varies, so does the flow area and the total quantity of coolant passing through the element. In order to maintain the average outlet temperature at 1007°F, the heat input into the rods was adjusted. The results of the calculations are shown in Fig. 3.8 for smooth rods and in Fig. 3.9 for roughened rods. In these figures the clearance, or rod-to-box-wall distance, is plotted versus a temperature factor (which is defined as the maximum cladding temperature minus the inlet temperature) for the turbulent mixing factor and the locations in the bundle. The temperature factor combines the subchannel coolant temperature rise with the local heat-transfer temperature difference and contains two parts of the hot-spot factor, namely, the coolant distribution and the heat-transfer coefficient. In addition to the 7-rod bundle calculations, an infinite-lattice calculation was performed that yielded a coolant temperature rise of 417°F and a smooth-rod heat-transfer difference of 164°F for a temperature factor of 581°F. For the surface-roughened rod, the heat-transfer difference is 82°F and the temperature factor is 499°F. Since the box wall degrades the element thermal performance, the infinite-lattice cladding temperature will be less than the maximum cladding temperature for a real fuel element.

From these results, it is concluded that for a 7-rod bundle with smooth rods, the optimum fuel-rod-to-wall clearance is 0.066 in. and for a 7-rod bundle with roughened rods (h/f = 2/3), the optimum fuel-rod-to-wall

Table 3.1

PARAMETERS FOR STUDYING BOX-WALL-TO-FUEL-ROD CLEARANCE FOR A SEVEN-ROD BUNDLE

Variable parameters	
Box-wall-to-rod clearance (G), in.	0.043, 0.050, 0.056, 0.064, 0.071
Turbulent eddy mixing factor (y)	3, 4, 5
Stanton number-to-friction factor ratio, h/f	
Smooth rods	1/1
Roughened rods	2/3
Constant parameters	
Rod diameter, in.	0.285
Rod pitch, in.	0.389
Length, in.	60
Spacers	None
Inlet temperature, °F	590
Average outlet temperature, °F	1007
Inlet helium pressure, psia	1250
Average helium mass flow, $lb/(hr)(ft^2)$	300,000
Infinite lattice Reynolds number	100,000
Uniform heating	Varied to obtain 1007° ave. outlet temperature
Velocity at inlet	Constant

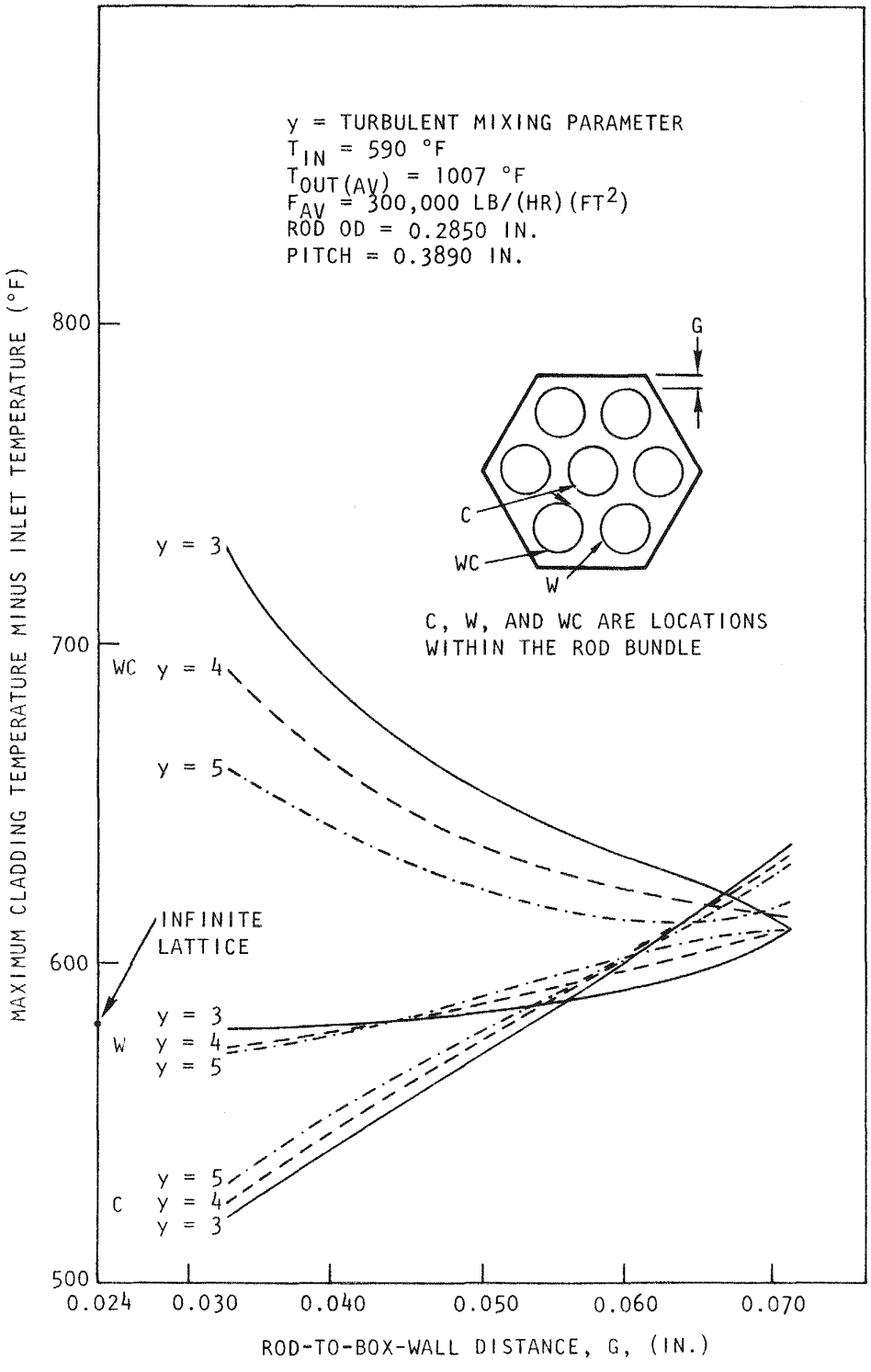

Fig. 3.8 Effect of wall-to-rod clearance in a 7-rod bundle for a smooth rod

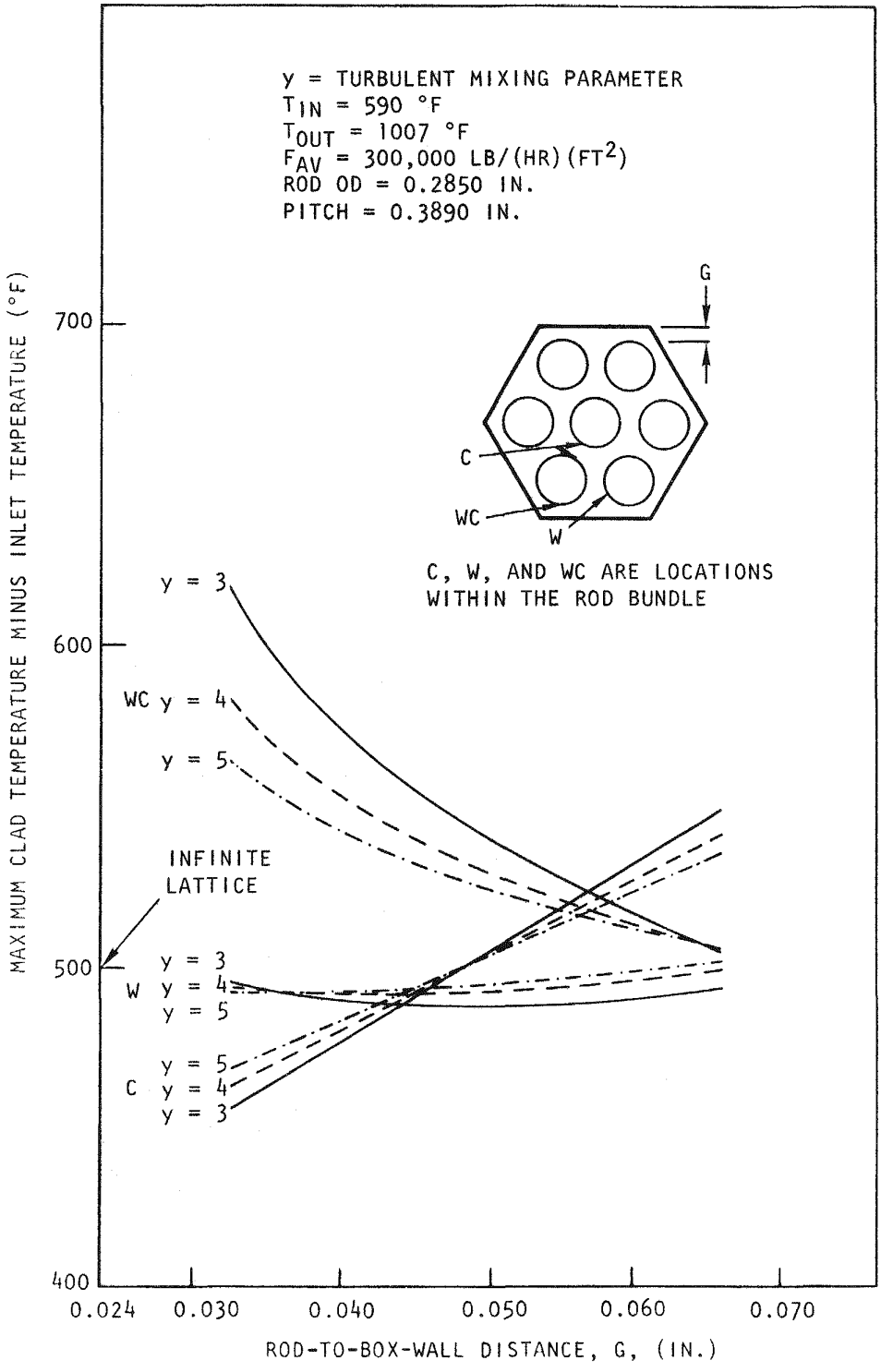

Fig. 3.9 Effect of wall-to-rod clearance in a 7-rod bundle for a roughened rod

clearance is 0.056 in. Near the optimum clearance, the maximum wall temperature is not greatly affected by the magnitude of the turbulent mixing factor. A review of the literature on turbulent mixing in rod bundles indicates a mixing of 3 to 5, using the formulation of Ingesson.[13] For future calculations, an average mixing factor of 4 will be used.

At the optimum rod-to-wall clearance, the curves for maximum wall temperature for the center subchannel and for the corner subchannel intersect, as shown in Figs. 3.8 and 3.9. The sensitivity of the maximum wall temperature to rod-to-wall clearance is indicated by the slope of the curves and is in the range of 2 ±1 °F/mil. The corresponding infinite-lattice maximum wall temperature indicated on each figure is less than the value calculated for a 7-rod bundle with an optimum wall clearance, indicating that a box wall effect for a 7-rod bundle increases the maximum wall temperature minus the inlet temperature by 6% for smooth fuel rods and by 4% for roughened fuel rods. For the portion of the fuel-rod surface indicated by "W" in Figs. 3.8 and 3.9, the surface temperature is below the other surface temperatures at the optimum clearance, which indicates overcooling. In the current GCFR design, the box wall is scalloped in this area to reduce overcooling.

3.1.2.3. Rod Displacement Effects. The effect of displacement of the center rod from the nominal position was analyzed for the roughened 7-rod bundle with the optimum box-wall-to-fuel-rod clearance of 0.056 in. The rod displacement was uniform along the length and in the direction of the diagonal of the hexagonal box. The model for the analysis is shown in Fig. 3.10. The temperature patterns for fuel-rod displacements of 0, 0.005, 0.013, 0.026, and 0.052 in. are shown in Figs. 3.11 through 3.15.

For a 0-in. displacement, the rod surface facing the hexagonal box corner is slightly hotter than its interior surface by 4°F, indicating that a slightly less than optimum clearance has been specified. With a slight rod displacement, the outer rod surface continues to be the hottest surface until the gap between the rods is less than 75% of the original clearance. At one-half the original clearance, the cladding surface of the displaced

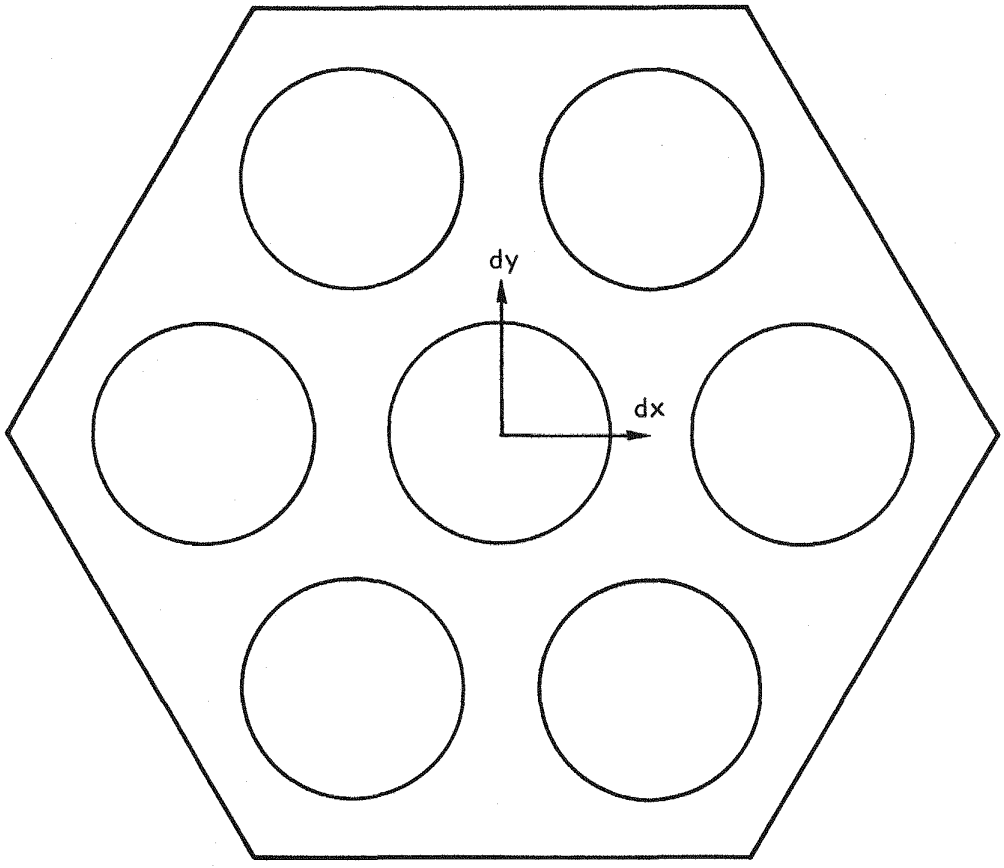

ROD DIAMETER = 0.285 IN.
ROD PITCH = 0.389 IN.
ROD-TO-WALL CLEARANCE = 0.056 IN.
ROD-TO-ROD CLEARANCE = 0.104 IN.

Fig. 3.10 Model for center-rod displacement in a 7-rod bundle for the temperature plots shown in Figs. 3.11 through 3.16

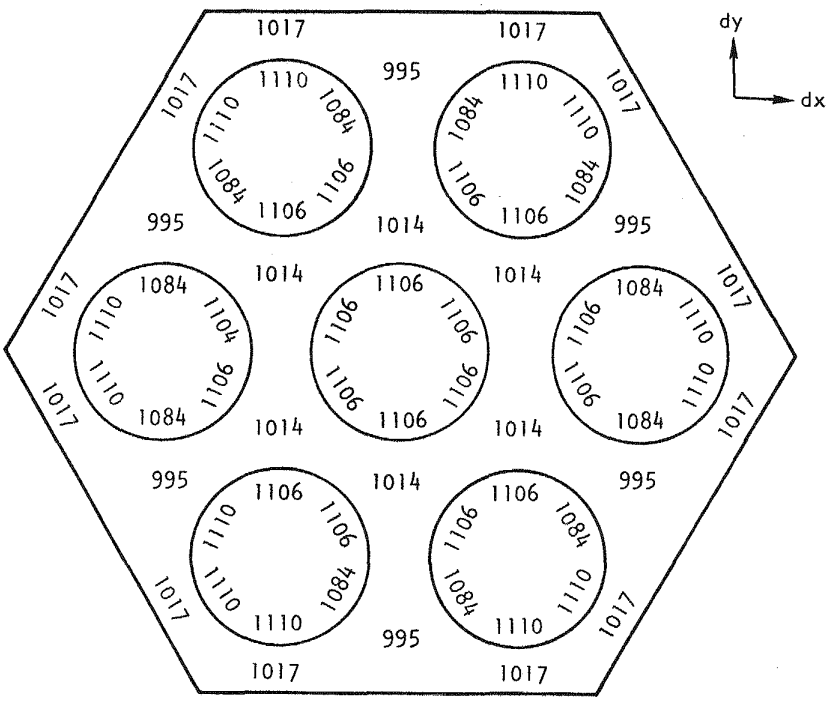

Fig. 3.11 Temperature distributions for center-rod displacement of 0 in. (dy = 0 in.)

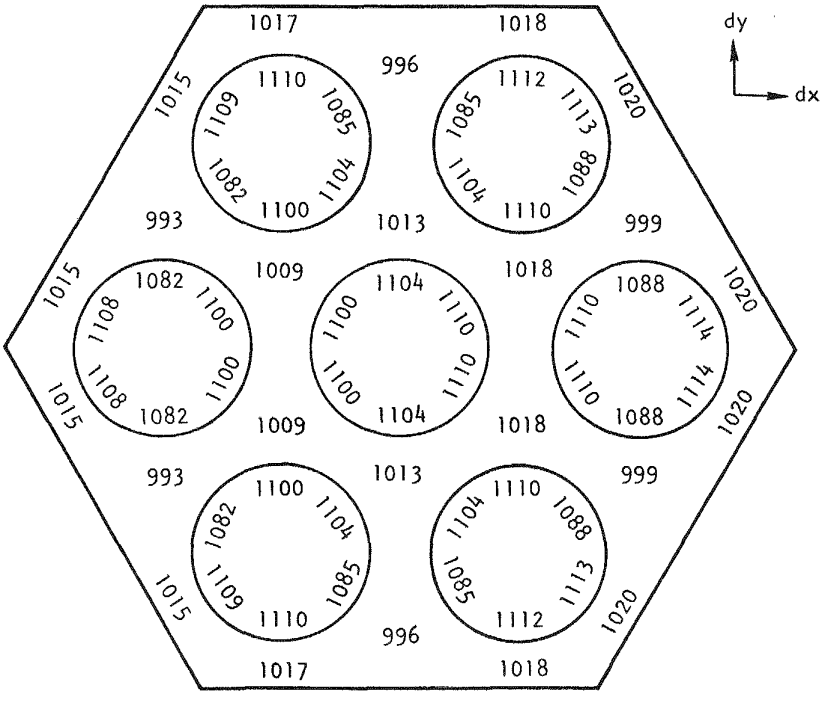

Fig. 3.12 Temperature distributions for center-rod displacement of 0.005 in. (dy = 0 in.)

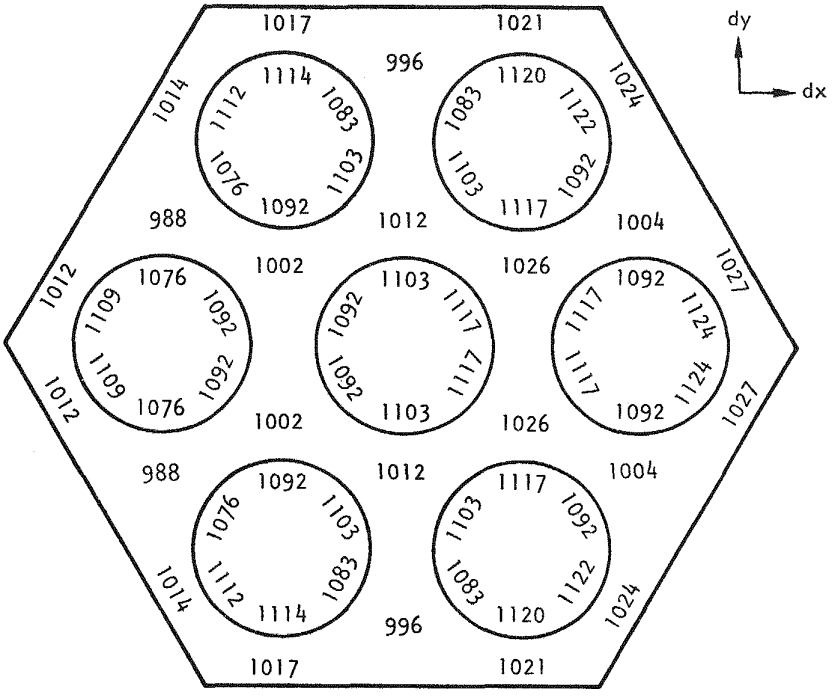

Fig. 3.13 Temperature distributions for center-rod displacement of 0.013 in. (dy = 0 in.)

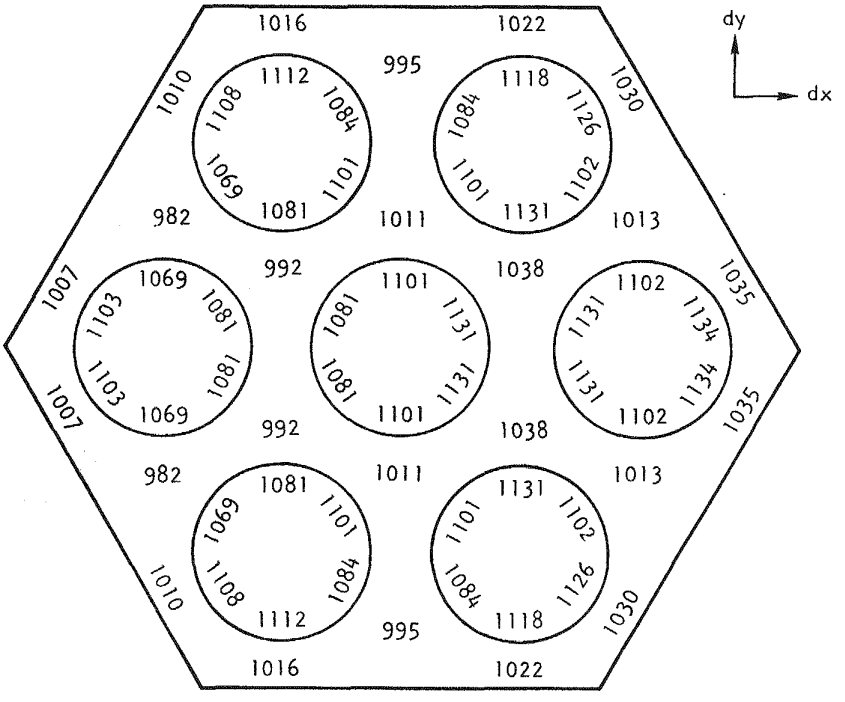

Fig. 3.14 Temperature distributions for center-rod displacement of 0.026 in. (dy = 0 in.)

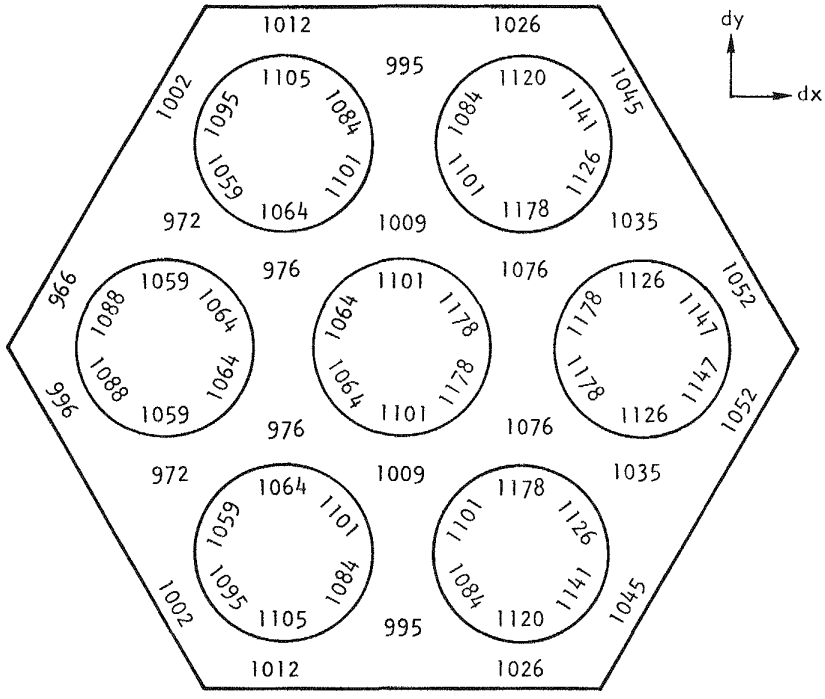

Fig. 3.15 Temperature distributions for center-rod displacement of 0.052 in. (dy = 0 in.)

rod has increased 72°F, whereas the surface facing the hexagonal box corner has increased 37°F.

A comparative case with sinusoidal bowing of the center rod (maximum displacement of 0.010 in. at the center) was calculated; the outlet temperature is shown in Fig. 3.16. The maximum temperature increase for a bowed rod is about one-half the value for a uniformly displaced rod.

Figure 3.17, which is a plot of the data for the fuel-rod displacements shown in Figs. 3.11 through 3.15, shows the effect of the displacement of the center fuel rod on the cladding temperature relative to an infinite lattice of fuel rods for the hottest inner-rod surface and the corner-rod surface. The zero-displacement slope is about 1°F cladding increase per mil displacement for both corner and inner surface. The average slope for the inner rod surface to a 0.050-in. displacement relative to the infinite rod lattice is 2°F/mil.

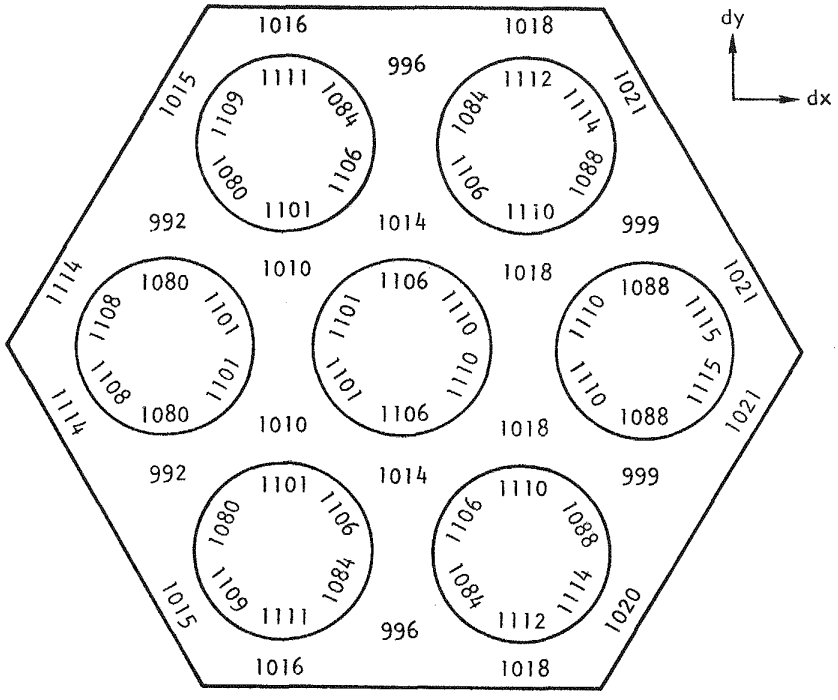

Fig. 3.16 Temperature distributions for sinusoidal bowing of center rod (dx = 0.01 in.; dy = 0 in.)

Since one of the goals of these studies is to relate rod bowing and displacement to hot-spot factors and from them the criteria for the spacer-grid design, the hot-spot channel factor corresponding to each of the calculated displacements was determined; these are listed in Table 3.2. For comparison purposes, the design values currently being used for the reference GCFR fuel element are also listed. It should be emphasized that a value of unity for the hot-spot channel factor corresponds to ideal behavior in an infinite lattice. Therefore, even at zero displacement, the hot-spot channel factor in a 7-rod bundle is greater than unity since the fuel duct wall tends to degrade performance.

The data listed in Table 3.2 are also plotted in Fig. 3.18. Two conclusions are evident from this figure:

1. The hot-spot channel factor is not very sensitive to displacements of the magnitude being calculated with the CRASIB code, namely, less than 0.010-in. displacements.

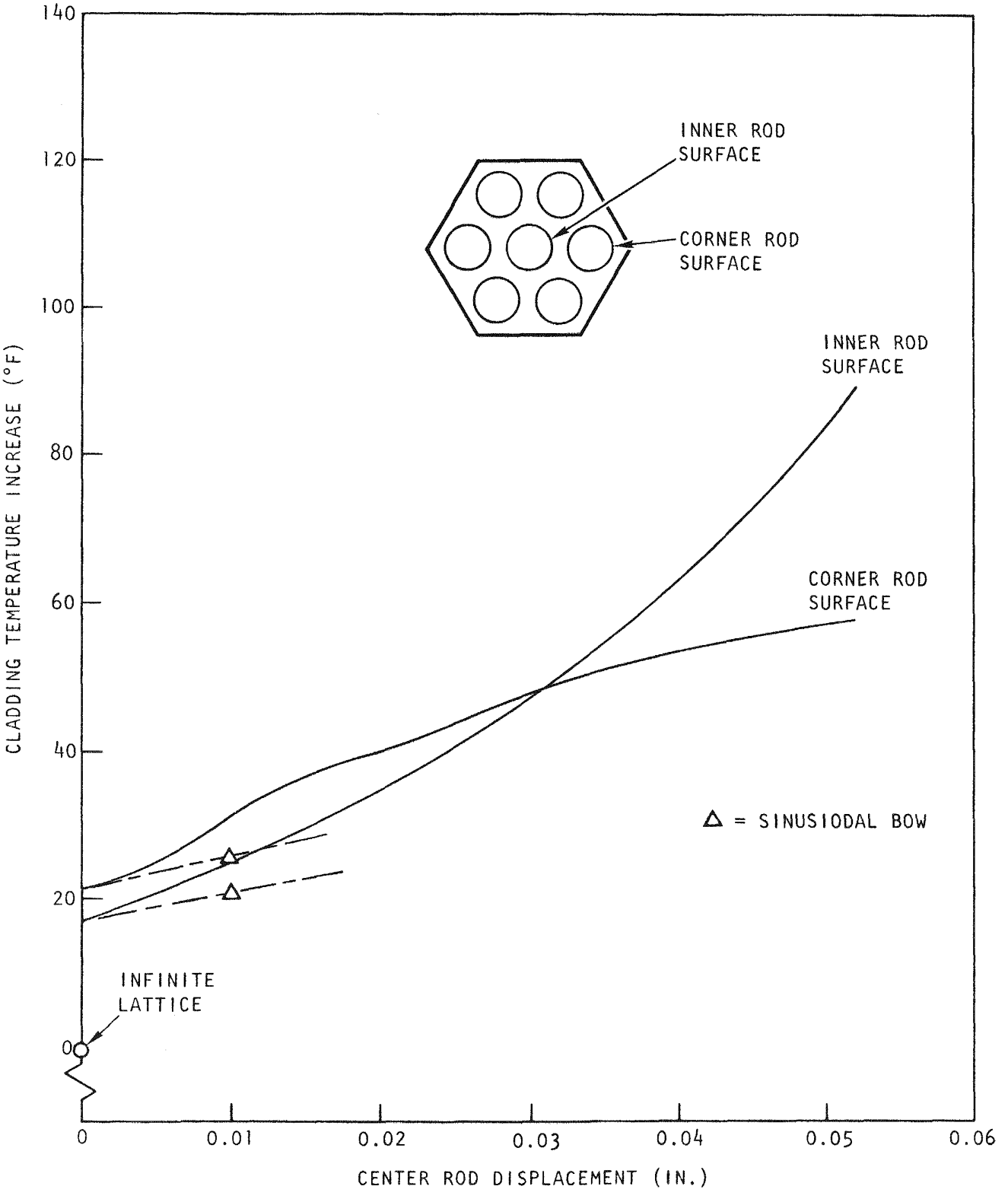

Fig. 3.17 Effect of center-rod displacement on cladding temperature for a 7-rod bundle

Table 3.2

HOT-SPOT CHANNEL FACTORS AS A FUNCTION OF CENTER-ROD DISPLACEMENT FOR A SEVEN-ROD BUNDLE

Surface-roughened rods, h/f = 2/3
Inlet gas temperature = 590°F
Average outlet temperature = 1007°F
Rod diameter = 0.285 in.
Rod pitch = 0.389 in.
Reynolds No. ≈ 100,000

	Displacement (in.)	Minimum Rod Clearance (in.)	Hot-spot Channel Factor
Infinite lattice of rods	0	0.104	1.000
Seven-rod bundle			
Uniform displacements	0	0.104	1.021
	0.005	0.099	1.025
	0.013	0.091	1.031
	0.026	0.078	1.048
	0.052	0.052	1.075
Sinusoidal bowing	0.010	0.094	1.025
Current GCFR design values			
Pitch tolerance (2%, or 0.008 in.)	----	----	1.057
Rod bowing (1%, or 0.004 in.)	----	----	1.028

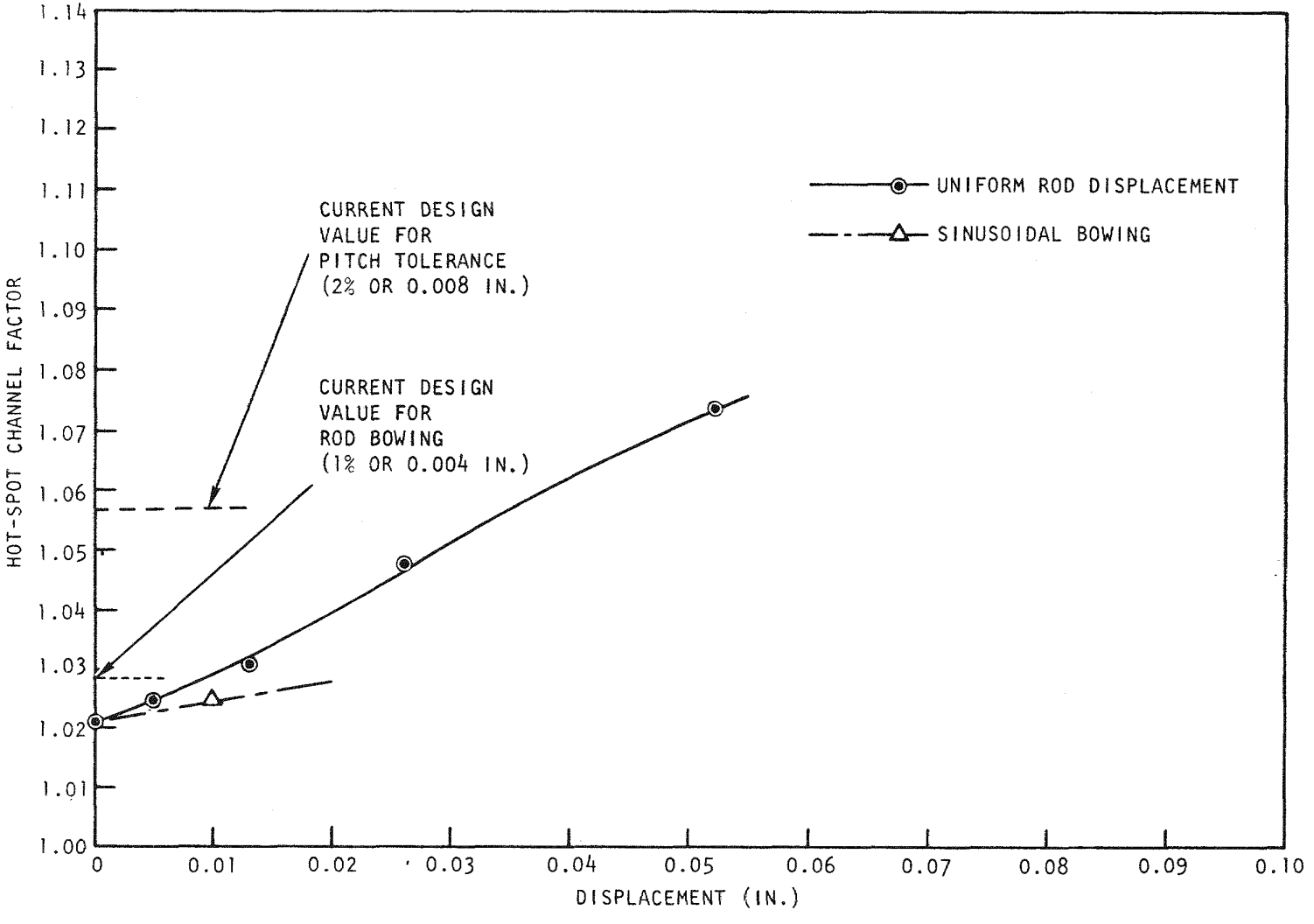

Fig. 3.18 Calculated hot-spot channel factor as a function of displacement for a 7-rod bundle

2. The current design values for the hot-spot channel factors resulting from rod bowing and rod pitch tolerance are larger than the hot-spot channel factors calculated for the 7-rod bundle. This difference will be even greater for a full-size fuel element, which more closely approaches an infinite lattice.

3.1.2.4. Bundle-size Effects. To determine the sensitivity of the temperatures to bundle size, 7-rod, 19-rod, and 37-rod bundles were analyzed for the conditions given in Table 3.1 but with the variable parameters set as follows:

Fuel-rod-to-box-wall clearance	0.050 in.
Turbulent eddy mixing factor	4.0
Roughened rod h/f	2/3

The radial power profile was uniform and no fuel-rod displacement was assumed so the results were symmetrical for each one-sixth sector. Figure 3.19 shows the results for a one-sixth sector of the 7-, 19-, and 37-rod bundles. The choice of a fuel-rod-to-box-wall clearance of 0.050 in. is about optimum for the 19-rod bundle with a center-rod cladding temperature of 1113°F and a corner-rod maximum cladding temperature of 1114°F. The 7-rod bundle is undercooled at the outer corner, yielding a maximum cladding temperature of 1118°F. In Fig. 3.11, with an optimum clearance of 0.056 in., the maximum cladding temperature is about 1110°F. The 37-rod bundle is undercooled at the center with a 0.050-in. clearance, which causes a maximum cladding temperature of 1116°F. A slightly smaller clearance would yield a small decrease in cladding temperatures. It is concluded that the sensitivity of temperature to bundle sizes of 7, 19, and 37 rods is small, provided a near-optimum clearance between the fuel rod and the box wall is maintained and no rod displacement is considered.

3.1.2.5. Axial Heat Distribution and Rod Spacer Effects. The above analysis examined a simplified set of operating conditions in which the effect of varying a particular parameter was easily identified and the temperature sensitivity to the particular parameter was evident. For the 7-rod bundle, an analysis was performed using the GCFR geometry and operating conditions. The temperatures that were calculated as a function of axial position are

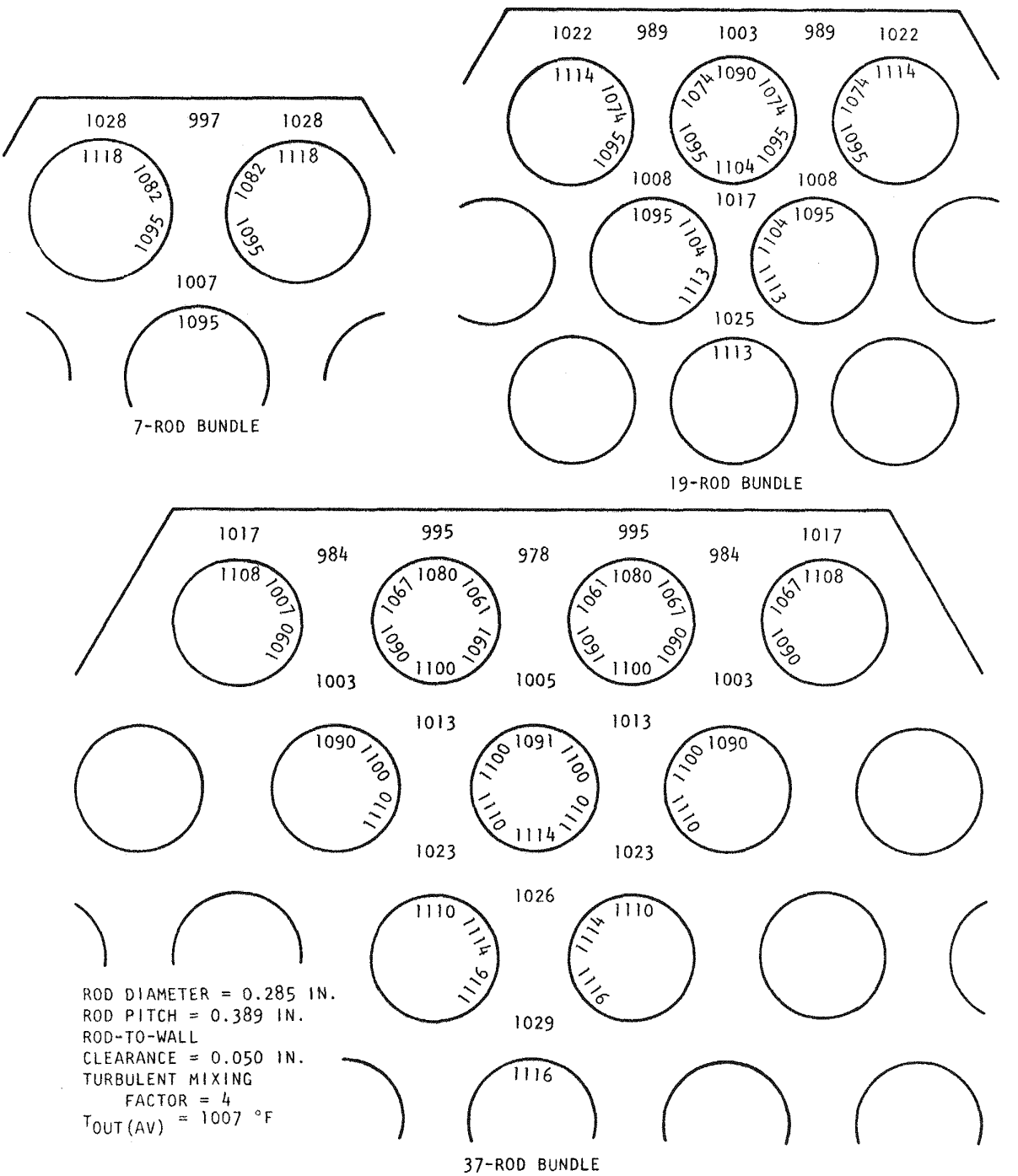

Fig. 3.19 Coolant and cladding temperatures for uniform rod bundles

summarized in Table 3.3. The results are similar to the calculations using uniform heating. The peak cladding temperature is lower but the spread of temperatures is slightly greater. Neither the sinusoidal heating distribution nor the spacers appears to have a large effect on the peak temperatures.

3.1.3. Fuel-rod–Spacer Interaction Tests

The purpose of this test program is to evaluate the mechanical interaction between the spacer-grid dimple and the fuel-rod cladding surface and to provide data for the design of the spacer grid. The problem, the test criteria, and test program were described in the previous quarterly report.[1] Work during this reporting period focused on the design of the test apparatus.

A schematic layout of the apparatus is shown in Fig. 3.20. A single cell of the hexagonal spacer (see Fig. 3.21) is held in a square block that is supported by thin beams (see Fig. 3.22). These beams are attached to a tube which in turn is attached to the left flange shown in Fig. 3.20. The thin beams resist movement of the spacer-grid cell axially along the fuel rod and allow deflection at right angles to the tube axis for the applied load.

The method of load application received a good deal of attention as the load levels are small—0.3 to 3 lb—and small high-temperature (750°C) load cells are difficult to make. The most simple loading concept is the use of a dead weight. This concept appeared suitable for the lower load ranges, but at the higher load ranges a long block of material would have to be used because of the small diameter of the furnace tube; balancing this long weight on a single spacer cell would be difficult. A possible variation is the use of two spacer cells coupled together. This longer load-bearing span would ease the problem of balancing a large dead weight. A design was also considered in which the load is applied through the use of a gas bellows. However, the use of gas bellows for low loads introduces calibration difficulties, including uncertainties in the unloading effects due to extension of the bellows and deflections of the beams supporting the spacer holder. Consequently, dead weight loading schemes are still being considered.

Table 3.3

COOLANT AND CLADDING TEMPERATURES OF SEVEN-ROD BUNDLE WITH GCFR OPERATING CONDITIONS

Rod diameter	0.285 in.
Rod pitch	0.385 in.
Rod-to-wall clearance	0.056 in.
Total rod length	88.0 in.
Core length	40.0 in.
Power distribution	Chopped cosine
Extrapolation length	7.9 in.
Number of spacers	8
Inlet temperature	590°F
Outlet temperature, ave.	1007°F
Reynolds number, ave.	105,000

Coolant and Cladding Temperatures (°F)

Distance from Inlet (in.)	Axial Position	Location in Hexagonal Bundle					
		Center		Wall		Wall Corner	
		Coolant	Cladding	Coolant	Cladding	Coolant	Cladding
0.0	Bundle inlet	590	590	590	590	590	590
30.0	Core inlet	590	770	590	779	590	779
40.6	Above rod roughening	668	966	656	972	683	1018
42.9	Roughened	693	854	679	848	717	882
50.0	Center of core (max. heat flux)	780	961	758	932	798	983
67.7	Maximum cladding temperature	987	1084	963	1056	992	1089
70.0	Core outlet	1002	1079	980	1054	1007	1085
88.0	Bundle outlet	1008	1008	1006	1006	1006	1006

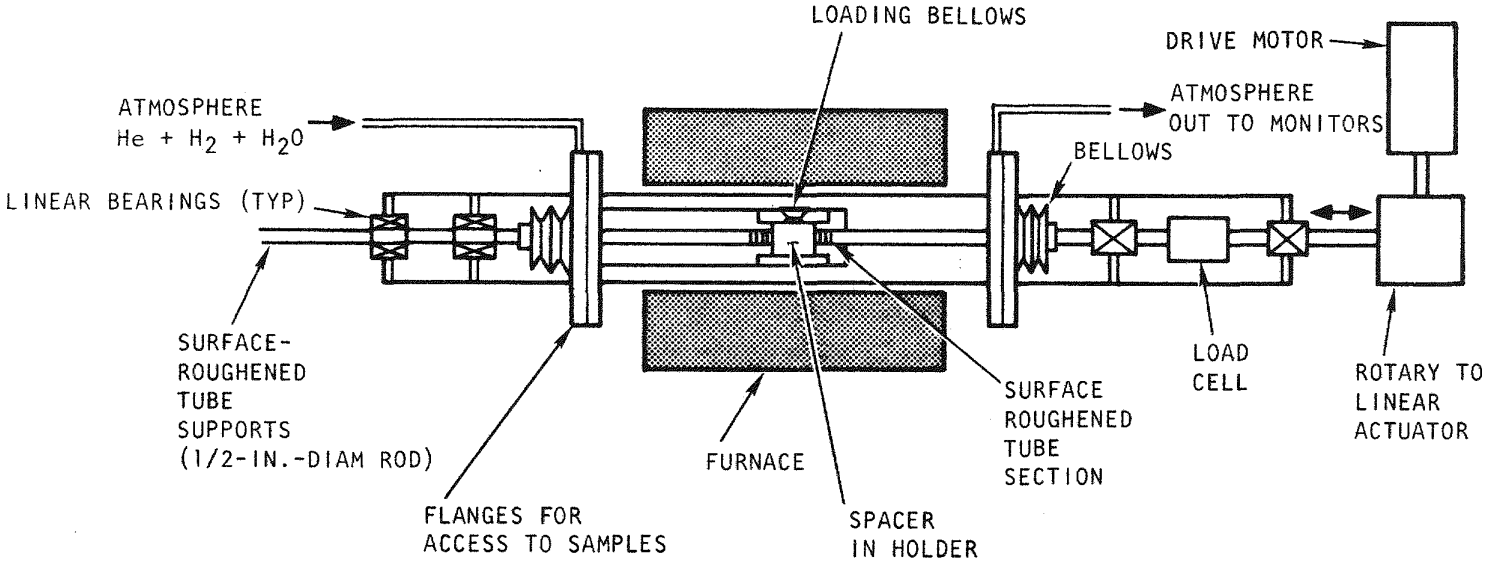

Fig. 3.20 Schematic of test setup for fretting-wear test of spacer and rod samples

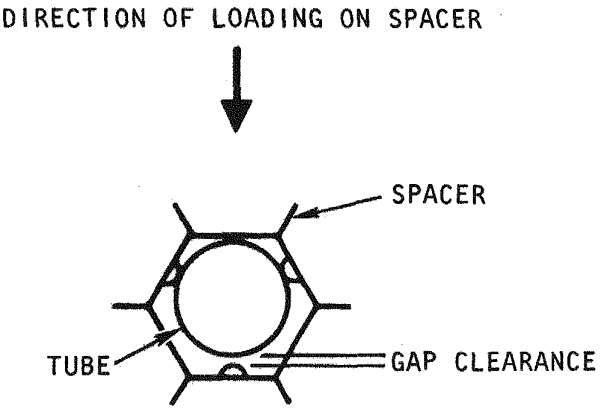

Fig. 3.21 Schematic of spacer loading force on sample tube

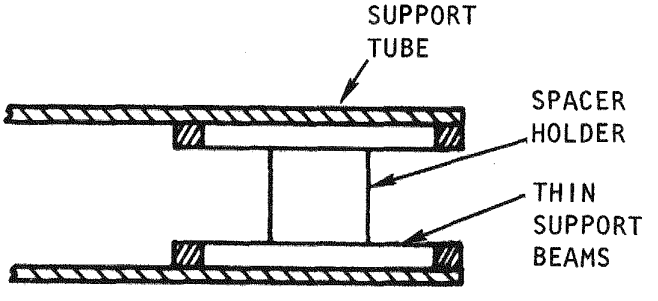

Fig. 3.22 Schematic of loading scheme for gas-bellows loading of spacer

As shown in Fig. 3.20, the load will be applied normal to the tube axis. The axial motion will be provided by a reversible electric motor driving a rotary-to-linear actuator connected through a load cell to one of the 1/2-in.-diam rods supporting the tube (see Fig. 3.20). Limit switches will control the stroke length and the initiation of each cycle will be controlled by a timer. Each of these support rods run in two linear bearings to maintain alignment of the system. The axial load, differential pressure representing normal load, and the number of cycles will be recorded.

The gas system that has been designed is planned to remove all impurities except H_2 from the He gas used. Controlled amounts of H_2 will be added to the He to give the desired H_2/H_2O ratio. The technique to be used in generating the desired H_2O level in the furnace atmosphere will be to pass the He-H_2 mixture over hot CuO (650°C) where the H_2 will be completely reacted to H_2O. This mixture will then be mixed with another He-H_2 gas mixture to produce the desired He-H_2-H_2O mixture. The resulting gas will pass through a Panametrics moisture sensor to measure H_2O content and then through a Thermox O_2 sensor, which, in the absence of O_2, will measure the H_2/H_2O ratio. The gas, after being admitted to the furnace near the test spacer, will be sampled on leaving the test furnace for changes in H_2 or H_2O. A simplified schematic of the gas system is shown in Fig. 3.23; not shown are valves, pressure regulators, or flowmeters. A preliminary setup has been made and is now being checked out to determine if the desired H_2O levels can be achieved.

All major components of the test apparatus have been received or shipped and fabrication of the test fixtures is scheduled to be started by the end of this quarterly period. The preparation of test specifications has also been initiated, and a quality assurance project plan will be prepared.

3.2. FUEL- AND BLANKET-ROD MODELING STUDIES

Fuel modeling studies are directed toward developing a design technique for predicting GCFR fuel- and blanket-rod behavior. The fast and thermal irradiations of GCFR are being used to test the calculated predictions with respect to rod diameter expansion. This modeling work is concentrated on using

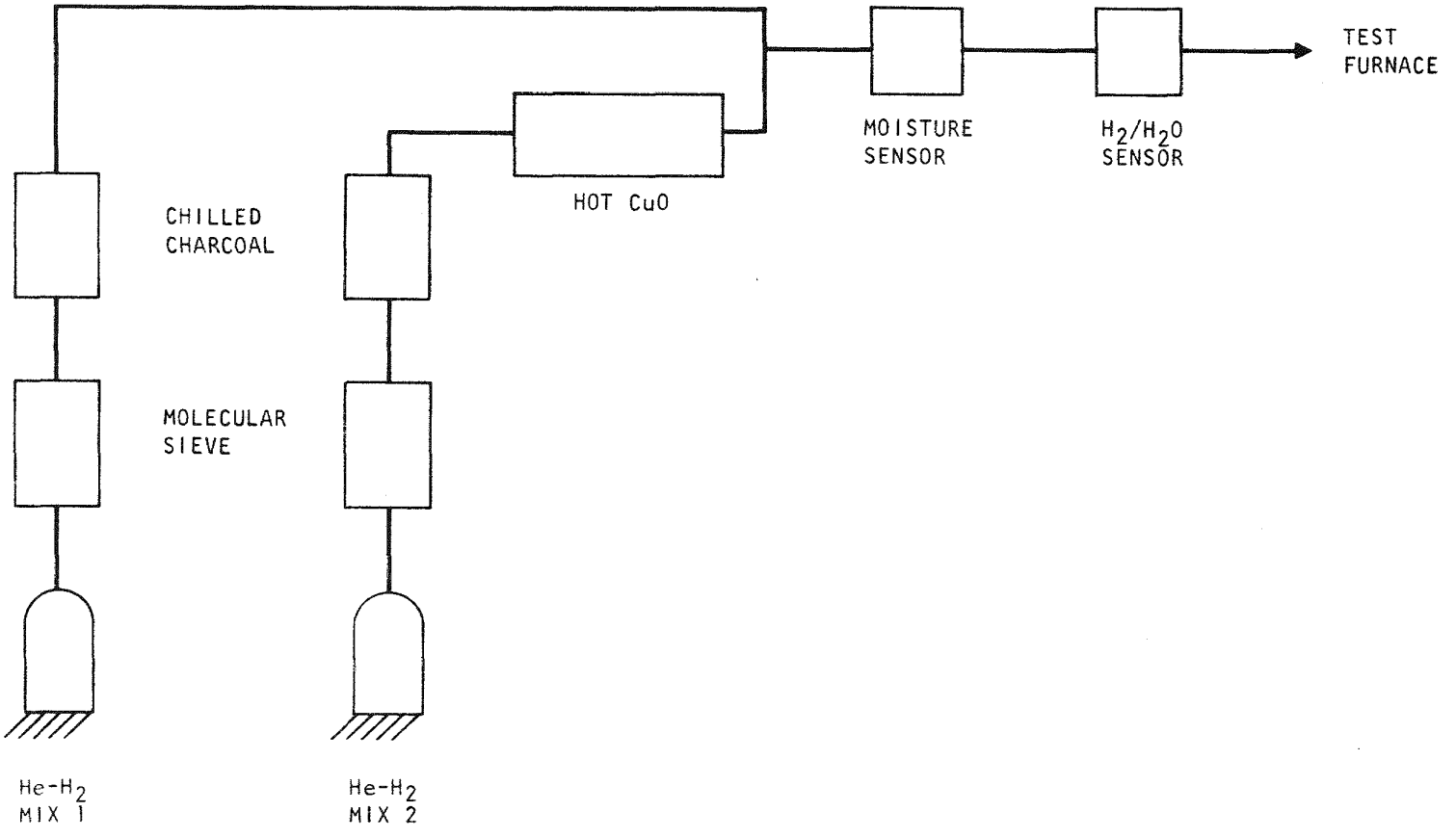

Fig. 3.23 Simplified schematic of gas system for spacer-grid–rod interactions tests

the LIFE-II code, which has been selected for development by the LMFBR project.

3.2.1. Fuel-rod Modeling Committee

At a meeting of the LMFBR Fuel-rod Modeling Committee in Washington, D.C., on October 11-12, 1972, a joint effort by all LMFBR contractors on the LIFE-II program was initiated. The first step in this program will be for ANL to issue a third revision of the code, which will be a calibrated version of the second revision.

3.2.2. Effects of Revision of LIFE-II on Predictions

The changes to the LIFE-II code, described as Revision No. 2,[14] were incorporated and no problems were encountered in running the sample program; the running time was approximately unchanged.

The results obtained with the updated code are compared in Table 3.4 with those obtained with the old code. Calculation A was made with Revision 1 of the LIFE-II code. For calculation B, the only difference from the old code is a correction in the calculation of fuel temperatures using the Biancheria fuel conductivity. For calculation C, the recommended Revision 2 options were used, as follows:

1. A new expression for creep of 20% cold-worked 316 stainless steel, suggested by Brian Harbourne of WARD, is used (NCRC = -4).
2. A new fuel creep expression is used, based on ANL thermal creep, BMI fission-enhanced creep, and GE porosity dependence (NCRF = 1).
3. Fuel swelling is computed with revised constants for hot-pressing based on the volume diffusion coefficient rather than on the surface diffusion coefficient (NSWL = 2). The result is a greatly reduced rate of hot-pressing.

From Table 3.5, the following results are noted:

1. The change in fuel temperature calculation (comparing calculation B with A) reduced the maximum fuel temperature about 250°F at 49 hr, and about 130°F at 1049 hr.
2. The fuel-cladding gap tended to close sooner when the revised hot-pressing relation was used. For example,

Table 3.4

EFFECT OF LIFE-II REVISION 2 CHANGES ON TEST PROBLEM

	49 hr			549 hr			1049 hr		
	A[a]	B[a]	C[a]	A	B	C	A	B	C
Max. fuel temp., °F	4703	4456	3983	3740	3613	3721	3723	3593	3711
Fuel-cladding gap, mil	0.525	0.625	0	0	0	0	0	0	0
Hot-pressing: (linear strain)									
Columnar	-0.151×10^{-2}	-0.151×10^{-2}	-0.728×10^{-8}	-0.151×10^{-2}	-0.151×10^{-2}	-0.243×10^{-3}	-0.151×10^{-2}	-0.151×10^{-2}	-0.109×10^{-2}
Equiaxed	-0.100×10^{-1}	-0.100×10^{-1}	-0.834×10^{-7}	-0.100×10^{-1}	-0.100×10^{-1}	-0.123×10^{-4}	-0.100×10^{-1}	-0.100×10^{-1}	-0.174×10^{-4}
Undisturbed	-0.380×10^{-2}	-0.440×10^{-2}	-0.629×10^{-3}	-0.380×10^{-2}	-0.475×10^{-2}	0.629×10^{-3}	-0.936×10^{-2}	-0.936×10^{-2}	0.629×10^{-3}
Swelling									
Columnar	-0.122×10^{-2}	-0.121×10^{-2}	0.173×10^{-5}	0.486×10^{-2}	0.443×10^{-2}	0.777×10^{-2}	0.620×10^{-2}	0.608×10^{-2}	0.379×10^{-2}
Equiaxed	-0.992×10^{-2}	-0.992×10^{-2}	0.112×10^{-4}	-0.168×10^{-3}	0.123×10^{-2}	0.382×10^{-2}	0.183×10^{-2}	0.310×10^{-2}	0.677×10^{-2}
Undisturbed	-0.380×10^{-2}	-0.440×10^{-2}	0.630×10^{-3}	-0.280×10^{-2}	-0.365×10^{-2}	0.162×10^{-2}	-0.740×10^{-2}	-0.749×10^{-2}	0.249×10^{-2}
Swelling excluding hot-pressing									
Columnar	0.274×10^{-2}	0.273×10^{-2}	0.174×10^{-5}	0.637×10^{-2}	0.594×10^{-2}	0.801×10^{-2}	0.771×10^{-2}	0.759×10^{-2}	0.489×10^{-2}
Equiaxed	0.810×10^{-4}	0.821×10^{-4}	0.113×10^{-4}	0.983×10^{-2}	0.112×10^{-1}	0.383×10^{-2}	0.118×10^{-1}	0.131×10^{-1}	0.679×10^{-2}
Undisturbed	0.722×10^{-6}	0.152×10^{-5}	0.124×10^{-5}	0.100×10^{-2}	0.110×10^{-2}	0.987×10^{-3}	0.196×10^{-2}	0.215×10^{-2}	0.186×10^{-2}
Cladding creep									
Thermal	0.189×10^{-20}	0.217×10^{-20}	0.749×10^{-14}	0.229×10^{-4}	0.981×10^{-5}	0.198×10^{-3}	0.683×10^{-3}	0.479×10^{-3}	0.181×10^{-2}
Irradiation	0.104×10^{-10}	0.117×10^{-10}	0.894×10^{-6}	0.395×10^{-7}	0.342×10^{-7}	0.125×10^{-2}	0.122×10^{-6}	0.114×10^{-6}	0.246×10^{-2}
Equiv. cladding stress (SIGCEQ)	------	226	11,361	------	16,055	52,362	------	25,761	57,525
% ΔD/D	0.880	0.880	0.920	0.949	0.940	1.193	1.044	1.023	1.466

[a]Calculations:

A = Revision 1,

B = Revision 2 with Revision 1 options (corrected fuel temperature),

C = Revision 2 with Revision 2 options (new cladding creep, new fuel creep, and new hot-pressing).

Calculation	A	B	C
Gap closing, hr	90	97	49

3. The new calculation (C) resulted in greater cladding thermal creep and much greater cladding irradiation creep. Apparently the former relation was in error, possibly a factor of 3600 in seconds per hour.

4. The "minor" corrections in the fuel-swelling calculation must have had some effect, since there is a considerable difference in the net swelling (not including hot-pressing) in the new calculation.

3.2.3. Model Calculations on GB-9 Rod Using LIFE-II Revision 2

Revision 2 of the LIFE-II code contains a revised hot-pressing relation that will have a strong effect on the net fuel swelling during early life. The use of the old hot-pressing relation delayed closure of the fuel-cladding gap sufficiently so that the creep expansion of the cladding was negligible. Since the newer relation predicts much slower hot-pressing, the resulting cladding expansion would be expected to be larger.

The predicted rod expansion versus fuel burnup, in % of metal atoms, using LIFE-II Revision 2 is shown in Fig. 3.24. Curve 1 is the prediction using standard assumptions, including the new recommended fuel thermal conductivity, which results in lower fuel temperatures. Curve 2, for which the hot-pressing was suppressed, shows a considerably greater expansion, as would be expected.

The predicted expansion using standard assumptions and the old GE fuel conductivity expression is shown by curve 3. Apparently the smaller rod expansion is a result of a reduction in fuel swelling in the hotter central zone. For example, at a burnup of 5.7% the calculated results for the columnar zone are as follows:

	New Conductivity	Old Conductivity
Total fuel swelling, %	3.240	2.569
Fuel hot-pressing, %	2.545	2.367
Net linear fuel swelling, %	0.695	0.202
Average temperature, columnar zone, °F	3682	3927
Maximum fuel temperature, °F	4108	4705
Fraction of fuel in columnar zone	0.548	0.656

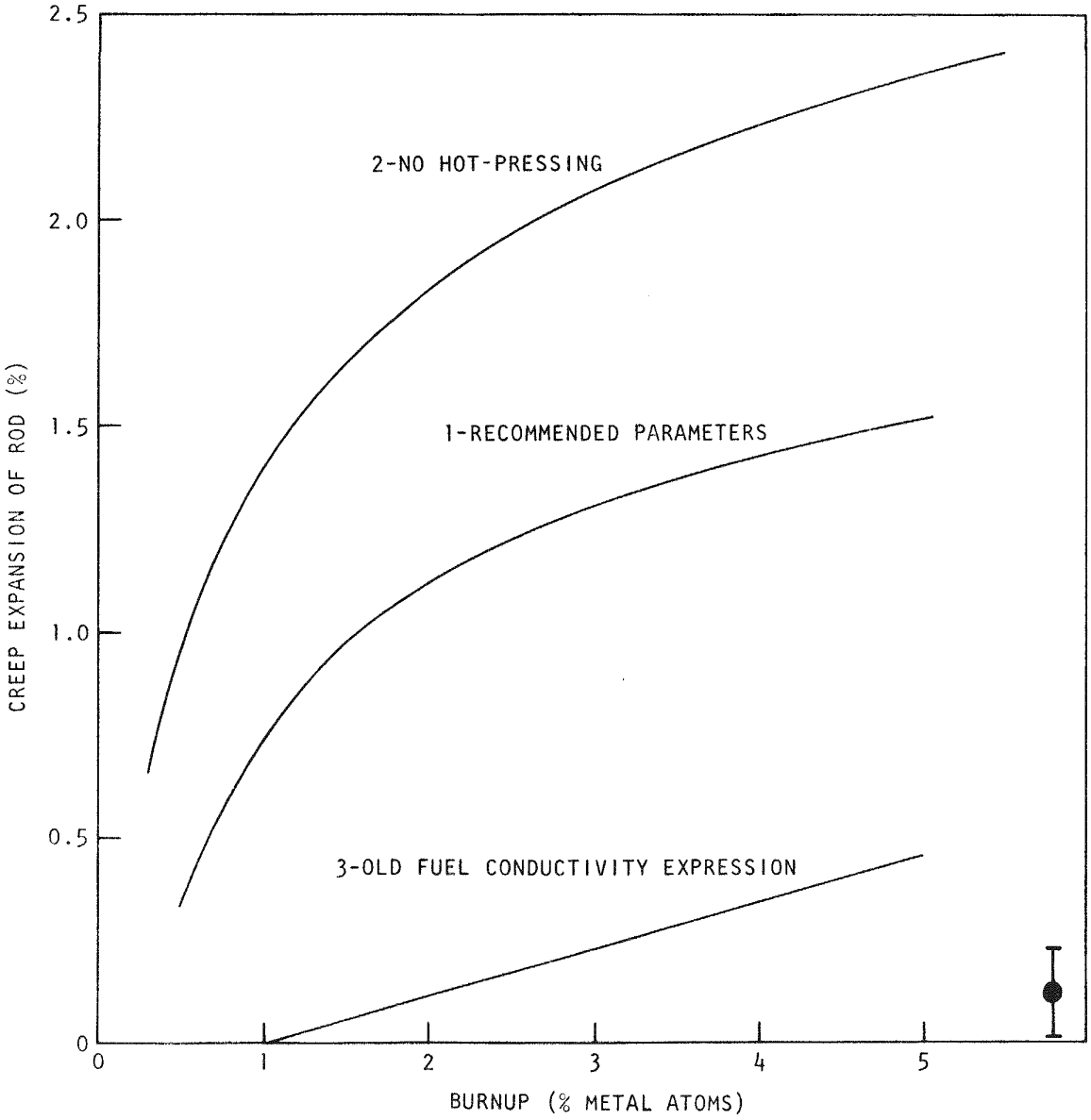

Fig. 3.24 Predicted expansion of GB-9 rod using LIFE-II Revision 2

Since fuel swelling and hot-pressing are roughly equal at this burnup (5.7%), small changes in either of those quantities could produce large fractional changes in the net swelling and appreciable differences in cladding deformation. It should be noted that measurements on the GB-9 rod indicated negligible diameter expansion at the end of the irradiation (~5% burnup) and thus none of the calculations is in agreement with that experiment.

3.2.4. Preliminary Calculations for High-power Rods in the F-3 Capsule Experiment

Attempts to run a LIFE-II calculation for the highest-powered fuel rods of the F-3 irradiation experiment (see Section 5.2) led to a number of problems. The conditions causing the problems appeared to be

1. High-density fuel (92% TD),
2. Small radial fuel-to-cladding gap (0.0016 in.),
3. Solid fuel pellets, and
4. High heat-generation rating (16.8 kW/ft).

Three separate code corrections were found to be necessary to run this calculation. These corrections, along with various other modifications, will be included in the next official revision of LIFE-II (Revision 3).

The results of this case show the fuel to be close to the melting temperature at the start (4871°F center) even though the fuel-cladding gap closes during the rise to power. At 3.3% burnup, or 4110 hr, the cladding creep expansion is 1.8%, of which 0.41% is due to irradiation-induced creep and the remainder is due to thermal creep. The fuel central hole increases from the nominal input value of 0.001 in. to 0.0027 in., a practically negligible change.

3.3. LOWER THERMAL SHIELD ASSEMBLY

Previous work on this task consisted of evaluated conceptual designs of the lower shield assembly for design base situations involving small quantities of fuel debris and for a postulated melted core situation.

One of the main conclusions of the melted-core containment feasibility evaluation was that a large fraction (on the order of 60% to 80%) of the decay heat must be removed upward from the top surface of the debris because

the downward flow of heat is limited by the low thermal conductivity of the fuel.

The current effort is focused on assessing the feasibility of removing heat from the top surface of the debris. Included in these studies are considerations of mass transfer and heat transfer resulting from vaporization and subsequent condensation of fission products and fuel debris. Also considered will be the contributions of natural circulation and forced circulation under various combinations of pressurized and depressurized conditions.

As a first step in this feasibility evaluation, the potential contribution of natural circulation through the auxiliary loops while the reactor remains pressurized has been evaluated. Analysis of this case is based on the following considerations. With core debris in the annular tray underneath the radial thermal shield, a natural convection flow path would exist because of the substantial difference in the elevation between the auxiliary loop heat exchanger and the annular debris tray. The helium would heat up above the debris tray and flow upward through the central cavity and through the auxiliary loops in the reverse direction. This flow path is shown schematically in Fig. 3.25. The helium would be cooled in passing downward through the auxiliary loop heat exchanger. The density difference between the cold helium leg below the heat exchanger and the hot helium leg in the central cavity provides the driving force for the natural convection.

The following initial conditions are assumed to exist:

1. The core has dropped to the bottom of the central cavity and has collected in the annular debris tray without causing substantial damage to the upper large-diameter section of the shield cylinders above the debris tray.

2. The auxiliary loop isolation valves are in the open position and the auxiliary circulators are inoperative (which would require modification of the reference design valves to permit mechanical actuation.

3. Cooling water is circulated through the auxiliary loop heat exchangers at the flow rate, pressure, and inlet temperature

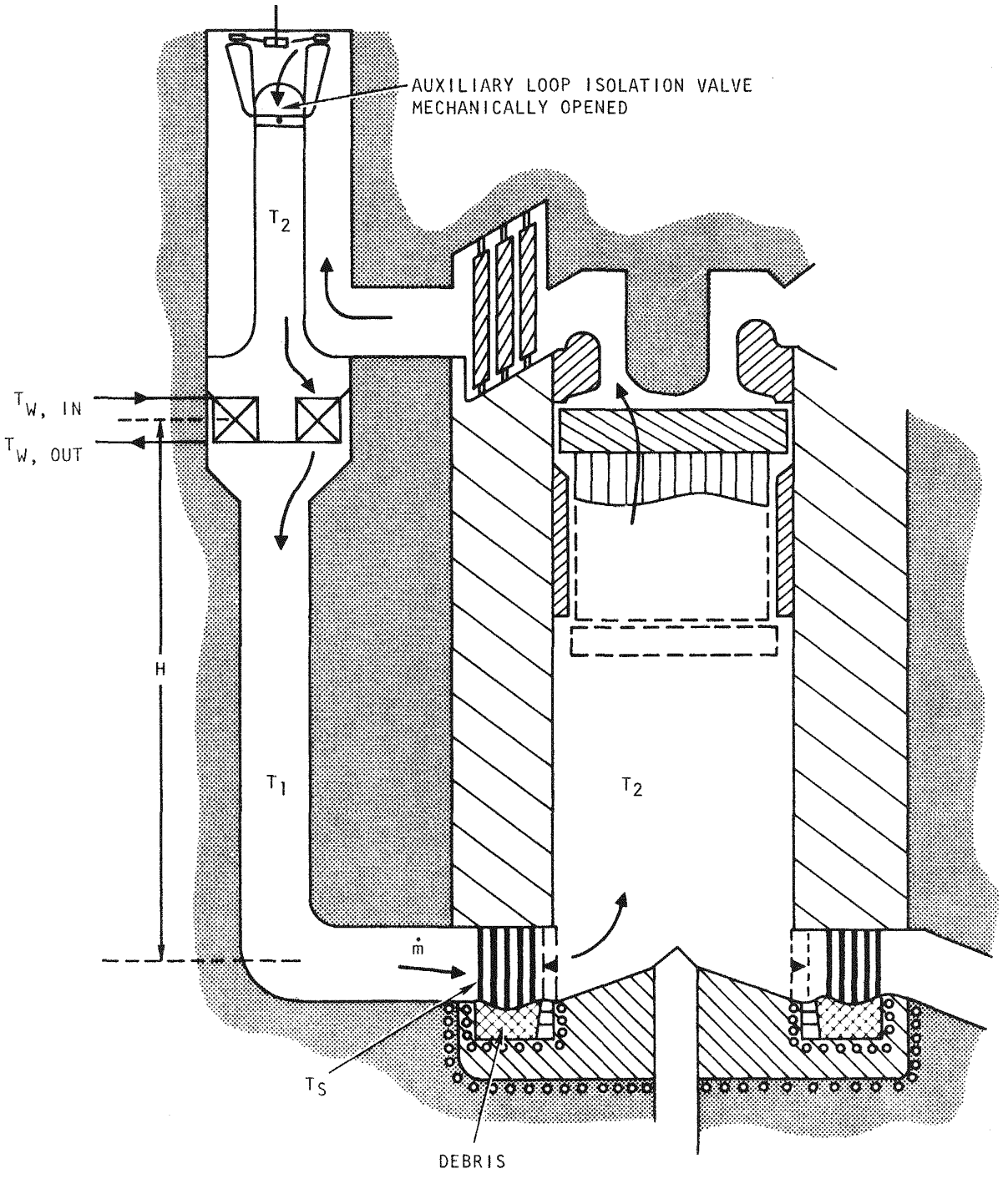

Fig. 3.25 Natural-convection flow path through auxiliary loop

specified in the design basis (i.e., the auxiliary heat-dump loops work normally, although the auxiliary circulators do not).

4. The primary system pressure is and remains at 1250 psia.

5. All of the helium heating is assumed to take place above the debris tray from a surface temperature, T_S, of 2600°F.

The heat-removal capability of natural circulation has been determined for several different flow paths above the debris. The shield cylinder arrangement above the debris tray consists of five circular rows of cylinders, each consisting of 84 cylinders. The shield cylinders in the outer rows have a larger diameter than those in the inner rows, and the diameter of the cylinders in the middle row was used in the calculations for all rows. The diameter of a cross-over duct corresponds to the width of about 6 cylinders in each row.

For the reference design with the annular debris tray, the coolant flow is assumed to exit from the cross-over duct and to fan out such that effective and equal cooling of 10 cylinders in each row is achieved, with the helium flowing equally through the 10 gaps between the cylinders. The flow direction is primarily radially inward, with an effective flow width above the debris of about 1.67 times the cross-over duct diameter.

For this case, the following operating conditions for loop balanced heat removal by natural convection were determined (the heat removed is expressed as a percentage of the nominal full reactor power, P_0 = 926.5 MW(t)):

Heat removed:	$\dot{Q}/P_0$ = 0.84% per loop,
	= 2.52% total,
Mass flow:	$\dot{m}$ = 13.6 lbm/sec per loop
	= 40.8 lbm/sec total,
Cold helium temperature:	T_1 = 385°F,
Hot helium temperature:	T_2 = 775°F,
Water outlet temperature:	$T_{w,\ out}$ = 320°F,
Reynolds numbers	
In cold leg pipe:	2.7×10^5
In debris tray:	5.1×10^4
In heat exchanger:	4.9×10^3

If 100% of the decay heat is to be removed in the upward direction, then natural convection in this mode could remove all the decay heat after 19 or 20 min. If 80% of the total decay heat is removed upward, and 20% is removed downward, then the total decay heat could be removed after 8 or 9 min. This includes the decay heat from the volatile and gaseous fission products, since it was assumed that all helium heating takes place above the debris. The minimum time required for the core to disassemble and relocate into the debris tray is estimated to be about 5 to 10 min. The helium temperatures for this case are quite low, which means that the temperatures throughout the PCRV would be acceptable.

As a second flow configuration, it was assumed that the helium flow was also radially inward, but that all cylinders in the tray were cooled with equal effectiveness. This flow mode could be approximated if flow from the auxiliary loop cross-over ducts could be distributed over the entire circumference.

The loop balanced natural convection operating conditions for this case are:

Heat removed:	$\dot{Q}/P_0$ = 1.17% per loop
	= 3.50% total
Mass flow:	$\dot{m}$ = 13.1 lb/sec per loop
	= 39.4 lb/sec total
Cold helium temperature:	T_1 = 445°F
Hot helium temperature:	T_2 = 1006°F
Water outlet temperature:	$T_{w,\ out}$ = 374°F
Reynolds numbers	
In cold leg pipe:	2.4×10^5
In debris tray:	4.5×10^4
In heat exchanger:	4.3×10^3

In this flow mode, all of the decay heat released after 5 to 6 min can be removed, or 80% of the decay heat can be removed after 1.5 to 2 min. The hot helium temperature is the same as the mixed mean outlet temperature in the normal operating condition and thus the temperatures within the PCRV would be well within the acceptable range. The flow is again turbulent.

As a third flow configuration, the helium flow path in the debris tray was assumed to be primarily in the circumferential direction. Helium was assumed to enter the tray from the cross-over duct and then turn 90° to flow around the tray for one-sixth of the circumference, where it would make another 90° turn to exit into the central cavity.

This flow path could be approximated by providing flow barriers or restrictors between the shield cylinders, which would guide the flow in the radial direction. Also a shroud in front of the innermost row of cylinders with appropriate openings could aid in redirecting the flow. Care would have to be taken in the design of this shroud to still permit efficient entry of the debris into the debris tray.

The balanced natural convection operating conditions for this case are:

Heat removed:	$\dot{Q}/P_0$ = 1.78% per loop
	= 5.34% total
Mass flow:	$\dot{m}$ = 11.75 lb/sec per loop
	= 35.25 lb/sec total
Cold helium temperature:	T_1 = 577°F
Hot helium temperature:	T_2 = 1533°F
Water outlet temperature:	$T_{w,\ out}$ = 475°F
Reynolds number	
In cold leg pipe:	1.8×10^5
In debris tray:	3.4×10^4
In heat exchanger:	3.3×10^3

In this flow mode, all of the decay heat released after about 1 min can be removed by natural convection; however, the maximum helium temperature is 1500° to 1600°F.

The following are tentative conclusions based on the foregoing analyses:

1. Assuming failed main loops, failed auxiliary circulators, but operating auxiliary heat-dump loops and a pressurized PCRV, natural-convection heat removal could substantially assist the decay heat removal from a melted core in the debris tray if the auxiliary loop isolation valves can be opened mechanically.

2. The current reference design of the lower thermal shield assembly represents a good geometry for natural convection heat removal. With the above assumed conditions, it appears that 80% of the total decay heat could be removed by natural convection after about 8 to 10 min.

These feasibility evaluations are being extended to other assumptions regarding equipment availability and PCRV pressure.

REFERENCES

1. "Gas-Cooled Fast Breeder Reactor Quarterly Progress Report for the Period August 1, 1972 through October 31, 1972," USAEC, Report GA-A12421, Gulf General Atomic, December 8, 1972.

2. Sutherland, W. H., and V. B. Wotwood, Jr., "Creep Analysis of Statically Indeterminate Beams—CRASIB, Users Guide and Program Manual," USAEC, Report BNWL-1362, Battelle Northwest Laboratories, June 1970.

3. Hopkins, H. C., D. Buttemer, and J. B. Dee, "Accommodation of Radiation Swelling in the GCFR," Trans. Am. Nucl. Soc., Vol. 13, No. 2, November 15, 1972, pp. 776-777.

4. "Gas-Cooled Fast Breeder Reactor Quarterly Progress Report for the Period May 1, 1972 through July 31, 1972," USAEC, Report GA-A12252, Gulf General Atomic, August 31, 1972, p. 12-13.

5. "Oxide Fuel Element Development Quarterly Progress Report for Period Ending June 30, 1972," USAEC, Report WARD-3045 T3-7, Westinghouse Electric Co., September 1972, pp. 13-45 and 13-47.

6. "Oxide Fuel Element Development Quarterly Progress Report for Period Ending June 30, 1971," USAEC, Report WARD-3045 T3-7, Westinghouse Electric Co., September 1971, pp. 12-19 and 12-20.

7. "Oxide Fuel Element Development Quarterly Progress Report for Period Ending June 30, 1970," USAEC, Report WARD-4135-11, Westinghouse Electric Co., September 1970, p. 7-26.

8. "Gas-Cooled Fast Breeder Reactor Quarterly Progress Report for the Period February 1, 1972 through April 30, 1972," USAEC, Report GA-A12165, Gulf General Atomic, July 20, 1972.

9. Roark, R. J., Formulas for Stress and Strain, 4th Edition, McGraw-Hill Book Co., 1965.

10. Rowe, D. S., "COBRA-II: A Digital Computer Program for Thermal-Hydraulic Subchannel Analysis of Rod Bundle Nuclear Fuel Elements," USAEC, Report BNWL-1229, Battelle Northwest Laboratory, February 1970.

11. "HECTIC-II, An IBM-7090 Fortran Computer Program for Heat-Transfer Analysis of Gas- or Liquid-Cooled Reactor Passages," USAEC, Report IDO-28595, Rev., December 1965.

12. "SCEPTIC (SCEPTC), A FORTRAN IV Computer Program for Temperature Analysis of Gas or Liquid Cooled Flow Passages with Heated Smooth or Roughened Surfaces," TM-IN-479, Swiss Federal Institute for Reactor Research, July 16, 1971.

13. Ingesson, L., and S. Hedberg, "Heat Transfer Between Subchannels in a Rod Bundle," Proceedings Fourth International Heat Transfer Conference, Paris, 1970, Vol. III, Paper FC 7.11.

14. Jankus, V. Z., and R. B. Peoppel, Argonne National Laboratory, Revision Letter #2 and Attachments, September 18, 1972.

4. TASK 4160—PRESSURE EQUALIZATION SYSTEM FOR FUEL

All efforts during this reporting period were focused on preparation of a planning document for the fuel pressure equalization system (PES) in which the various aspects that are important in the development of the PES for the GCFR are coordinated. As a reference basis, the design concepts have been applied to a 300-MW(e) GCFR and the planning of the development of the PES has been related to the overall development program plan for the total GCFR nuclear steam supply system.

The development planning document for the PES covers (1) the preliminary functional, design, and performance criteria, (2) a system design description, (3) an evaluation of the system design with respect to the criteria established, and (4) a development program and schedule. A draft of this document has been completed and submitted to the Division of Reactor Development and Technology for review.

5. TASK 4200/4400—FUELS AND MATERIALS DEVELOPMENT

5.1. THERMAL-FLUX IRRADIATION EXPERIMENTS

5.1.1. Irradiation Capsule GB-9

No further postirradiation examination at Argonne National Laboratory (ANL) of the vented fuel rod irradiated in ORR capsule GB-9 was carried out during this quarter.

As reported previously,[1] a burst test at 700°C and 3000 psi was performed on the GB-9 fuel-rod cladding. Metallography of the fracture region of the burst-test sample from the GB-9 cladding indicates that the failure may have been intergranular through ~80% of the wall thickness and transgranular through ~20% of the wall thickness. The grains in the outer 20% region appear elongated, indicating significant ductility in the outer region (see Fig. 5.1). The fuel in the fracture region of this sample appears as a ring of apparently densified fuel adjacent to the outer edge of the equiaxed grain region (see Fig. 5.2), and the grain size in the equiaxed region is smaller than in the fuel-rod sections that had not been subjected to burst testing and heating. Annealing tests will be performed on the GB-9 fuel specimens not subjected to burst-testing pressure to determine whether the burst-test conditions may have caused the apparent densification.

The activated charcoal trap and Kr^{85} sample from GB-9 are ready for shipping to GGA for analysis.

5.1.2. Irradiation Capsule GB-10

Irradiation of the vented-fuel-rod, sweep-gas capsule experiment GB-10, which started on August 9, 1972, has reached a burnup of ~12,000 MWd/Te. The rod is being operated initially at a linear heat-generation rating of 12 kW/ft until steady fission-gas release conditions are attained. After this initial period, the heat generation rate will be increased, possibly in two steps, to 14.8 kW/ft, at which level it will continue for the

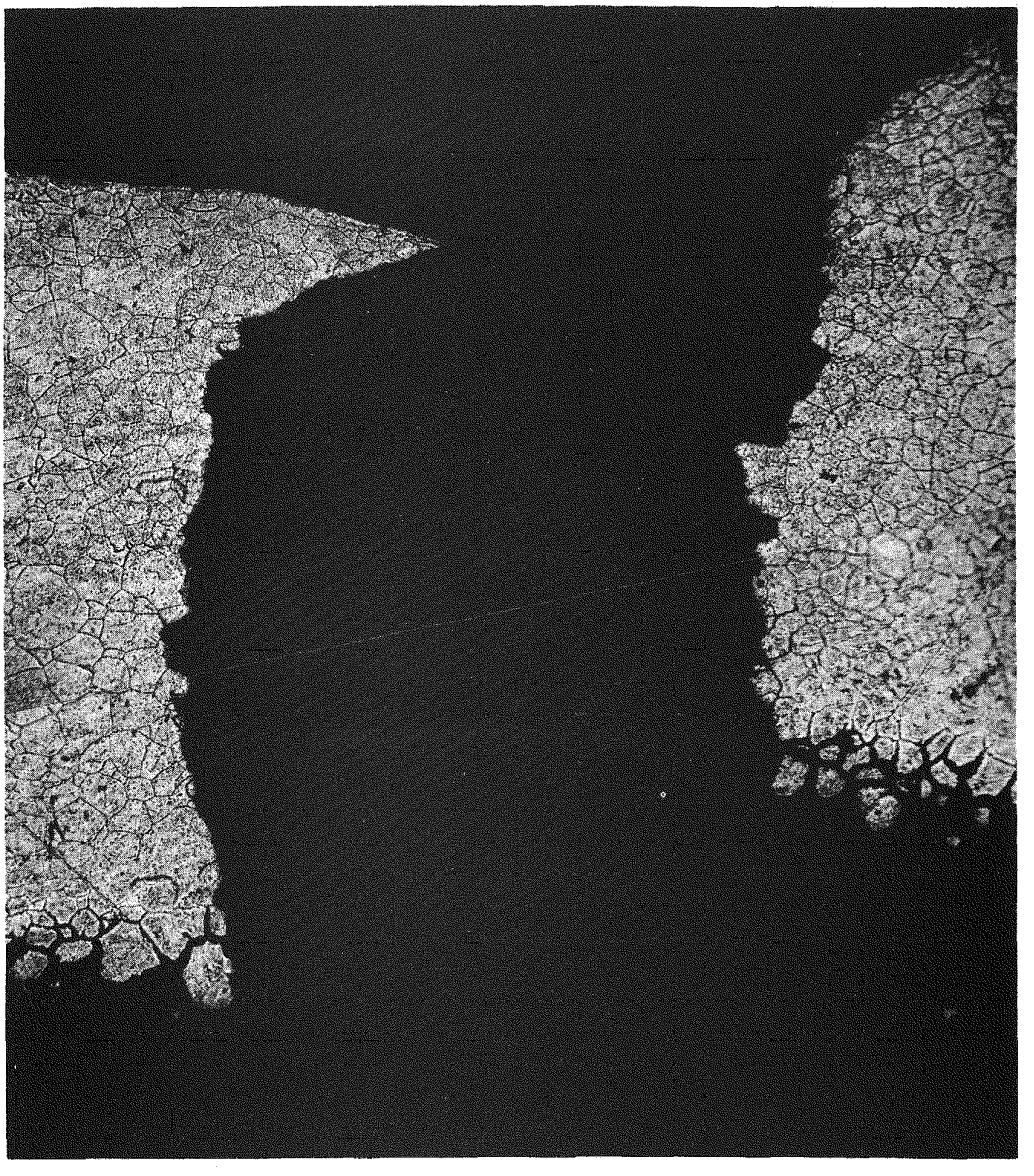

Fig. 5.1 Fracture region of GB-9 cladding burst-test sample showing intergranular failure to ~80% of cladding and transgranular failure through remainder

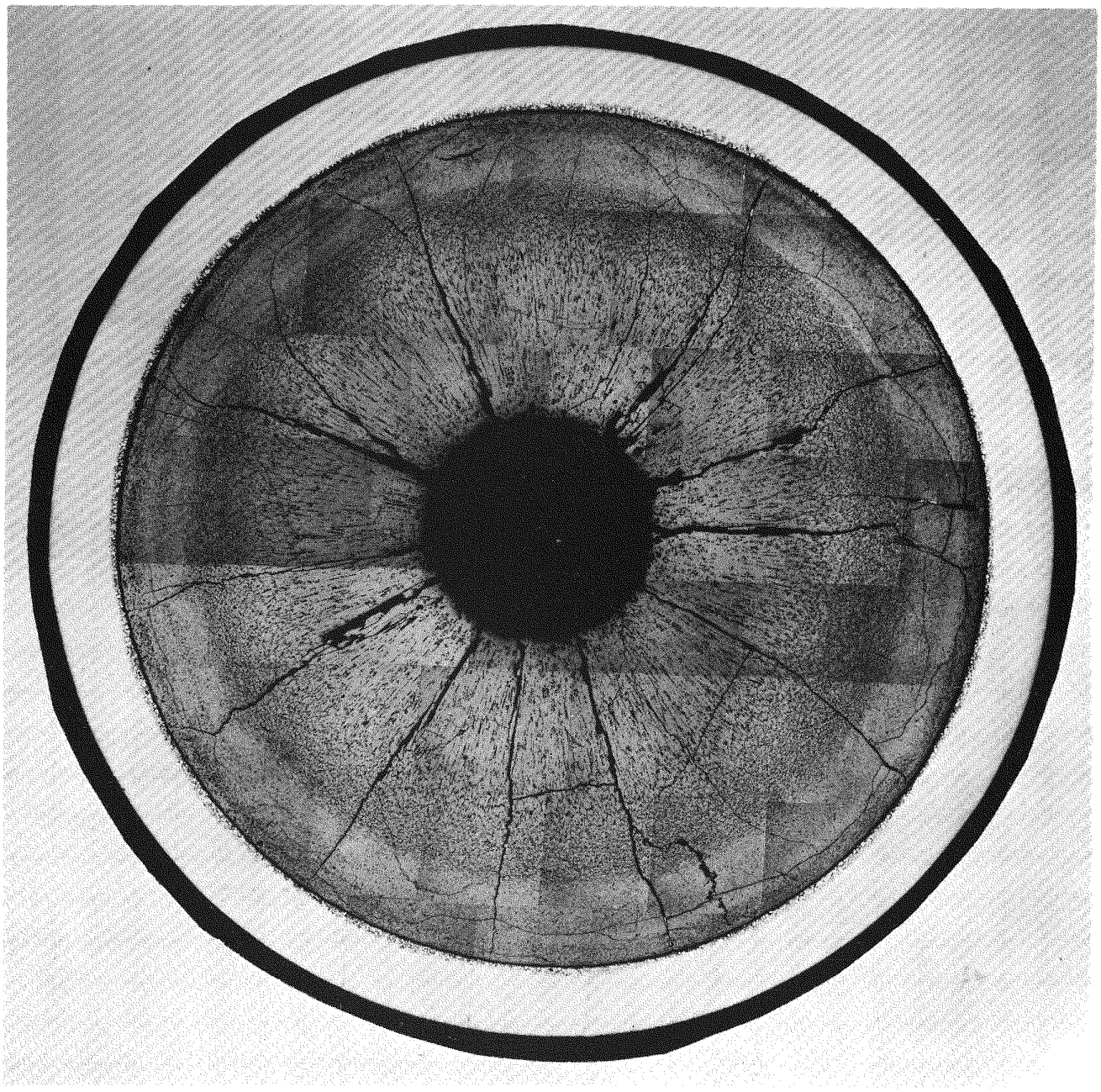

Fig. 5.2 Section of GB-9 burst-test sample taken above the bottom of fuel region which shows ring of densified fuel near outer portion of fuel

remainder of the exposure to a burnup goal of 75,000 MWd/Te.

On December 23, 1972, two overpower transients occurred in the ORR, both of which were of short duration. The first one reached 20% overpower (36 MW(t)) and the second 10% (33 MW(t)), after which the reactor was manually scrammed. Since the reactor period is reported to have been 17 sec, the overpower period was limited to a few seconds. At 20% overpower, irradiation capsule GB-10 operating at 12 kW/ft prior to the excursion would have reached a level of 14.5 kW/ft, which is less than its design point of 15 kW/ft. Thus, no damage to the fuel rod and capsule is expected or was observed. Fission-gas release data taken subsequent to the overpower transients does not appear to have been affected. The sample-line monitors measuring the activity of the gas sweeping through the sample line showed a transient pulse with a peak of double the pretransient level. The activity pulse may have resulted from exhalation of the gases within the rod or from an increase in the release of fission products from the oxide fuel as a result of increased temperature or from a combination of both.

A transient rise of the thermocouples monitoring the cladding outside temperature showed a maximum increase of about 20°C. In order to interpret the effect of the transient, a complex transient thermal analysis of the capsule will be done.

The data analyzed to date on the active fission-gas release from the GB-10 fuel rod during operation at the 12 kW/ft power level has been received from ORNL. Several flow modes were tested. These flow modes are designated by two letters to indicate the sweep gas entry point into the GB-10 rod followed by two more letters to indicate the exit point out of the rod. The letter symbols used are as follows:

TT - top of trap
BT - bottom of trap
BB - bottom of upper blanket
BF - bottom of fuel

The results for the following flow modes are reported:

TT - TT: In through the top of trap, out through top of trap,
TT - BT: In through the top of trap, out through bottom of trap,

TT - BB: In through the top of trap, out through bottom of blanket,

BF - BB: In through the bottom of fuel, out through bottom of blanket,

BT - TT: In through the bottom of trap, out through top of trap,

BF - TT: In through the bottom of fuel, out through top of trap.

The release fractions as a function of burnup are shown in Figs. 5.3 through 5.8. A comparison between release fractions obtained in the previously irradiated sweep-gas capsule GB-9 and those obtained in capsule GB-10 for the TT-TT flow mode is shown in Fig. 5.9. (Capsule GB-9 was limited to two flow modes whereas the arrangement of capsule GB-10 permits six flow modes, without counting reverse flow over the same pathways.) It is apparent that the release fractions from capsule GB-10 operating at 12 kW/ft are significantly lower than those in capsule GB-9 operating at 14.8 kW/ft. In addition, it should be noted that the initial minimum, which is very apparent in the GB-10 data up to burnups of about 10,000 MWd/Te, is both broader and deeper for GB-10 than that observed in capsule GB-9. In fact, it was necessary to go back to the early sample-line monitor data of GB-9 to be certain that similar transients occurred in that irradiation. It should also be noted that although the activity levels have not reached the saturation value after 10,000 MWd/Te burnup in capsule GB-10 at 12 kW/ft, steady values had essentially been reached in capsule GB-9 at that burnup level.

The release for all of the isotopes for which measurements were obtained from capsule GB-10 decreased during the first 30 days of irradiation (~2,900 MWd/Te) and then began to increase; steady-state levels of release have not yet been attained (based on monitor measurements of in-line activity). The initial decrease in release is thought to be due to the formation of a central hole in the fuel (solid pellets initially) and the closure of the fuel-cladding gap. It is hypothesized that the formation of the central hole and closure of the gap lowered the central and overall fuel temperatures and resulted in a lowered fractional release. Another effect the closure of the fuel-cladding gap may have is that it results in more delay in release of fission gases from the outer periphery of the fuel. During the initial irradiation period, most of the fissions occur in the outer periphery of the fuel because of self-shielding effects in the thermal flux in the ORR.

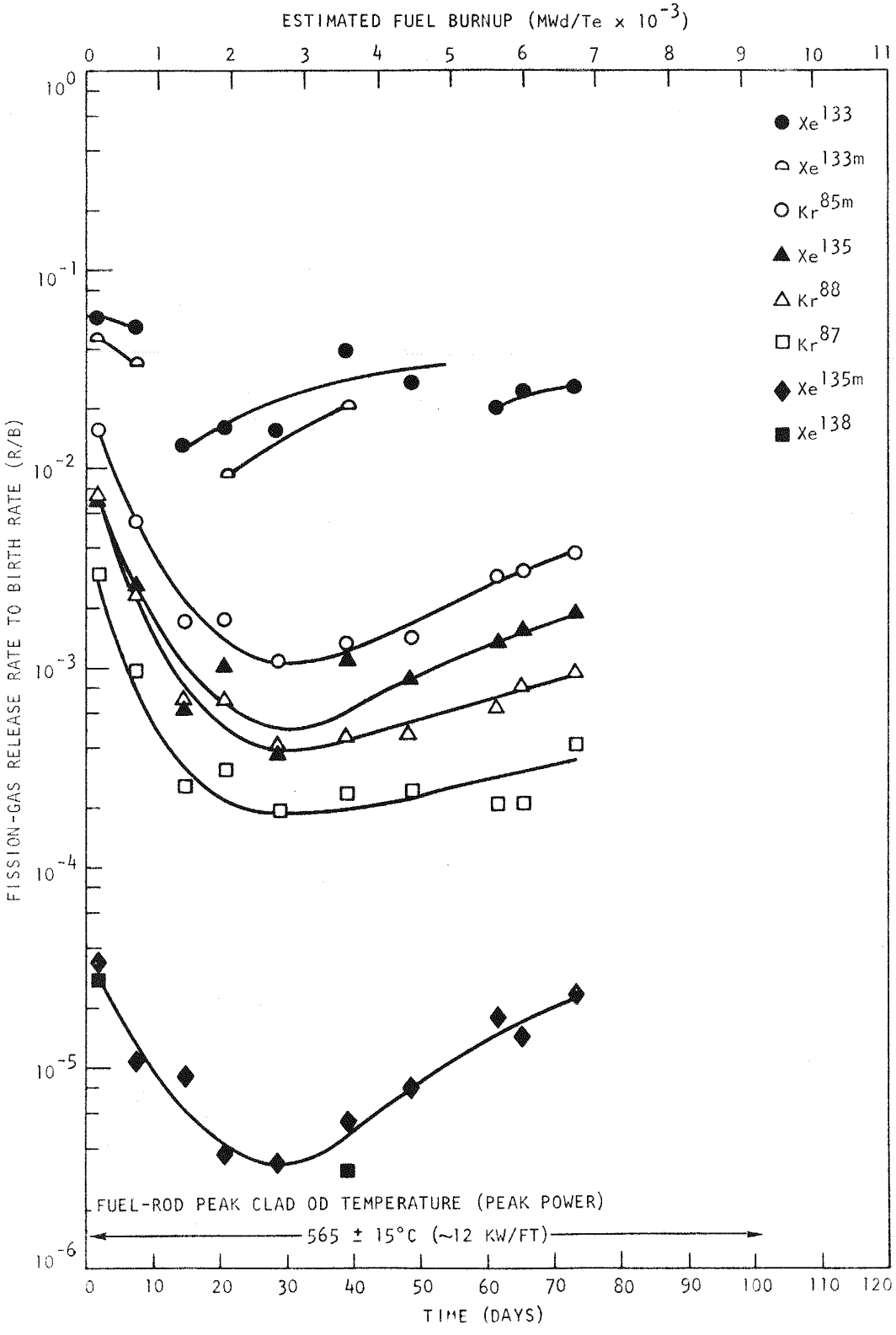

Fig. 5.3 Steady-state fission-gas release from GB-10 fuel rod vs. time for sweep flow mode TT - TT

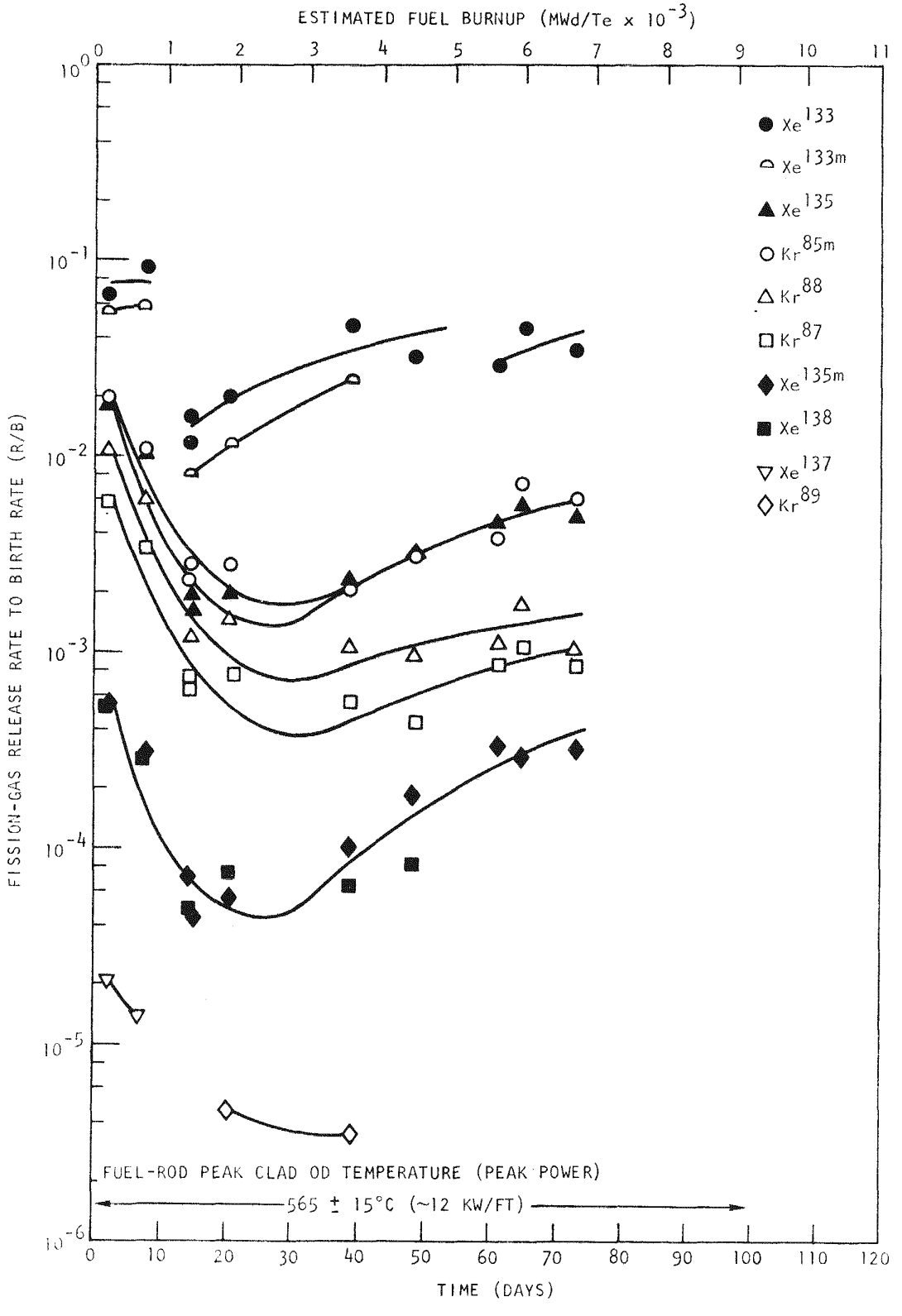

Fig. 5.4 Steady-state fission-gas release from GB-10 fuel rod vs. time for sweep flow mode TT - BT

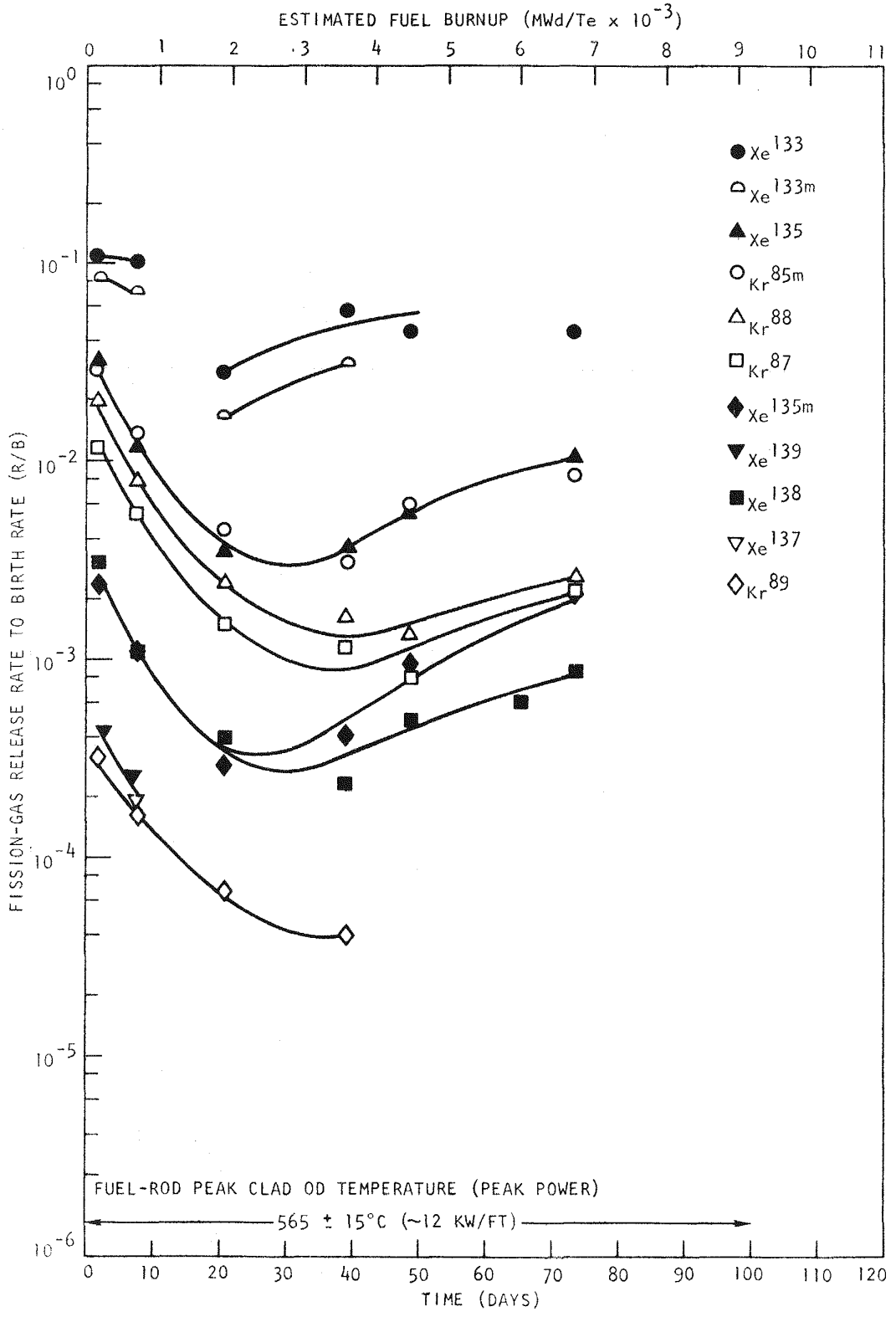

Fig. 5.5 Steady-state fission-gas release from GB-10 fuel rod vs. time for sweep flow mode TT - BB

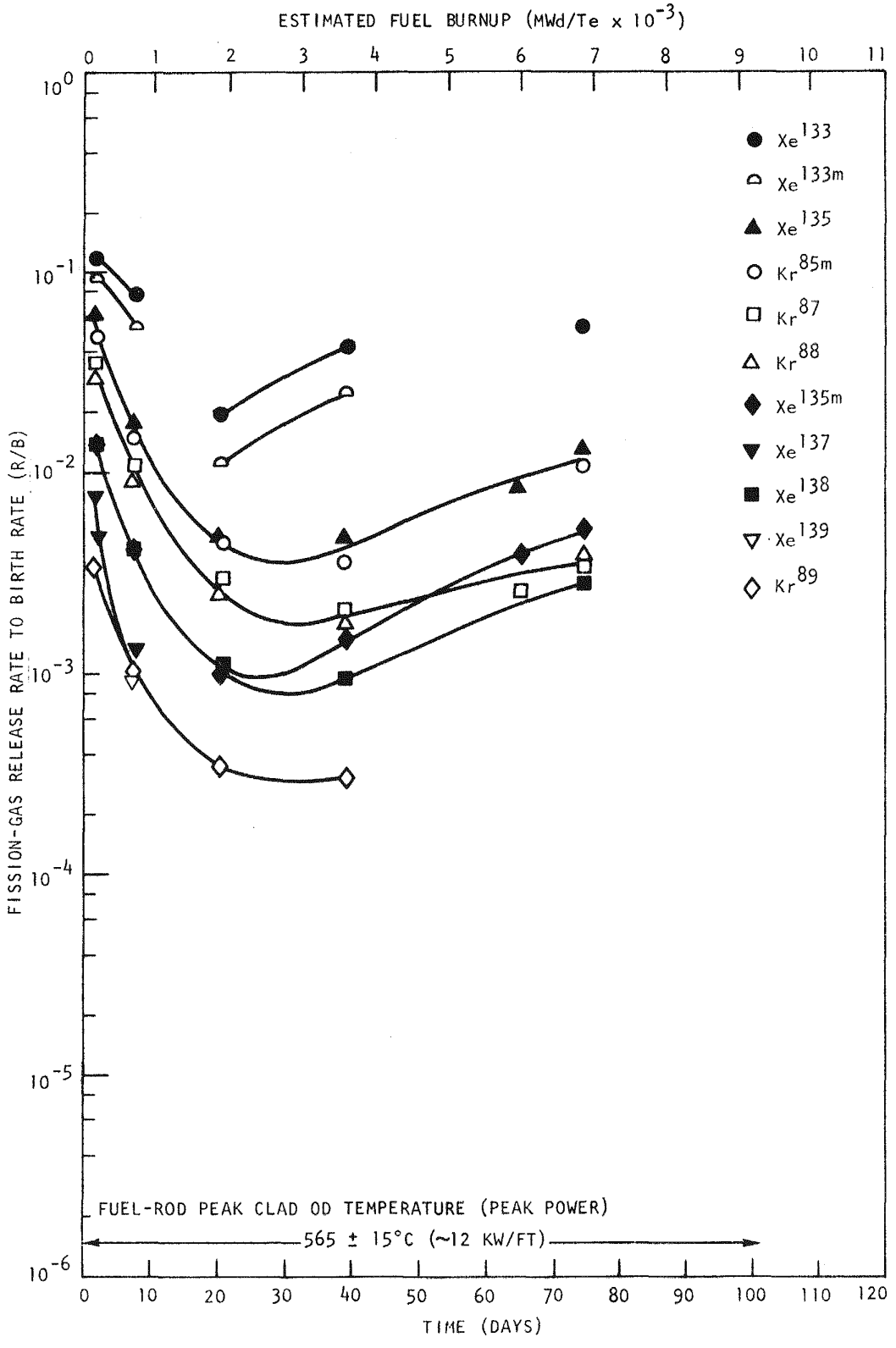

Fig. 5.6 Steady-state fission-gas release from GB-10 fuel rod vs. time for sweep flow mode BF - BB

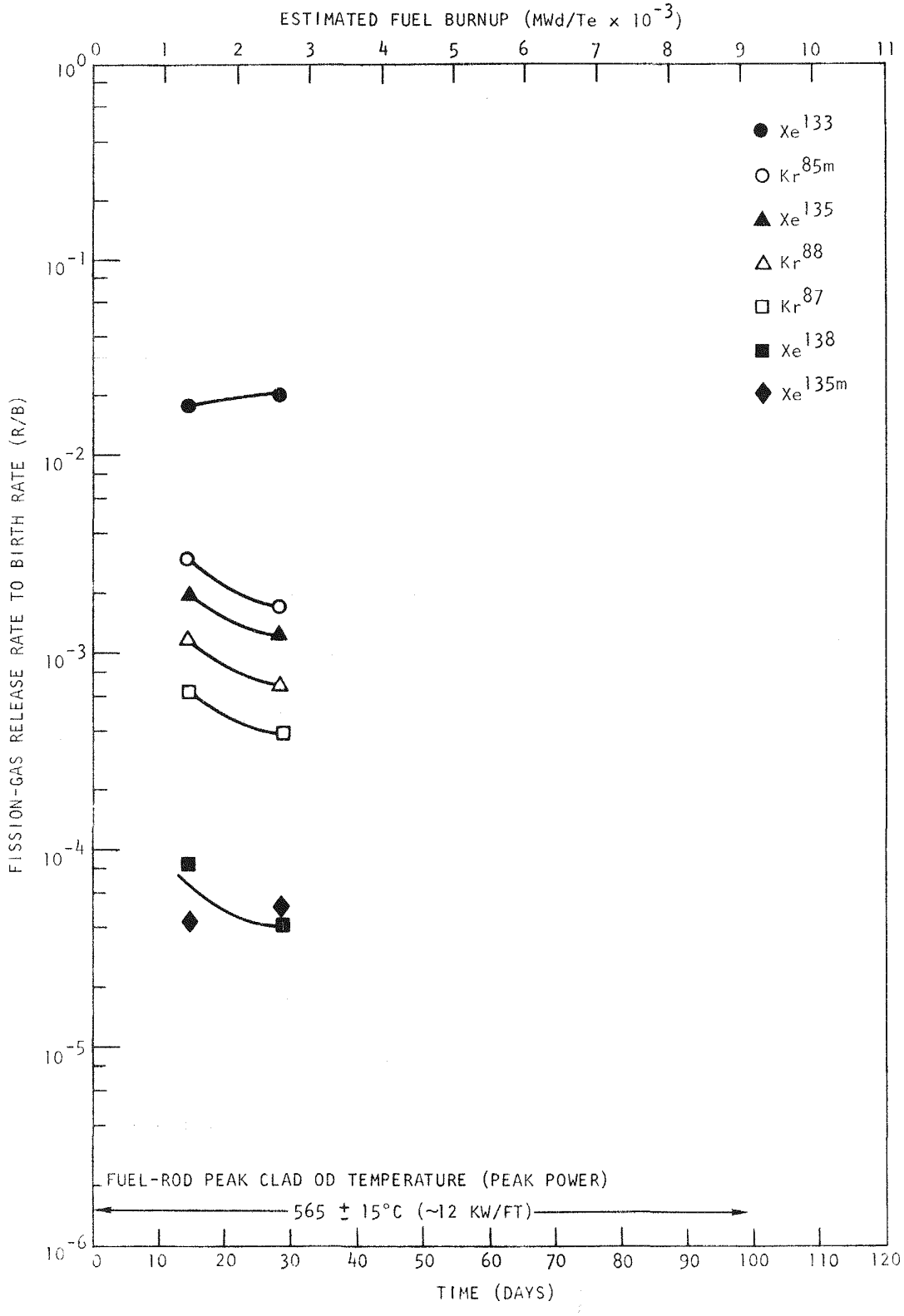

Fig. 5.7 Steady-state fission-gas release from GB-10 fuel rod vs. time for sweep flow mode BT - TT

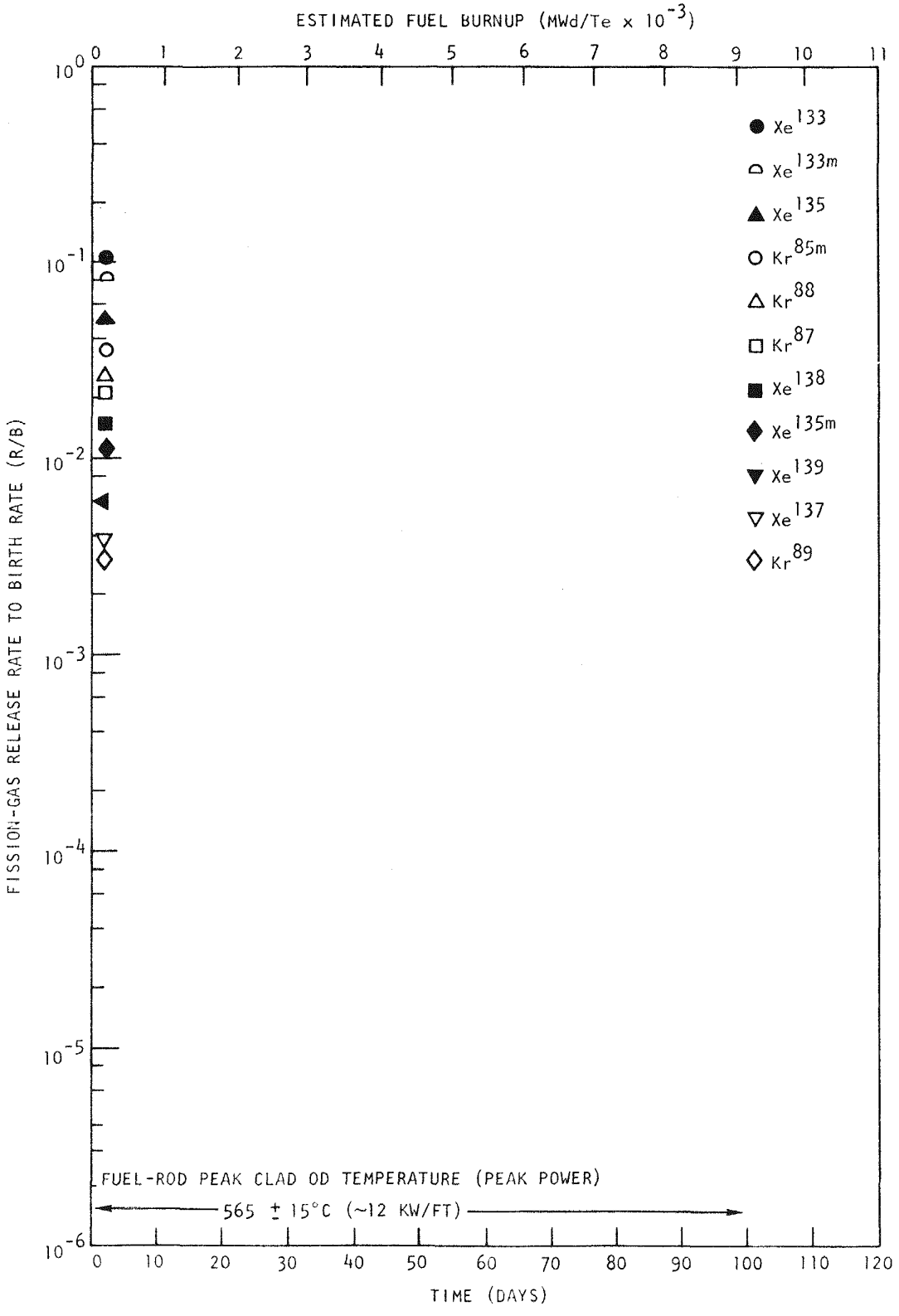

Fig. 5.8 Steady-state fission-gas release from GB-10 fuel rod vs. time for sweep flow mode BF - TT

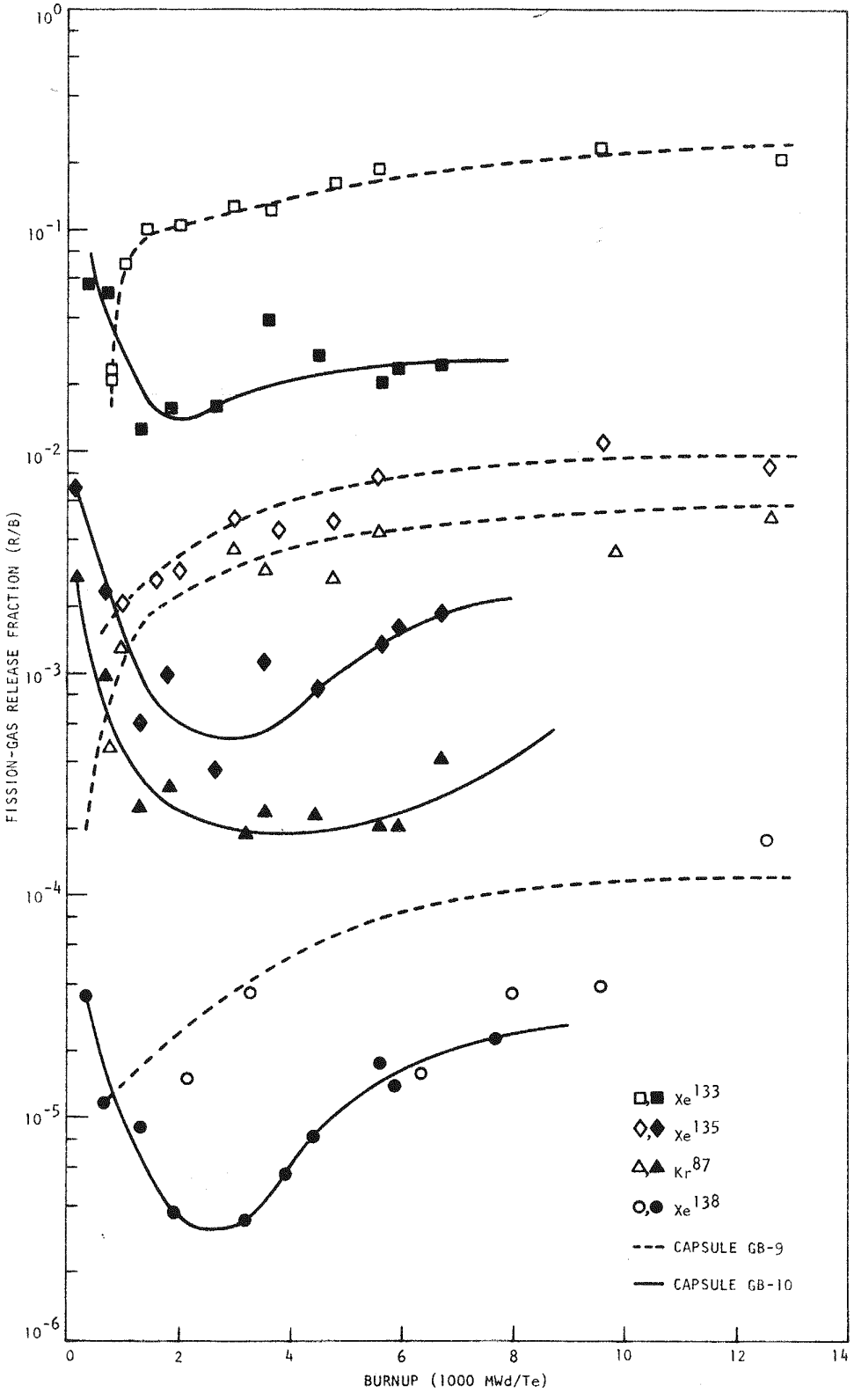

Fig. 5.9 Comparison of fission-gas release during early irradiation of fuel rods in capsules GB-9 and GB-10

The release fractions for the various isotopes in the sweep-gas flow mode in through the top of the trap and out through the top of the trap (TT - TT) in comparison with those from the flow mode in through the bottom of the fuel and out through the bottom of the blanket (BF - BB) are very different for the short-lived isotopes (e.g., Xe^{138} shows a factor of 200 greater release in the BF - BB mode), whereas the release fractions for the longer-lived isotopes (e.g., Xe^{133}) are very nearly the same for both flow modes, in agreement with expectations.

A flow constriction in the sweep-gas lines has been observed and has been located in the cross-over line between the line connecting the bottom of the blanket and the sample line to the monitor. The constriction developed while operating in the BF - BB flow mode with a flow rate of 1200 cm^3/min. It was observed that the constriction in the cross-over line disappeared after a period of time. Subsequently, it has been found that the activity in the sample line decreased with approximately a 40-min half-life while the constriction was disappearing. Radioactive half-life analysis (by ORNL) of the decay curve suggests that the deposit may be principally iodine made up of the isotopes of I^{131}, I^{133}, I^{135}, and I^{132}. Rubidium, cesium, and I^{134} also coexist in the deposit. Identification of the isotope composition of the deposit will be obtained by mounting a sodium iodide scintillation detector submerged in the pool on the sample gas line in order to take gamma-ray spectra measurements.

An analysis of the pressure drop across the capsule during the initial startup has been made. Preirradiation flow testing data taken while the capsule was connected to the various gas lines and while it was retracted from the reactor position in the pool and data taken during initial startup operation are shown in Table 5.1. It should be noted that the pressure differential across the capsule prior to irradiation was about 40 psi, whereas at zero power just prior to startup it was approximately 65 psi. It should also be noted that the differential is determined by taking the difference between two readings, each taken at about 1000 psi on strip-chart recorders with full scale readings of 1500 psi. Therefore, the individual measurements are probably no more accurate than ±15 psi and the combined reading no more accurate than ±21 psi. The measured pressure differential

Table 5.1

FLOW TESTING OF CAPSULE GB-10 PRIOR TO AND DURING INITIAL STARTUP

Clock Time	Flow Mode[a]	Flow Rate (sec/m)	Pressure (psig)			Capsule Position (in.)	Maximum Linear Heating Rate (kW/ft)	Maximum Cladding OD Temp. (°C)	Relative Rod Flow Resistance
			Upstream	Downstream	Differential				
Preirradiation Flow Testing									
1245	BF-TT	1185	1010	965	45	18.00	0	40	1.00
1320	BF-BT	1185	1010	965	45	18.00	0		1.00
1347	BF-BT	1180	1005	958	47	18.00	0		1.29
1428	BF-BB	1180	1005	958	47	18.00	0		1.29
1440	TT-TT	1235	1005	1005	0	18.00	0		----
Initial Startup									
1058	BF-TT	1027	995	930	65	11.00 to	0 to	40 to	1.67
1112		1030	997	935	62	8.6	1.5	106	1.67
1130		1033	997	937	60	8.6 to	1.5 to	106 to	1.53
1145		1035	1000	940	60	6.9	4.35	230	
1231		1035	1000	940	60	6.9 to	4.35 to	230 to	
1250		1033	1000	940	60	5.35	5.55	283	
1323		1033	1000	940	60	5.35	5.55	283	
1337		1030	1000	940	60	to	to	to	1.53
1345		1062	1000	983	17	4.05	9.0	434	0.42
1432	BF-TT	1093	1005	985	20				
1434	BF-BT	1093	1005	985	20				
1456	BF-BT	1093	1005	985	20				
1458	BF-BB	1093	1005	985	20				0.42
1519	BF-BB	1093	1005	985	20	4.05	9.0		0.48
1537	BF-TT	1087	1005	985	20	4.05 to	9.0 to	434 to	0.48
1545		1038	1005	945	60	3.25	12.0	565	1.52
1553		1062	1005	970	75			565	0.87
1559		949	1007	930	77				2.13
1622		1024	1015	980	35				0.90
1636		1046	1005	975	30				0.76
1705	BF-TT	1056	1007	977	30	3.25	12.0	5.65	0.75

[a]Flow modes are designated by two letters indicating the entrance point followed by two more letters indicating the exit point from the fuel rod. BF - bottom of fuel, TT - top of charcoal trap, BT - bottom of charcoal trap, BB - bottom of the upper blanket.

through the lines and fuel rod across the capsule prior to irradiation is very much greater than the calculated value. The pressure tap points are located upstream in the valve box and connected by 80 ft of 0.027-in.-ID tubing and downstream at the exit point of the rod, depending on the flow mode. The calculated pressure tubing loss between the upstream tap and the capsule is about 5 psi, whereas the pressure differential for flow through the fuel rod is about 2 psi in the as-fabricated condition. The reasons for the initially high preirradiation pressure differential across the capsule are not known. But it is presumed that the complex nature and structure of the fuel rod introduces very much greater uncertainty than does the lead tubing. Thus, contrary to our calculated conditions, the fuel rod is the major flow resistance in these tests.

The data indicate that as the capsule was inserted and its power increased, there was little change in the resistance in the rod to sweep-gas flow up to a power level of about 5.5 kW/ft. However, upon increasing the power from 5.5 to 9 kW/ft, the apparent flow resistance of the rod dropped by approximately a factor of 3. At the steady power level of 9 kW/ft, there was no further change in the flow resistance in the rod while flowing sweep gas in a number of different flow modes in the rod. Since all the sweep-gas flow modes involved flow over the fuel region of the rod, it appears that the major flow resistance of the rod is in the fueled region. As the power of the rod was further increased and also while operating at a steady 12 kW/ft, the flow resistance of the rod oscillated over a factor of 4 with the pressure differential (ΔP) across the capsule going as high as 77 psi. Subsequent to the initial startup operation of the capsule, the ΔP has very gradually decreased without further oscillations to a value of about 15 psi. The resistance of the flow through the rod was expected to decrease upon startup as a result of fuel cracking and possibly the formation of a central hole over much of the fuel length.

Coincident with the sudden drop in pressure differential across the capsule, there were temperature drops registered by the thermocouple monitoring the outside temperature of the cladding near the bottom of the fuel rod. The sudden temperature drops associated with the drop in the ΔP ranged from 0° to 32°C or up to about 12% of the cladding outside temperature

rise above the ambient pool-water temperature. From this evidence, it is speculated that changes in the rod flow resistance resulted from thermo-mechanical transients in the fuel rod. However, no detailed information as to the nature of these changes has been deduced. Similar, but much smaller, temperature changes have been observed during subsequent startup while flowing sweep gas through the fueled region of the fuel rod.

5.2. FAST-FLUX IRRADIATION EXPERIMENTS

5.2.1. Fast-flux Irradiation Experiment F-1 (X094A)

The irradiation of the seven encapsulated fuel rods in the F-1 (X094A) experiment in EBR-II continues toward a burnup goal of 100,000 MWd/Te. To date, a peak burnup exposure of 52,500 MWd/Te has been achieved in the lead fuel rod (capsule G-1).

The changes in fuel column length due to burnup exposure of up to 27,000 MWd/Te in the F-1 (X094) experiment are listed in Table 5.2.

The detailed as-built fuel-rod capsule drawings and the data package have been prepared for the five F-1 (X094A) replacement capsules, which are to be inserted when the F-1 (X094A) experiment is removed for interim examination at ~50,000 MWd/Te average exposure in February 1973. The replacement capsules were shipped from ORNL and have arrived at EBR-II.

Postirradiation examination of the fuel rod in capsule G-3, which was removed during the interim examination of the F-1 (X094A) experiment at an exposure of 27,000 MWd/Te, is progressing at ANL. The dosimetry tube was removed from the capsule thermal barrier. During removal the dosimeter outer tube fractured about 1/2-in. from the top end of the tube. The SiC temperature-monitor capsules are still in the thermal barrier.

In regard to the cladding strain in the G-3 fuel rod, which was previously reported to be a maximum of 0.13%, an error was made in the profilometer readings; rather than 0.3007 at the largest diameter, it should have been 0.3012 and 0.3008 at the ends of the fueled region. On measuring the unirradiated archive cladding tubing samples, ANL obtained profilometry measured diameters of 0.3003 to 0.3005. These results indicate the actual cladding diameter increase of the G-3 rod may have been as much as 0.3% rather than 0.13%.

Table 5.2

CHANGES IN FUEL COLUMN LENGTH IN F-1 (X094) EXPERIMENT

(Based on Measurements of Neutron Radiographs)

Fuel Rod No.	Smear Density (% T.D.)	Initial Fuel Length (in.)	Fuel Length at 27,000 MWd/Te (in.)	Length Change, ΔL (in.)
G-1	82.64	13.74	13.69	-0.05
G-2	84.12	13.76	13.79	+0.03
G-3	85.52	13.62	13.62	----
G-4	82.47	13.54	13.54	----
G-5	83.51	13.69	13.69	----
G-6	82.65	13.53	13.53	----
G-7	82.54	13.58	13.49	-0.09
G-8 (std)	86.06	13.59	13.59	----

Analysis of the gamma spectrometry data from the interim examination of capsule G-3 from the F-1 (X094) irradiation assembly at 27,000 MWd/Te burnup continued during the quarter. The principal effort was an analysis of the diametral Mn^{54} activity due to activation of the stainless steel. The experimental data were reported previously in the quarterly report for the period February 1, 1972 through April 30, 1972.[2] The experimental data were normalized to a relative activity minimum and are replotted in linear form in Fig. 5.10.* A comparison of the diameters of the peaks in Mn^{54} activity obtained from Fig. 5.10 with the calculated peaks obtained from Figs. 5.11 and 5.12 is given in Table 5.3. The agreement is shown to be within ± 0.01 in. except for the diameter of the thermal barrier in the blanket region.

The expected activity profiles due to Mn^{54} activation in the three concentric steel tubes has been calculated. The expected profile is a composite of the contributions of the three tubes for each 180° sector as shown in Fig. 5.13. The composite calculated profiles are then shown

*These data are taken from the diametral gamma scan in the blanket region. Similar data were obtained in the fuel region and will be reported later.

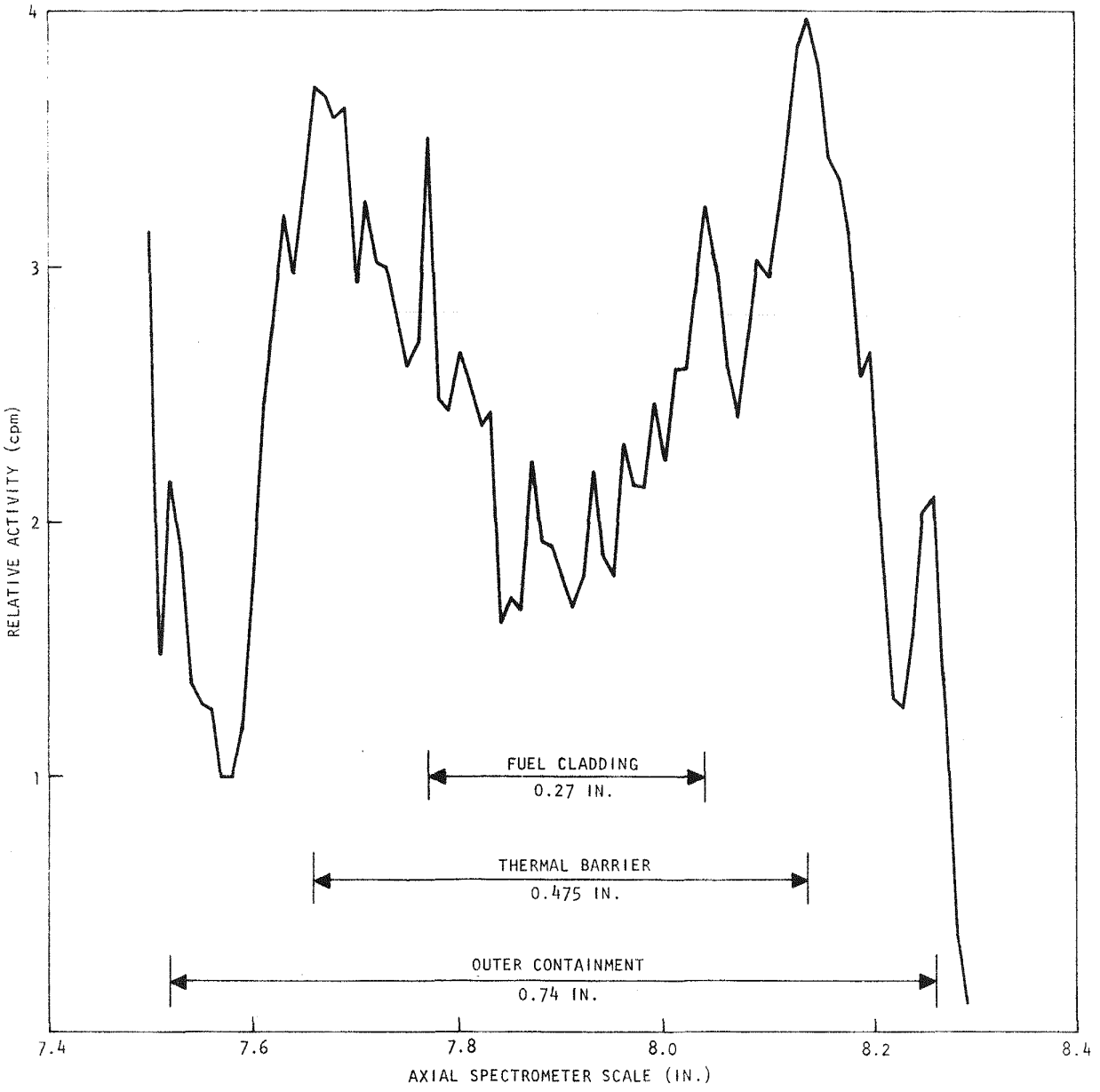

Fig. 5.10 Calculated relative diametral activity profile in linear form for the three concentric tubes of F-1 (X094) capsule G-3

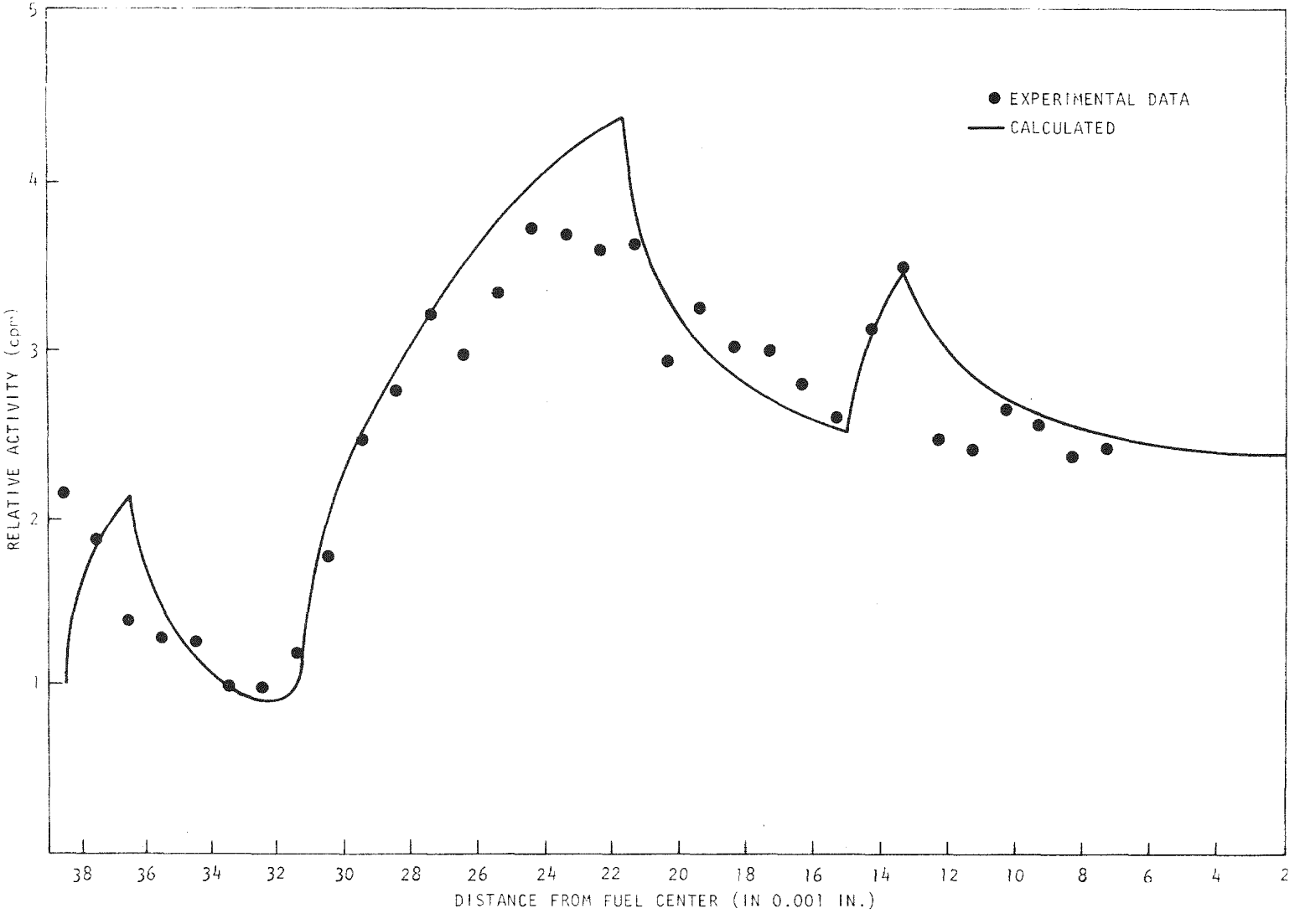

Fig. 5.11 Calculated Mn^{54} distribution in composite of three steel tubes surrounding fuel in F-1 (X094) capsule G-3—0° to 180° sector

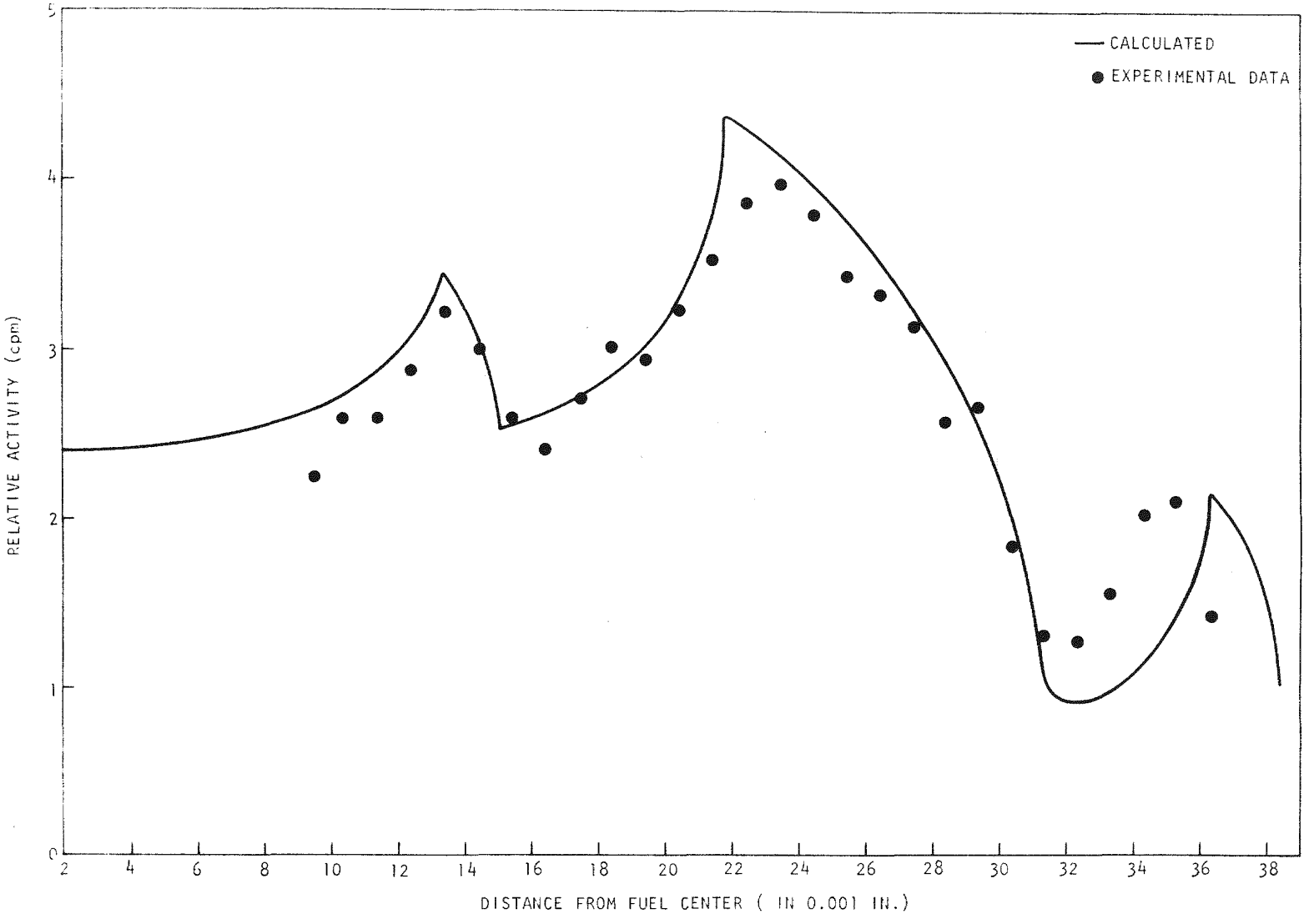

Fig. 5.12 Calculated Mn^{54} distribution in composite of three steel tubes surrounding fuel in F-1 (X094) capsule G-3—180° to 360° sector

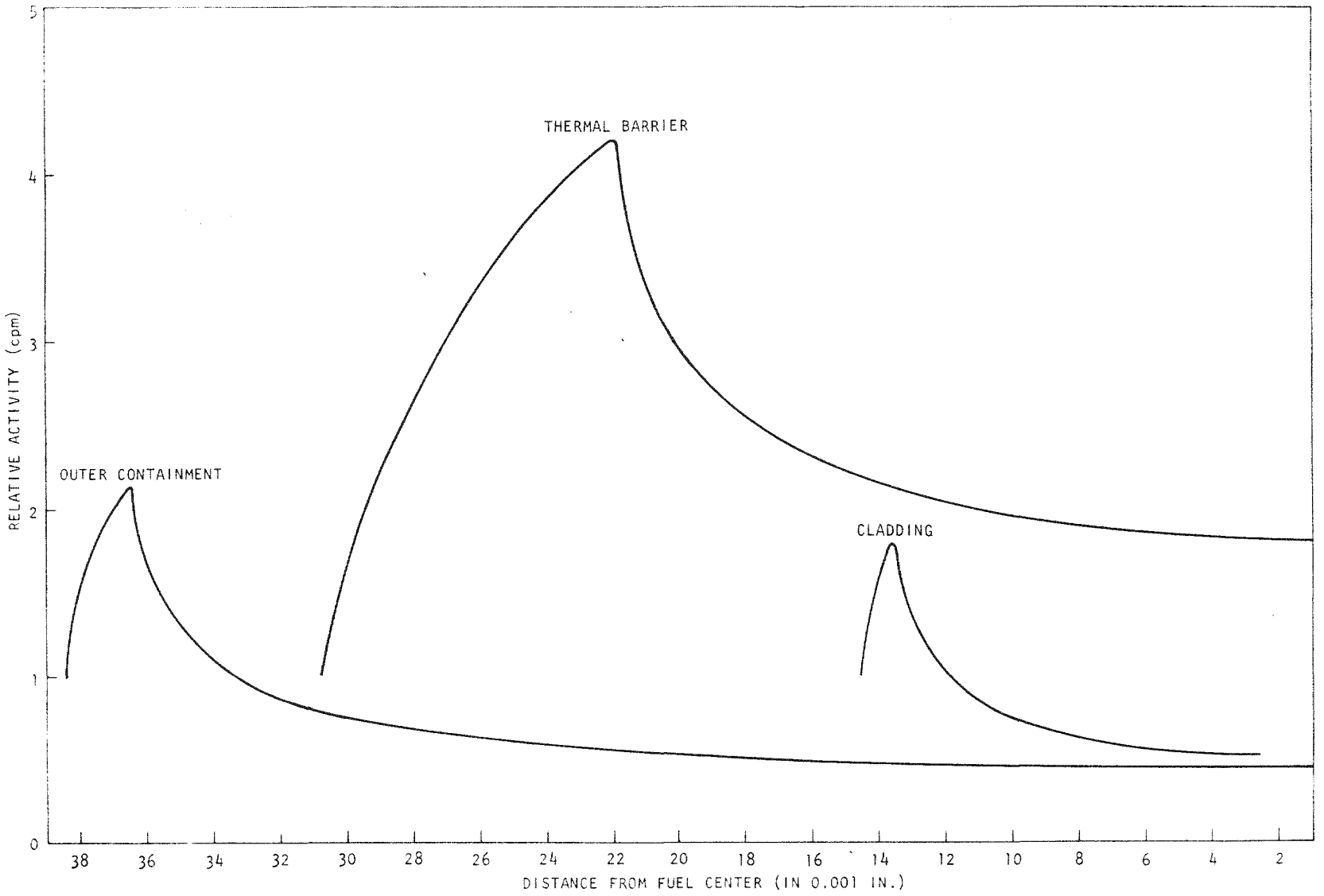

Fig. 5.13 Calculated Mn^{54} distribution in each of the concentric steel tubes surrounding the F-1 (X094) fuel rod G-3

Table 5.3

DIAMETERS OF MAXIMUM RELATIVE Mn^{54} ACTIVITIES IN CAPSULE G-3

Axial Region	Outer Containment (in.)	Thermal Barrier (in.)	Cladding (in.)
Mid-fuel region	0.73	0.455	0.27
Blanket region	0.74	0.48	0.27
Calculated	0.728	0.44	0.268

as the solid lines in Figs. 5.11 and 5.12,* where they are compared with the normalized experimental data points.

The axial flux profile remains to be determined from the Mn^{54} activity data to obtain the relative flux profile for the capsule irradiation. Data are available for rods G-1, G-3 and G-4 over the entire length of the fuel and blanket regions.

Tellurium is a volatile fission product and might be expected to migrate in the fuel rod as have other volatile species.(3) Therefore, the detailed axial gamma scan for capsule G-3 has been reexamined to determine the Te^{132} profile. The data are shown in Fig. 5.14 for the lower fuel-blanket interface. The Te^{132} activity profile coincides precisely with that of I^{131} with peaks at the fuel-blanket interface and at the gap between the first and second fuel pellets. Thus it can be concluded that tellurium, like iodine, is a volatile migrating species. Based on data available to date it is possible, although unlikely, that the observed migration of I^{131} might be entirely accounted for by migration of the tellurium precursors Te^{131m} or Te^{131y}. However, it is suspected that both the iodine and the tellurium are involved in vapor transport processes.

5.2.2. Fast-flux Irradiation Experiment F-3

Planning continued for the F-3 irradiation experiment and some changes in the details of the loadings of the capsules were made. These are shown in Table 5.4.

Some changes in the details of the dosimetry and in the design of the capsule upper end plugs were also made. The change in dosimetry involved

*The scale of the calculated curve and the experimental points were made coincident at the well-defined peak resulting from the fuel cladding.

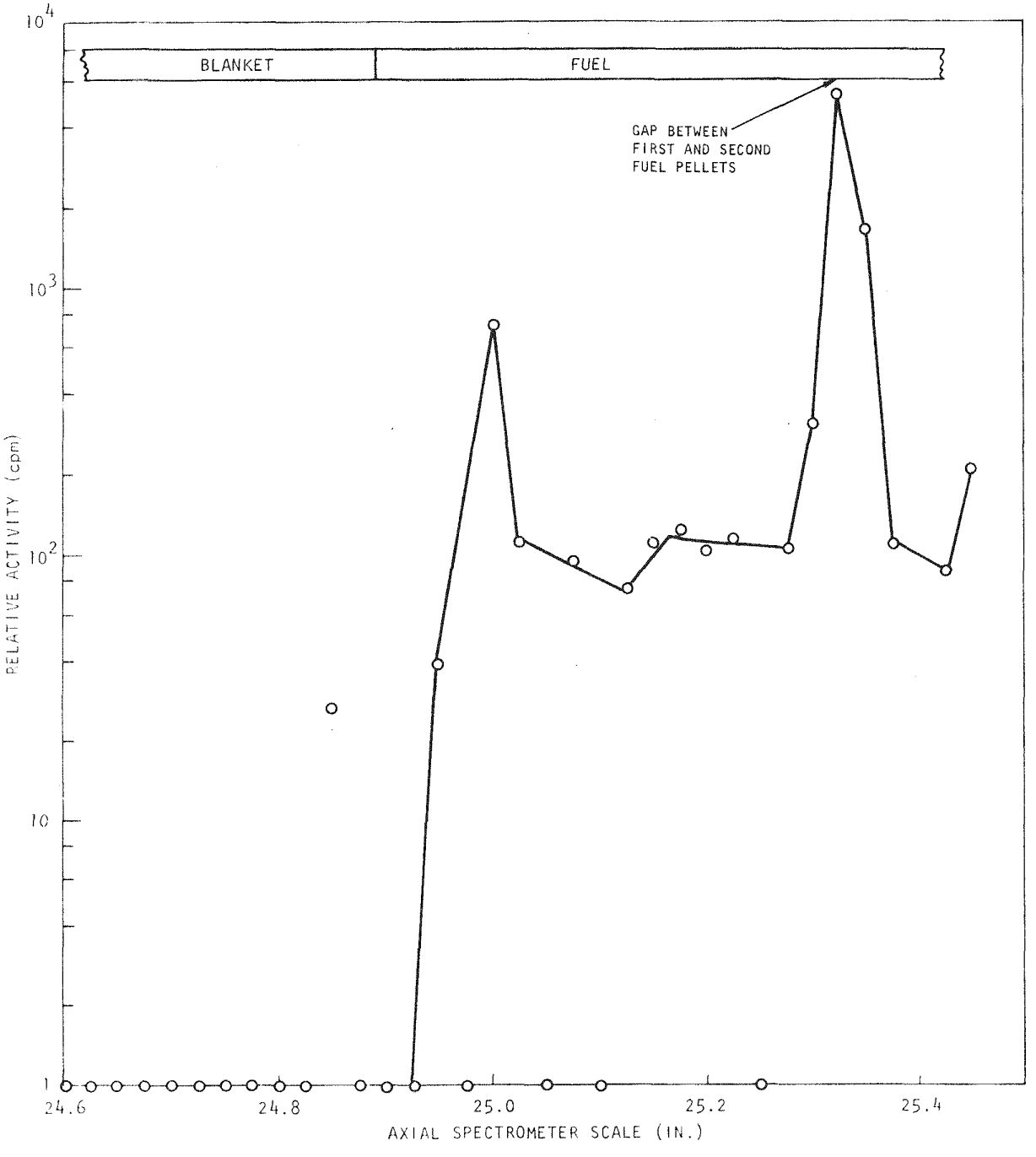

Fig. 5.14 Detailed gamma scan of Te^{132} at lower fuel-blanket interface, capsule G-3, F-1 (X094) irradiation, 2 x 10^{22} nvt

Table 5.4

F-3 FAST-FLUX IRRADIATION CAPSULE EXPERIMENT

Fuel-rod Capsule No.	Cladding Temperature Calculated (°C)	F-3 Irradiation Conditions								Remarks
		Fuel O/M Ratio	Fuel Density (% TD)	Pellet Geometry	Burnup (MWd/Te)		Charcoal Trap			
					50,000	100,000	Type	Location[a] (in.)	Neutron Fluence ($nvtx10^{-22}$)	
G-14	676	1.94	88	Solid	—		A	9.875	2.4	Initial loading into subassembly
G-15	685	1.94	88	Solid	—	—	A	7.55	7.0	
G-16	688	1.94	88	Solid	—	—	S	7.55	7.0	Transient test rod
G-17	690	1.98	88	Solid	—	—	A	7.55	7.0	Transient test rod
G-18	689	1.98	88	Solid	—	—	S	9.875	4.7	
G-19	749	1.94	92	Annular	—		A	9.875	2.4	
G-20	749	1.98	92	Annular	—		A	9.875	2.4	
G-21	728	1.94	92	Annular	—	—	A	9.875	4.7	
G-22	743	1.94	88	Solid	—	—	A	7.55	7.0	
G-23	743	1.98	88	Solid	—	—	A	9.875	4.7	
G-24[c]	676	1.94	88	Solid		—	A	7.27	3.7	Charcoal trap between blanket pellets 1 and 2
G-25[c]	749	1.94	88	Solid		—	A	7.55	3.5	
G-26[c]	749	1.94	88	Solid		—	S	9.875	2.4	

Notes:

All capsules to be gamma-scanned and neutron-radiographed at 50,000 MWd/Te and 75,000 MWd/Te.

All rods will have a 10-in. fuel column length and will be designed to operate at a nominal maximum heat generation rating of 15 kW/ft, but because of the expected power tilt in the subassembly, this will be the maximum in the maximum-powered rod.

All rods will contain $U_{0.8}Pu_{0.2-x}$ fuel (x = 0.02 or 0.06). At 100,000 MWd/Te burnup, the fluence will be ~1.3×10^{23} n/cm^2.

All rods will have roughened cladding. The smear density will be 80% to 85% on all rods.

[a] Distance from core centerline to trap centerline.

[b] A = active; S = sealed.

[c] Replacements to be installed at 50,000 MWd/Te exposure.

compartmentalizing the coated particles to facilitate easier handling and identification during postirradiation examination. The design of the capsule end plug was also changed to facilitate handling by the EBR-II Project. Information from ANL on the amount of flow bypass through the ANL Group-08 capsules (which will share the J19A subassembly) is not as yet available. Additional thermal analysis for the F-3 experiment will be performed employing the HECTIC code to evaluate the effects of the ANL flow-through capsules.

Some of the machined hardware for the F-3 experiment has been received from the vendor supplier and assembly has been initiated. The fabrication of the UO_2 blanket pellets for the F-3 fuel rods has been completed.

Design drawings have been sent out for obtaining bids for machining the required hardware. Copies of the design drawings have also been submitted to the ANL Plutonium Fuels Fabrication Section and to the EBR-II Project.

REFERENCES

1. "Gas-Cooled Fast Breeder Reactor Quarterly Progress Report for the Period August 1, 1972 through October 31, 1972," USAEC, Report GA-A12421, Gulf General Atomic, December 8, 1972.

2. "Gas-Cooled Fast Breeder Reactor Quarterly Progress Report for the Period February 1, 1972 through April 30, 1972," USAEC, Report GA-A-12165, Gulf General Atomic, July 20, 1972.

3. Langer, S., et al., "Volatile Fission-product Migration and Plateout in GCFR Fuel-rod Irradiations," Trans. Am. Nucl. Soc., Vol. 15, No. 2, November 1972, p. 850.

6. TASK 4700—NUCLEAR ANALYSIS AND REACTOR PHYSICS

Efforts continued on surveillance of LMFBR critical assembly experiments with the objective of establishing an experimentally verified basis for GCFR reactor physics work. Analysis of ZPPR-2 voided inner core experiments had to be curtailed because of an imposed budget cut for Task 4700. Emphasis during the quarter focused on comparisons between GGA and ANL physics calculations of a 300-MW(e) GCFR. Work has begun on the definition of goals and requirements of a GCFR critical experiments program. Liaison with ANL continued, both through the Industrial Participation Program and through direct contact with members of the ANL staff.

6.1. CRITICAL ASSEMBLY ANALYSIS

6.1.1. Small-sample Central Worth

Work continued on the analysis of the small-sample central worth in the voided inner core of ZPPR-2.[1] A two-dimensional DOT calculation of the flux depression in the B1 sample was repeated using a finer spatial mesh. Applying the calculated flux depression factor to the r-z perturbation calculation improved the calculation-to-experiment ratio (C/E) from 1.35 to 1.19.

6.1.2. Doppler Small-sample Worths

The calculation of the Doppler small-sample worth in the 69-drawer voided inner core of ZPPR-2 was reanalyzed to check the assumptions used in the calculations—namely,

1. Sample and capsule self-shielding is adequately handled with diffusion theory. This appears to be true for the hardened voided inner core where self-shielding is small (less than 2% in all groups).

2. Changes in self-shielding with temperature is negligible. This appears to be true because the self-shielding is negligible; also, the maximum sample cross-section variation with temperature was 15%.

3. The Doppler effect of the Inconel capsule can be ignored. Actually, this could account for approximately 5% of the total Doppler worth and should be included.[2] Calculation of this effect is being postponed until calculations with ENDF/B Version III are completed.

4. ENDF/B Version II (modified) cross sections are adequate. Calculations with ENDF/B Version III might decrease the Doppler worth by a few percent primarily due to changes in the sodium and iron cross sections.

It is therefore expected that the GGA calculation-to-experiment ratio of C/E = 1.07 is within the range of experimental and calculational uncertainties and that inclusion of items 3 and 4, above, will have a small net effect.

6.2. ANL LIAISON

Meetings were held on November 2, 1972, at ANL with members of the Applied Physics Division to discuss the GCFR program. It was agreed that GGA would prepare a hierarchy of GCFR physics parameters that require experimental verification and ANL would then make recommendations as to feasibility and costs for these experiments.

6.3. GCFR CROSS SECTIONS

Conversion of the GGA data files for GCFR to ENDF/B Version III was completed during the last quarter. Generation of multigroup cross sections is now under way. This effort, however, has had to be curtailed because of the imposed budget cut on the physics tasks.

6.4. GCFR CRITICAL ASSEMBLY PLANNING

Work is continuing in defining physics design problems affecting the design of the 300-MW(e) GCFR. The major physics design problems that have

an impact on reactor performance and economics can be categorized as follows:

1. Calculation of statics parameters such as critical mass, power distribution, control-rod worth, and reactivity coefficients.
2. Calculation of slowly varying quantities such as burnup-associated changes and control-rod programs.
3. Calculation of reactor transients.

Although the physics design of a GCFR can rely heavily on methods and data developed in other programs, in particular the LMFBR program, in each of the above areas there is some inadequacy in the calculational method or relevant data. Uncertainty in statics parameters is being reduced by the analysis of appropriate critical assembly mockups being utilized by the LMFBR program with emphasis on those experiments involving sodium-voided regions. A full GCFR critical experiment program is being planned to reduce these uncertainties to acceptable values.

6.5. UNCERTAINTY ANALYSIS

6.5.1. GGA and ANL Benchmark Calculations

As part of a cooperative study between ANL and GGA to assess the adequacy of design methods currently in use at GGA for fast reactor analysis, a series of calculations of standard benchmark-type fast assemblies was performed at ANL utilizing the recently developed space-dependent cross-section averaging code SDX[3] and microscopic cross-section input from ENDF/B Version III data tapes. Four assemblies were selected for study. Three of those chosen were the well-known standard ZPR-6 Assembly 6A, a uranium-fueled assembly; the plutonium-fueled ZPR-6 Assembly 7; and the plutonium-uranium-carbide-fueled ZPR-3 Assembly 48. Results of this study at ANL have been recently reported.[4] The fourth assembly chosen for study was a representation of a 300-MW(e) GCFR. Details of this work, and auxiliary calculations, are reported here.

6.5.1.1. Calculational Model. A quarter of the core of a two-dimensional model is shown in Fig. 6.1. The number of mesh points selected for later r-z calculations are in parentheses. It was decided that the initial

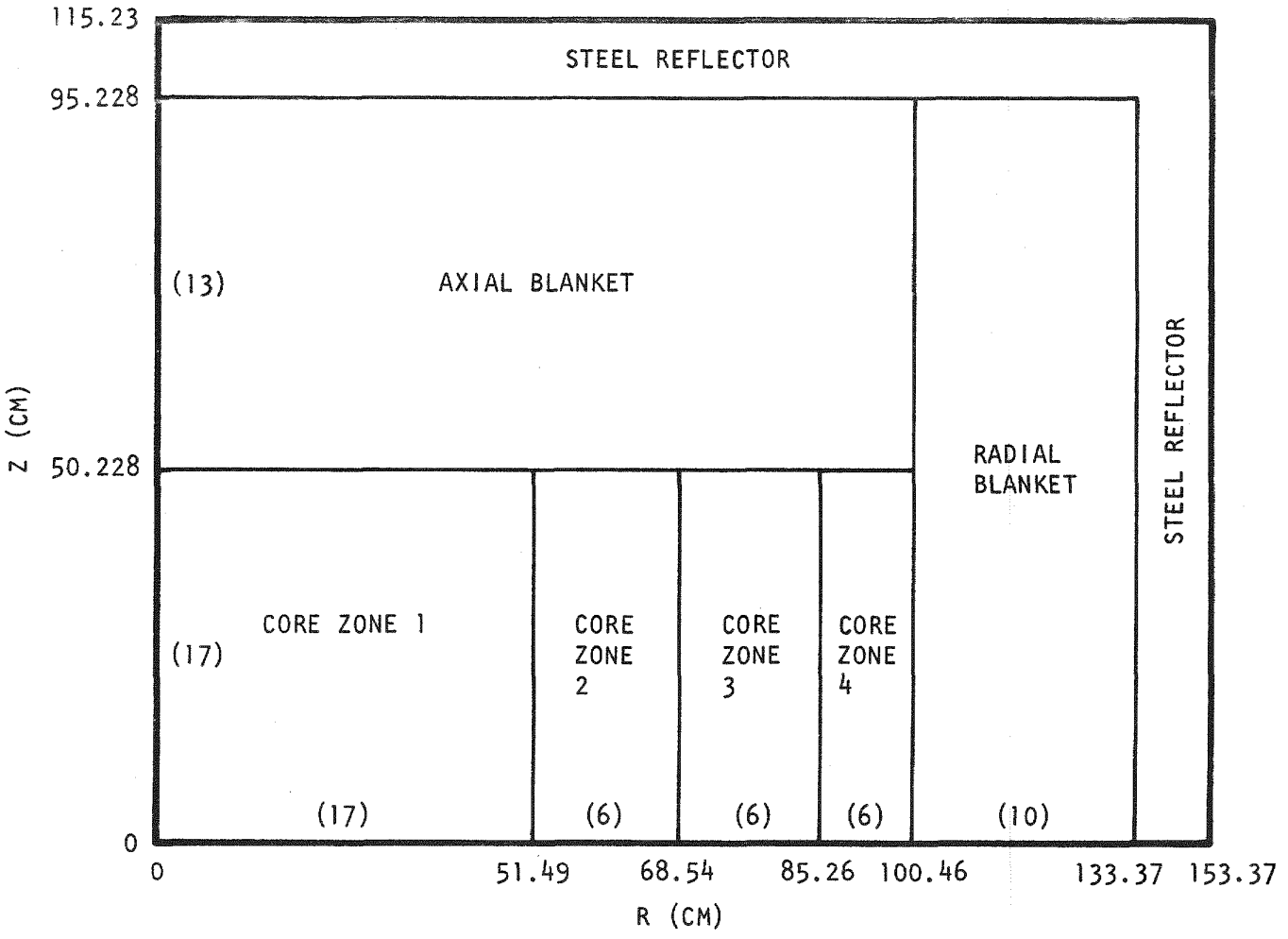

Fig. 6.1 Cylindrical dimensions (one-fourth core) for a 300-MW(e) GCFR

calculations would be performed on a hot, clean, unrodded core. Accordingly, the atom densities selected were those of a virgin core prior to burnup to the equilibrium cycle[5] and reflect the compositions appropriate to fueling with LWR discharge-grade plutonium fuel. A temperature of 1300°K was chosen for the mean core and axial blanket temperature and a temperature of 850°K was deemed appropriate for the radial blanket. No control poisons or fission-product simulation were included so that any uncertainties due to rod self-shielding or fission-product compositions are eliminated.

6.5.1.2. Cross-section Generation and Spectrum Calculation. The unit-cell models chosen for the core and the blanket structures were those reported earlier.[6] The effect of cell heterogeneity was included in calculations of the resonance self-shielding of the heavy metals but was not included in spatial self-shielding effects (the "resonance heterogeneity" treatment). The one-dimensional SDX code was then utilized to produce cross sections for a 156-group energy mesh of 0.1 lethargy unit width, starting from the ANL maximum energy considered of 10.0 MeV (lethargy = 0.0). This code utilizes as input data a set of 156-group cross sections generated using ENDF/B Version III data in a consistent B_1 calculation of the core of ZPPR Assembly 2 with the MC^2 code. These data files are incorporated into the Argonne Reactor Computation (ARC) system.[7] The SDX code computes the 156-group spectrum at each space point specified. For the present calculation, the 45-point radial mesh structure of Fig. 6.1 was utilized. In each radial zone, a space point representing the midpoint of the region was selected and the median energy from the 156-group edit was ascertained. This is exhibited in Table 6.1, where the 156-group structure has been manually collapsed to correspond exactly with the GGA 10-group structure commonly used.

Also of interest is the integrated flux below a given energy which is obtained from the same edit. Figure 6.2 illustrates this representation for each of the radial zones. The curves for core zones 2, 3, and 4 are all approximately the same and are represented by a single curve.

The midpoint spectra are shown in Fig. 6.3 for core zones 1 and 2 (CZ 1, CZ 2) and the radial blanket (RB). Each curve has been normalized so that $\int \phi(u)\, du = 1.00$.

Table 6.1

REGIONWISE INTEGRATED FLUXES

GGA Group No.	GGA E_{Lower} (ev)	u_{Lower}	$\bar{u}$	$E(\bar{u})$ (ev)	Region Midpoint Fractional Integrated Flux Below Group				
					Core Zone 1	Core Zone 2	Core Zone 3	Core Zone 4	Radial Blanket
--	10×10^6	0	---	------	1.0000	1.0000	1.0000	1.0000	1.0000
1	3.679×10^6	1.0	0.5	6.065×10^6	0.9832	0.9809	0.9792	0.9792	0.9936
2	1.353×10^6	2.0	1.5	2.231×10^6	0.9082	0.8961	0.8878	0.8893	0.9618
3	479.9×10^3	3.0	2.5	820.8×10^3	0.7346	0.7079	0.6929	0.7005	0.8512
4	183.2×10^3	4.0	3.5	302.0×10^3	0.5123	0.4789	0.4632	0.2611	0.4252
5	67.38×10^3	5.0	4.5	111.1×10^3	0.2882	0.2596	0.2482	0.2611	0.4252
6	24.79×10^3	6.0	5.5	40.9×10^3	0.1438	0.1252	0.1185	0.1268	0.2347
7	9.119×10^3	7.0	6.5	15.03×10^3	0.0557	0.0467	0.0434	0.0474	0.1066
8	3.355×10^3	8.0	7.5	5.53×10^3	0.0204	0.0164	0.0149	0.0166	0.0465
9	0.454×10^3	10.0	9.0	1.234×10^3	0.0005	0.0003	0.0003	0.0004	0.0046
10	0.414	17.0	13.5	13.7	0.0	0.0	0.0	0.0	0.0
11	0.0	----	----	------	------	------	------	------	------
Median lethargy, $\bar{u}$					4.047	3.912	3.849	3.900	4.285
$E(\bar{u})$, kev					174.8	200.0	213.0	202.4	137.7

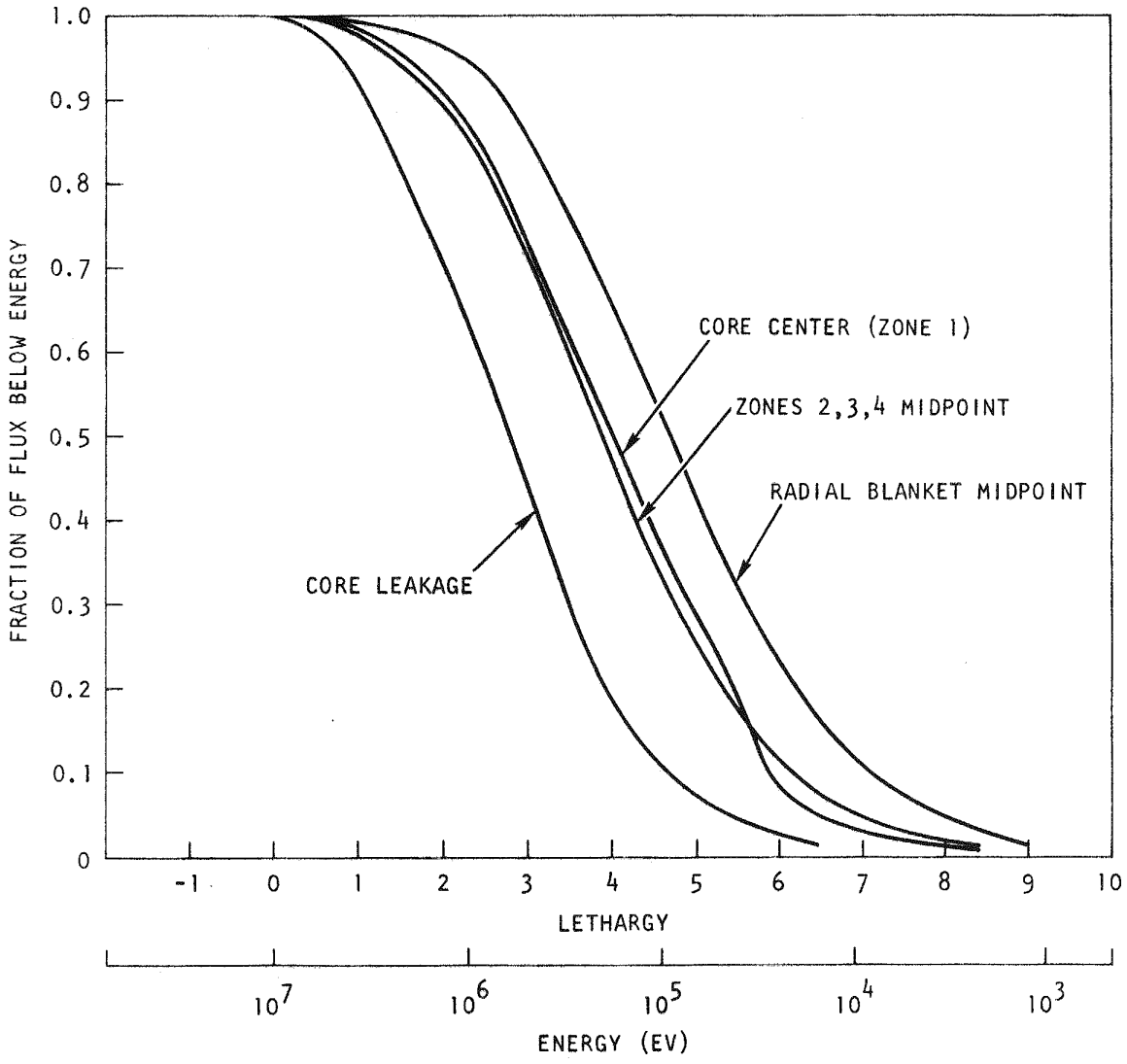

Fig. 6.2 ANL calculated integrated fluxes for a 300-MW(e) GCFR

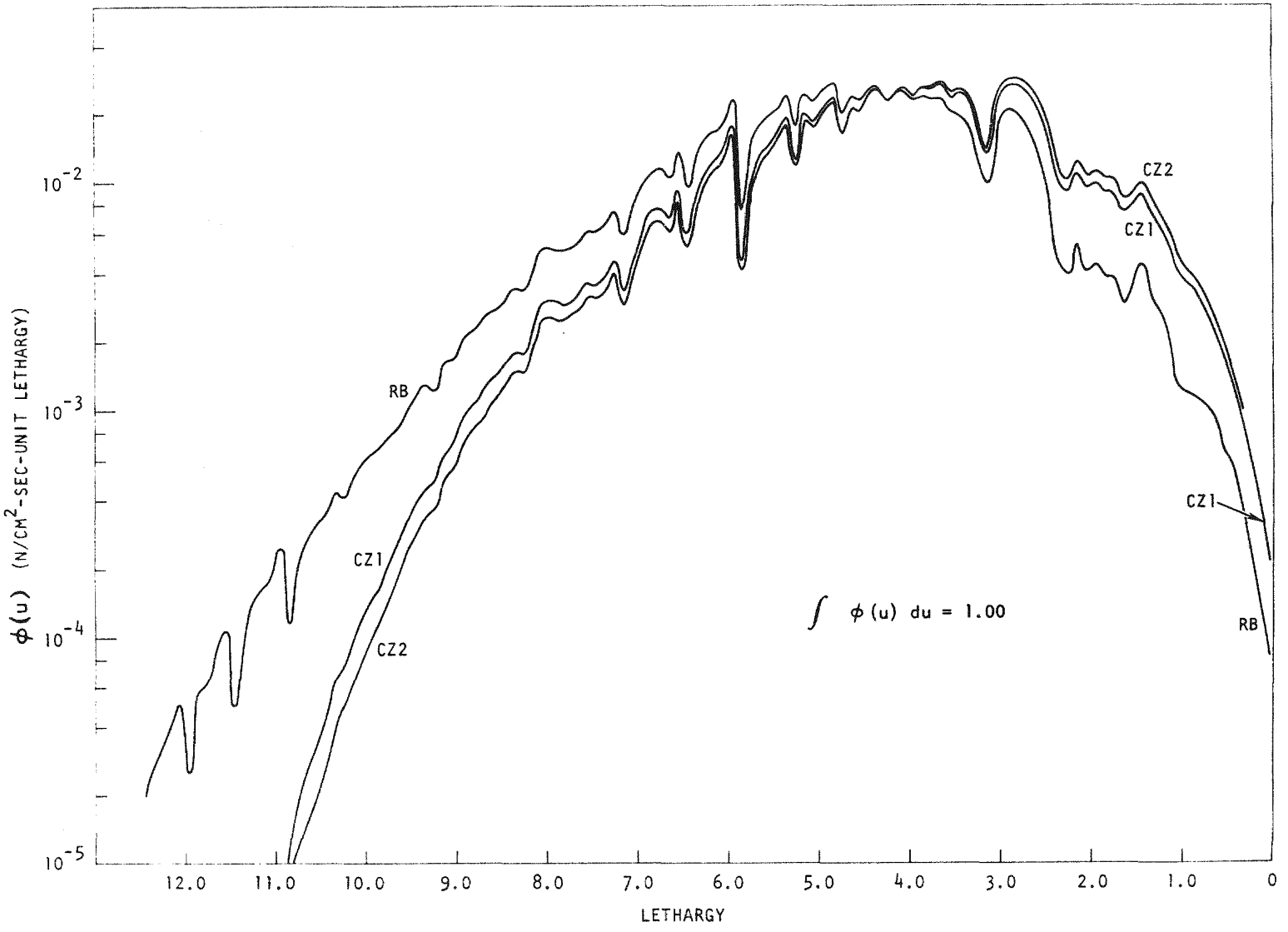

Fig. 6.3 Midpoint spectra in a 300-MW(e) GCFR

Cross-section preparation for the four separate subregions of the axial blanket used an appropriately weighted average of the atom densities in each region in a fundamental mode calculation. This option is available as a single region calculation in the SDX code.

The collapsing regions for producing the space-dependent cross-section sets may be varied so that within any individual region (e.g., core zone 2), subregions may be specified, each having its own set of cross sections for inclusion in later diffusion calculations. Preliminary tests of this option, however, indicate that for very large, dilute systems such as the present core, a single collapsing region per core zone is adequate. Hence the number of cross-sections sets generated were limited to the six necessary to specify four core zones and two blanket zones.

Group-collapsing from the base 156-group structure to the standard ANL 27-group mesh and an 11-group mesh was then done. An example of the group structure and the edits for core zone 1 for selected heavy metal cross-sections are given in Table 6.2.

6.5.1.3. Two-dimensional Diffusion Theory Calculations. Two-dimensional diffusion calculations utilizing the above six sets of cross sections were performed on the model shown in Fig. 6.1. Except where noted, these computations were made with the 11-group energy mesh. No streaming corrections have been included.

Calculated power maps are shown in Figs. 6.4 and 6.5. The breakdown of power generated in each zone is shown in Table 6.3. It is apparent that while the maximum powers generated in each power-producing region are quite close, which is desirable, some additional zone power tailoring may be possible.

Two-dimensional perturbation calculations using real and adjoint fluxes for the unreflected reactor were performed to get preliminary estimates of some of the kinetic parameters and reactivity worths. Table 6.4 shows the quantities computed.

In the calculation of the effective delayed neutron fraction, the higher isotopes of plutonium, Pu^{241} and Pu^{242}, were lumped with Pu^{240} for lack of a better representation.

Table 6.2

ENDF/B VERSION III CROSS SECTIONS FOR GCFR CORE ZONE 1

ANL 11-Gp	GGA 10-Gp	ANL 27-Gp	E_{Lower} (ev)	u_{Lower}	Pu-239 $\sigma_{capture}$[a]	Pu-239 $\sigma_{fission}$	Pu-239 $\nu\sigma_{fission}$	$\alpha = \frac{\sigma_{cap.}}{\sigma_{fiss.}}$	U-238 $\sigma_{capture}$
			10.000×10^{6}	0.0					
1	1	1	6.065×10^{6}	0.5	1.582×10^{-3}	2.082	8.269	7.598×10^{-4}	6.412×10^{-3}
		2	3.679×10^{6}	1.0	1.758×10^{-3}	1.708	6.038	1.030×10^{-3}	1.175×10^{-2}
2	2	3	2.231×10^{6}	1.5	4.147×10^{-3}	1.962	6.391	2.114×10^{-3}	2.851×10^{-2}
		4	1.353×10^{6}	2.0	1.057×10^{-2}	2.001	6.220	5.283×10^{-3}	6.514×10^{-2}
3	3	5	8.208×10^{5}	2.5	2.553×10^{-2}	1.748	5.269	1.461×10^{-2}	1.219×10^{-2}
		6	4.979×10^{5}	3.0	7.769×10^{-2}	1.627	4.816	4.776×10^{-2}	1.253×10^{-1}
4	4	7	3.020×10^{5}	3.5	1.429×10^{-1}	1.553	4.547	9.201×10^{-2}	1.171×10^{-1}
		8	1.832×10^{5}	4.0	1.959×10^{-1}	1.493	4.345	1.312×10^{-1}	1.343×10^{-1}
5	5	9	1.111×10^{5}	4.5	2.275×10^{-1}	1.540	4.463	1.477×10^{-1}	1.695×10^{-1}
		10	6.738×10^{4}	5.0	2.695×10^{-1}	1.633	4.721	1.651×10^{-1}	2.163×10^{-1}
6	6	11	4.087×10^{4}	5.5	3.616×10^{-1}	1.702	4.913	2.124×10^{-1}	3.361×10^{-1}
		12	2.479×10^{4}	6.0	5.553×10^{-1}	1.739	5.015	3.194×10^{-1}	4.407×10^{-1}
7	7	13	1.503×10^{4}	6.5	7.662×10^{-1}	1.790	5.160	4.281×10^{-1}	5.440×10^{-1}
		14	9.119×10^{3}	7.0	1.065	1.946	5.610	5.471×10^{-1}	6.692×10^{-1}
8	8	15	5.531×10^{3}	7.5	1.592	2.208	6.362	7.211×10^{-1}	7.953×10^{-1}
		16	3.355×10^{3}	8.0	2.230	2.593	7.470	8.602×10^{-1}	9.203×10^{-1}
9	9	17	2.035×10^{3}	8.5	3.022	3.184	9.174	9.489×10^{-1}	1.083
		18	1.234×10^{3}	9.0	3.650	4.163	1.199×10^{1}	8.769×10^{-1}	1.120
		19	7.485×10^{2}	9.5	4.420	5.926	1.707×10^{1}	7.458×10^{-1}	1.531
		20	4.540×10^{2}	10.0	6.813	8.328	2.399×10^{1}	8.181×10^{-1}	1.643
10	10	21	2.754×10^{2}	10.5	7.650	9.491	2.734×10^{1}	8.060×10^{-1}	1.441
		22	1.013×10^{2}	11.5	1.342×10^{1}	1.626×10^{1}	4.682×10^{1}	8.256×10^{-1}	1.978
		23	3.723×10^{1}	12.5	1.644×10^{1}	4.335×10^{1}	1.248×10^{2}	3.792×10^{-1}	1.777
		24	1.371×10^{1}	13.5	1.066×10^{1}	1.249×10^{1}	3.599×10^{1}	8.535×10^{-1}	5.491
		25	5.043	14.5	3.579×10^{1}	5.377×10^{1}	1.549×10^{2}	6.657×10^{-1}	3.726
		26	1.855	15.5	2.635×10^{-1}	7.799	2.246×10^{1}	3.379×10^{-2}	9.742×10^{-1}
11		27	0.0	∞	2.657×10^{2}	7.423×10^{2}	2.147×10^{3}	3.583×10^{-1}	2.720

[a] Includes $\sigma(n,\alpha)$ in groups 1 and 2 and $\sigma(n,p)$ in group 1.

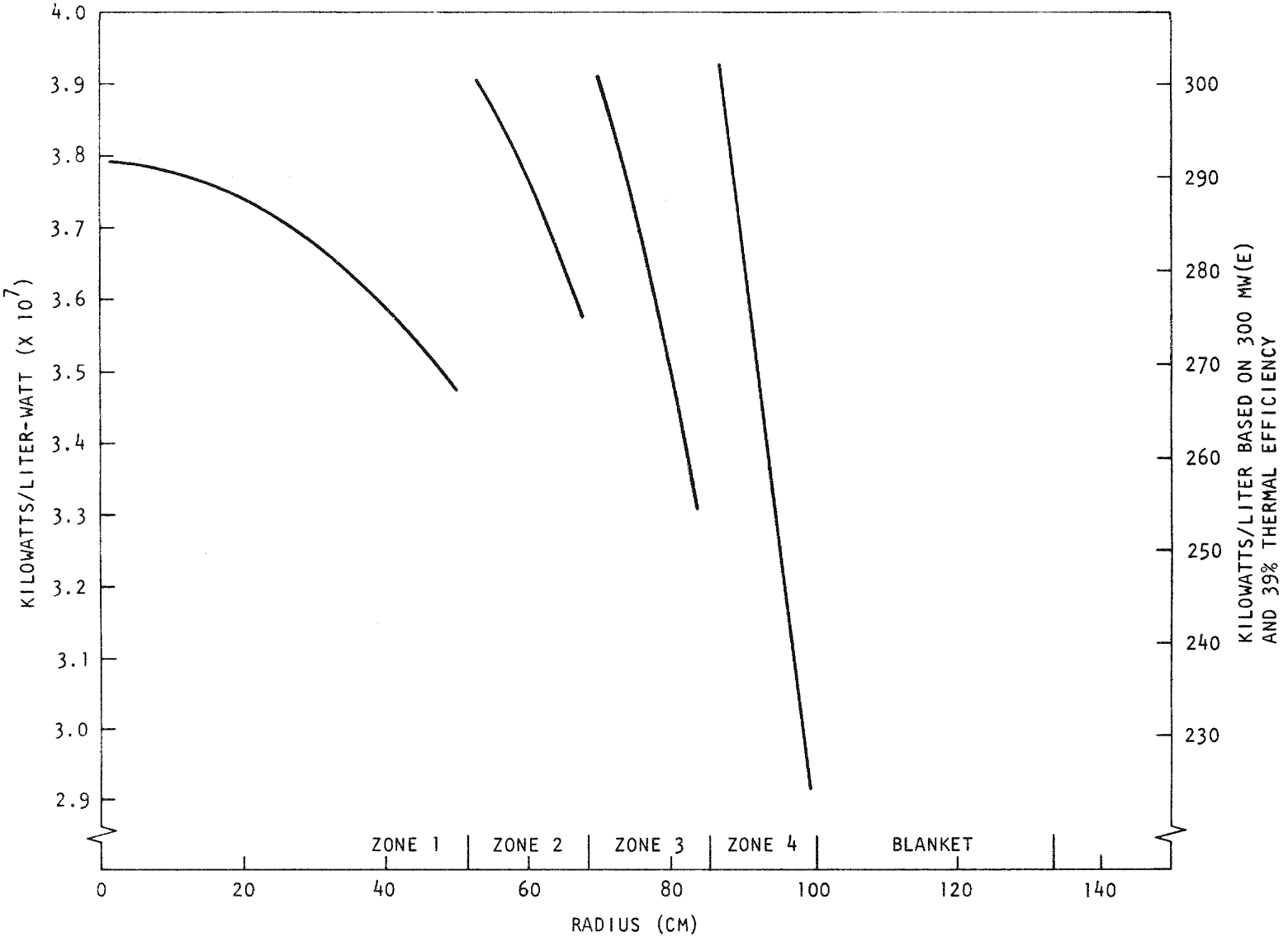

Fig. 6.4 Midplane core power density for hot, clean, unrodded core (k = 1.0638)

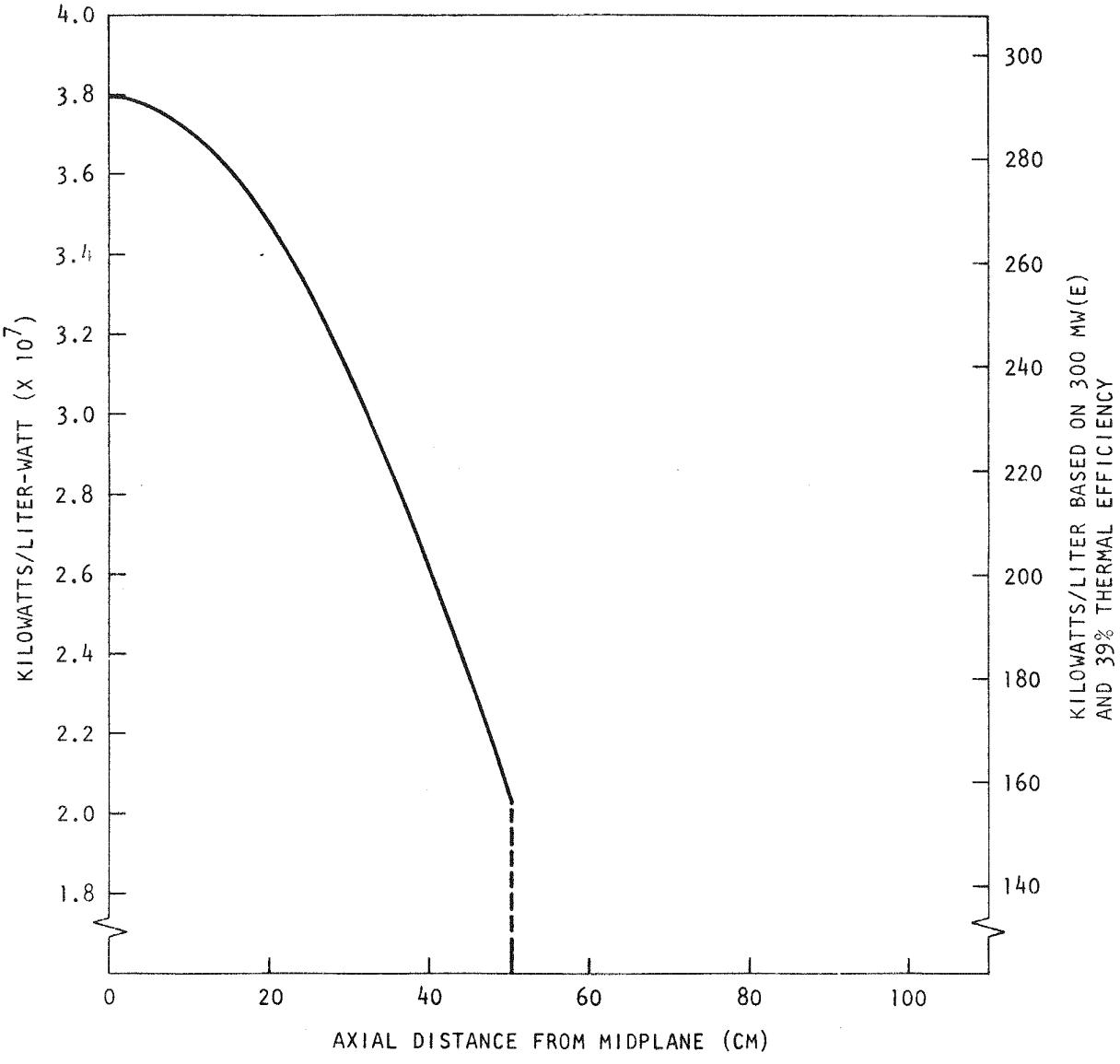

Fig. 6.5 Axial core power density for hot, clean, unrodded core (k = 1.0638)

Table 6.3

POWER CALCULATIONS

(Based on k_{eff} = 1.0638 and clean 1300°K core)

Region	Material	Volume (cm^3)	Fractional Power	Average Regional Power (kW/liter)	Maximum Regional Power (kW/liter)	Maximum / Average
1	Core zone 1	8.3670×10^5	0.2533	232.8	291.7	1.253
2	Core zone 2	6.4586×10^5	0.2013	239.7	300.3	1.253
3	Core zone 3	8.1156×10^5	0.2434	230.7	301.0	1.305
4	Core zone 4	8.9090×10^5	0.2527	218.2	302.1	1.385
5	Radial blanket	4.6044×10^6	0.0300	5.0		
6	Axial blanket 1	7.4962×10^5	0.0062	6.4		
7	Axial blanket 2	5.7864×10^5	0.0044	5.9		
8	Axial blanket 3	7.2708×10^5	0.0048	5.1		
9	Axial blanket 4	7.9816×10^5	0.0039	3.8		
10	Fe radial reflector	4.0588×10^6	0.0	0		
11	Fe axial reflector	2.2352×10^6	0.0	0		

Table 6.4

WORTHS AND KINETIC PARAMETERS

Total worth, helium, in depressurization from 85 bars to 1 bar	+ $0.457
Central worth, Pu^{239} at core center	+ 87.1 Ih/kg
Beta effective	3.373×10^{-3}
Prompt neutron lifetime	3.98×10^{-7} sec
Conversion factor, Ih/% ($\Delta k/k$)	951.75

6.5.1.4. Comparison between ANL and GGA Calculations. The GGA and ANL calculations both utilized the same geometrical model atom densities discussed above. The GGA cross sections were obtained with the GG5 code utilizing the GAROL-GANDY resonance treatments for the resolved and unresolved regions, respectively. The calculational method has been discussed previously.[7] ENDF/B Version II (modified) data were used for all the nuclides.

The GGA and ANL calculated reactor parameters are compared in Table 6.5 and the calculated neutron balances are compared in Table 6.6. Figures 6.6 through 6.9 show a comparison of the ANL and GGA integrated fluxes. As can be seen from Tables 6.5 and 6.6 and in Figs. 6.6 through 6.9, the agreement between the ANL and GGA calculations is excellent. This comparison lends further confidence to the design methods being utilized at GGA for the design of fast reactors and to the calculations made to date, especially with regard to spectra and breeding ratios.

Table 6.5

COMPARISON OF GGA AND ANL CALCULATED CORE PARAMETERS FOR THE PHYSICS DESIGN OF A 300-MW(e) GCFR

	ANL Calculated	GGA Calculated
k_{eff}	1.0638	1.0760
Absorptions per source neutron	0.925	0.921
Leakage per source neutron	0.075	0.079
Core conversion ratio[a]	0.567	0.559
Breeding ratio[a]	1.295	1.293
Beta effective	3.37×10^{-3}	3.505×10^{-3}
Total helium worth	0.46[b]	0.38[c]
Prompt neutron lifetime (sec)	3.98×10^{-7}[b]	4.30×10^{-7}[c]

[a]Fissile: Pu-239 + Pu-241,
Fertile: U-238 + Pu-240.

[b]Virgin core.

[c]Equilibrium core.

Table 6.6

COMPARISON OF GGA AND ANL CALCULATED NEUTRON BALANCES[a] FOR A 300-MW(e) GCFR

Quantity	GGA	ANL
η_{eff}	2.972	2.953
k_{eff}	1.0760	1.0638
Fissile absorptions	1.000	1.000
Fertile captures	1.293	1.295
Leakage	0.231	0.229
Fissions	1.080	1.072
Structure captures	0.132	0.185
Other H.M. absorptions	0.109	0.088
Control (for k = 1.0)	0.206	0.156

[a]Per fissile absorption, where fissile ≡ Pu-239 + Pu-241.

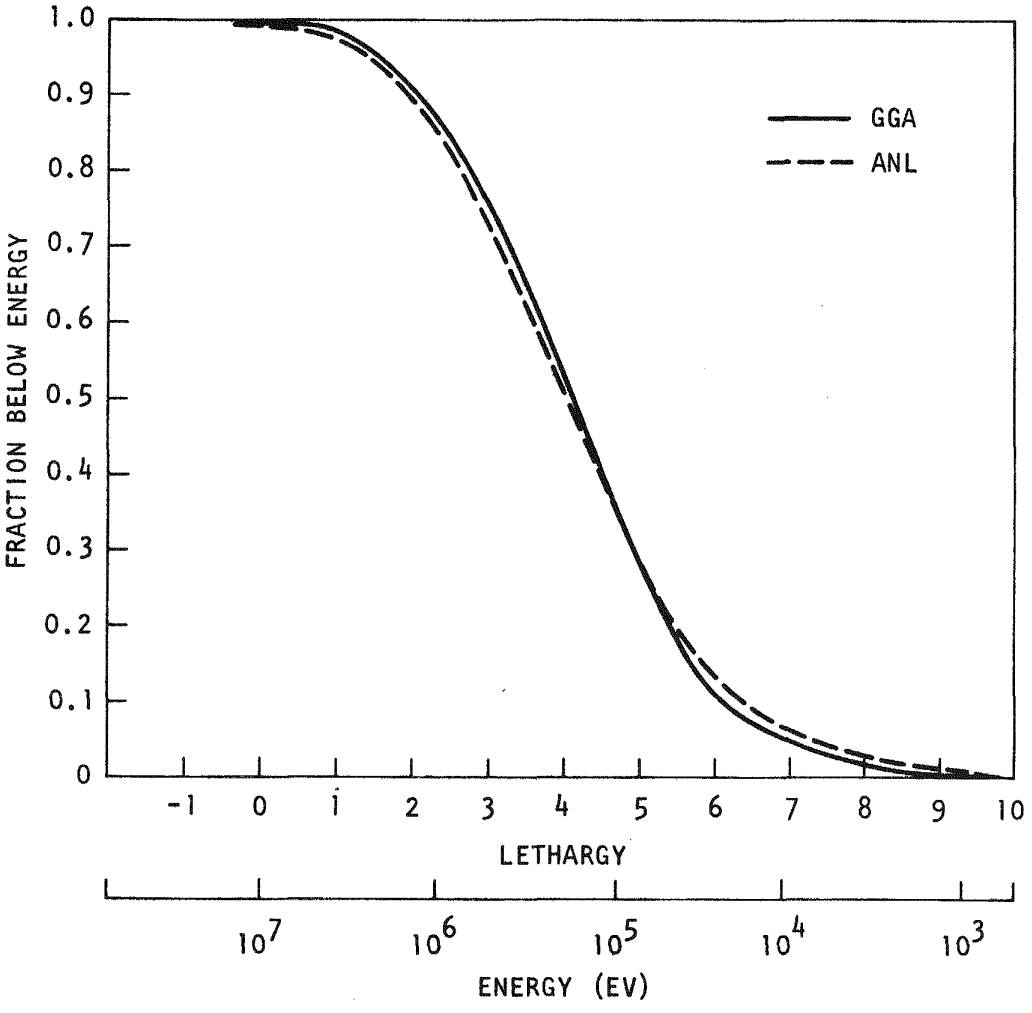

Fig. 6.6 Comparison of GGA and ANL calculated integrated fluxes for zone 1 of a 300-MW(e) GCFR

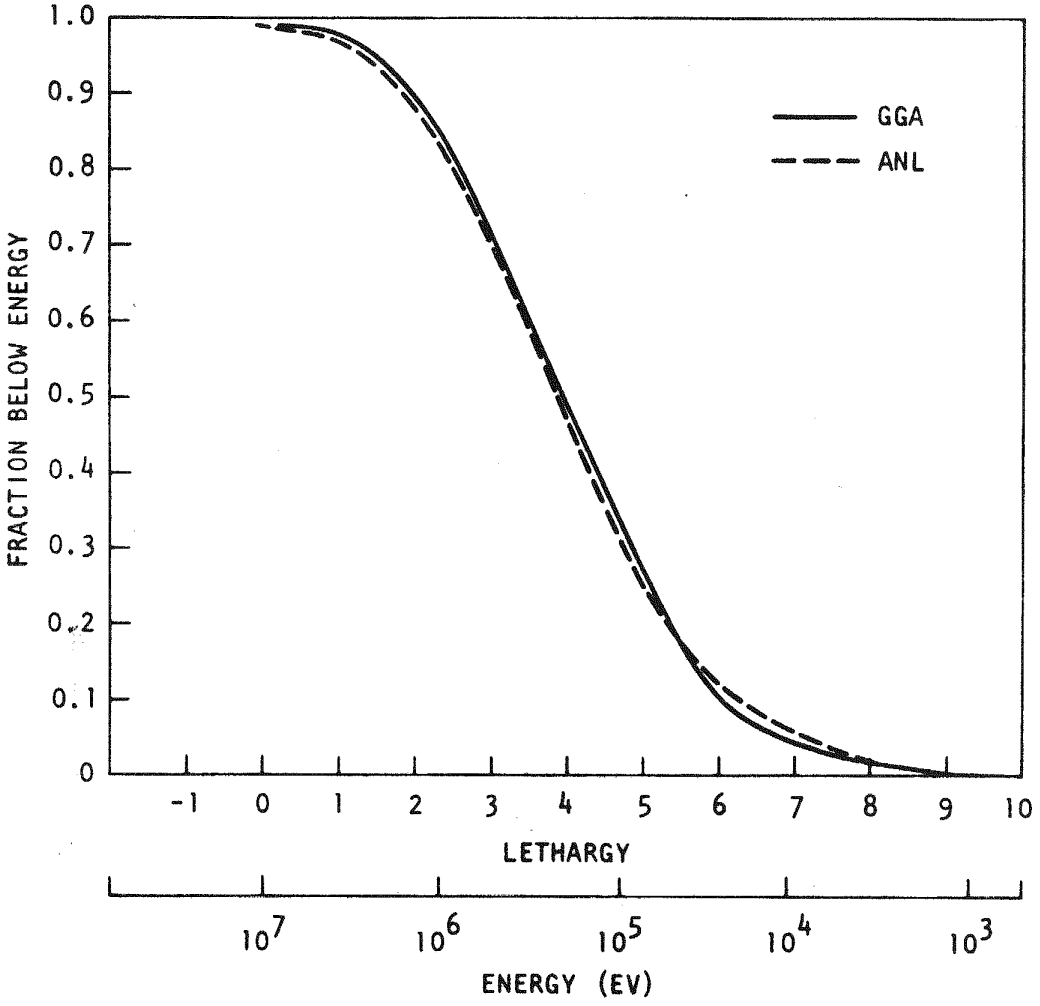

Fig. 6.7 Comparison of GGA and ANL calculated integrated fluxes for zone 2 of a 300-MW(e) GCFR

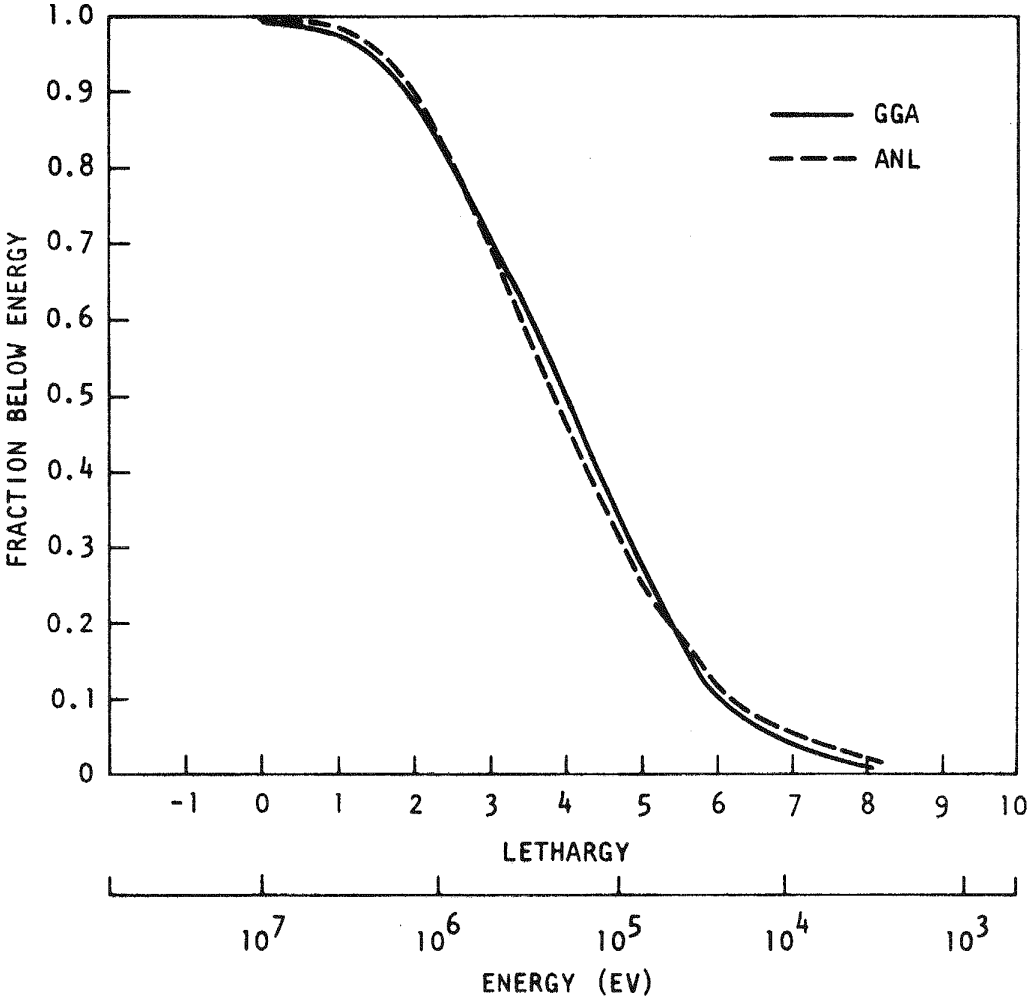

Fig. 6.8 Comparison of GGA and ANL calculated integrated fluxes for zone 3 of a 300-MW(e) GCFR

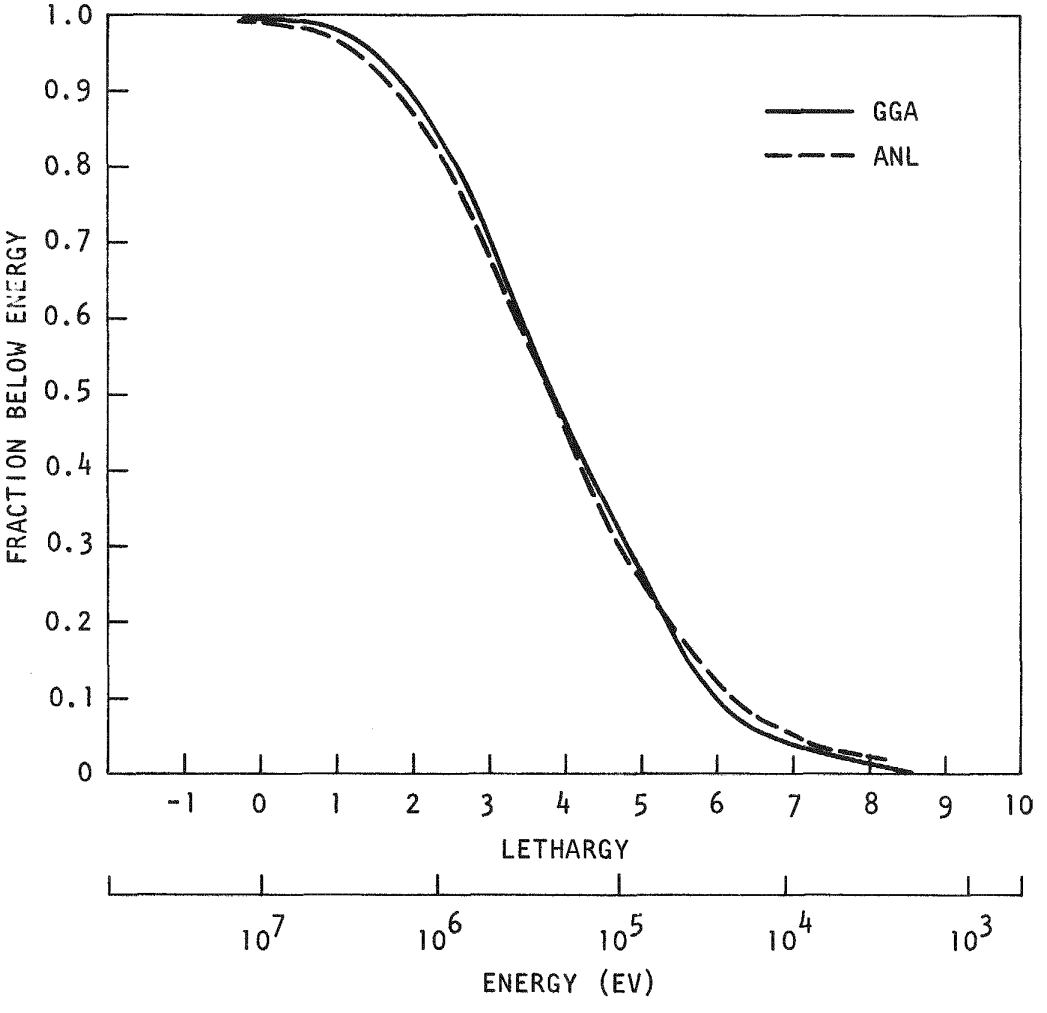

Fig. 6.9 Comparison of GGA and ANL calculated integrated fluxes for zone 4 of a 300-MW(e) GCFR

REFERENCES

1. "Gas-Cooled Fast Breeder Quarterly Progress Report for the Period August 1, 1972 through October 31, 1972," USAEC, Report GA-A12421, Gulf General Atomic, December 8, 1972.

2. Till, C. E., "Fast Neutron Doppler Effect," Proceedings, National Topical Meeting on New Developments in Reactor Physics and Shielding Reactor Technology, USAEC, CONF-702901, Book 2, September 1972.

3. Stacey, Jr., W. M., et al., "A New Space-dependent Fast-neutron Multigroup Cross-section Preparation Capability," Trans. Am. Nuc. Soc., Vol. 15, 1972, p. 292.

4. Zolotar, B. A., et al., "Benchmark Tests and Comparisons Using ENDF/B Version III Data," Trans. Am. Nuc. Soc., Vol. 15, 1972, p. 941.

5. "Gas-Cooled Fast Breeder Reactor Quarterly Progress Report for the Period February 1, 1972 through April 30, 1972," USAEC, Report Gulf-GA-A12165, Gulf General Atomic, July 20, 1972.

6. Pellaud, B., "The Physics Design of the Gas-Cooled Fast Breeder Reactor Demonstration Plant," USAEC, Report GA-10509, Gulf General Atomic, August 29, 1971, Chapter 3.

7. Toppel, B. J., ed., "The Argonne Reactor Computation (ARC) System," USAEC, Report ANL-7332, Argonne National Laboratory, 1967.

PUBLICATIONS

S. Langer, et al., "Volatile Fission-product Migration and Plateout in GCFR Fuel-rod Irradiations," Trans. Am. Nucl. Soc., Vol. 15, No. 2, November 1972, p. 850 (Gulf-GA-A12379, November 8, 1972).